Growth, phase transformation, and self-assembly in iron oxide and uranium oxide nanostructures

A Dissertation submitted to the faculty of the University of Minnesota by
Jennifer Anne Soltis

In partial fulfillment of the requirements for the degree of Doctor of Philosophy

R. Lee Penn, Advisor

October 2015

Acknowledgements

Thank you to friends and family, near and far, for their support throughout my graduate school adventures. Thank you in particular to my advisor, Lee Penn, and Wei Zhang at the University of Minnesota Characterization Facility, for their patient teaching and guidance, and to the members of the Penn Research Group, past and present, for their camaraderie, support, and general lab antics.

Dedication

Dedicated to my parents and sister
In loving memory of my grandparents

Abstract

Nanomaterials have great scientific appeal due to their unique properties and prevalence in the environment, but the fundamental mechanisms that drive nanoparticle growth, phase transformation, and assembly into larger structures are still shrouded in mystery. Considerable progress has been made in elucidating these mechanisms in the past several decades, and a comprehensive picture of nanoparticle growth is closer than ever. Advances in electron microscopy and computational modeling play a particularly important role in understanding crystal growth at the atomic-level. We use a broad suite of characterization techniques, including X-ray diffraction, conventional and cryogenic transmission electron microscopy, analytical chemistry, and magnetic property measurements, in an attempt to answer fundamental questions about the processes of nanoparticle growth and phase transformation and their assembly into larger—but still nanoscale—objects. This work documents the formation of hematite and goethite via particle-mediated growth under a variety of reaction conditions and presents, for the first time, direct images of the products of hierarchical self-assembly of uranium polyoxometalate clusters.

The abstract is reproduced in braille on the following page in recognition of the importance of accessibility to modern science. This work is available in a digital format that is accessible to screen readers.

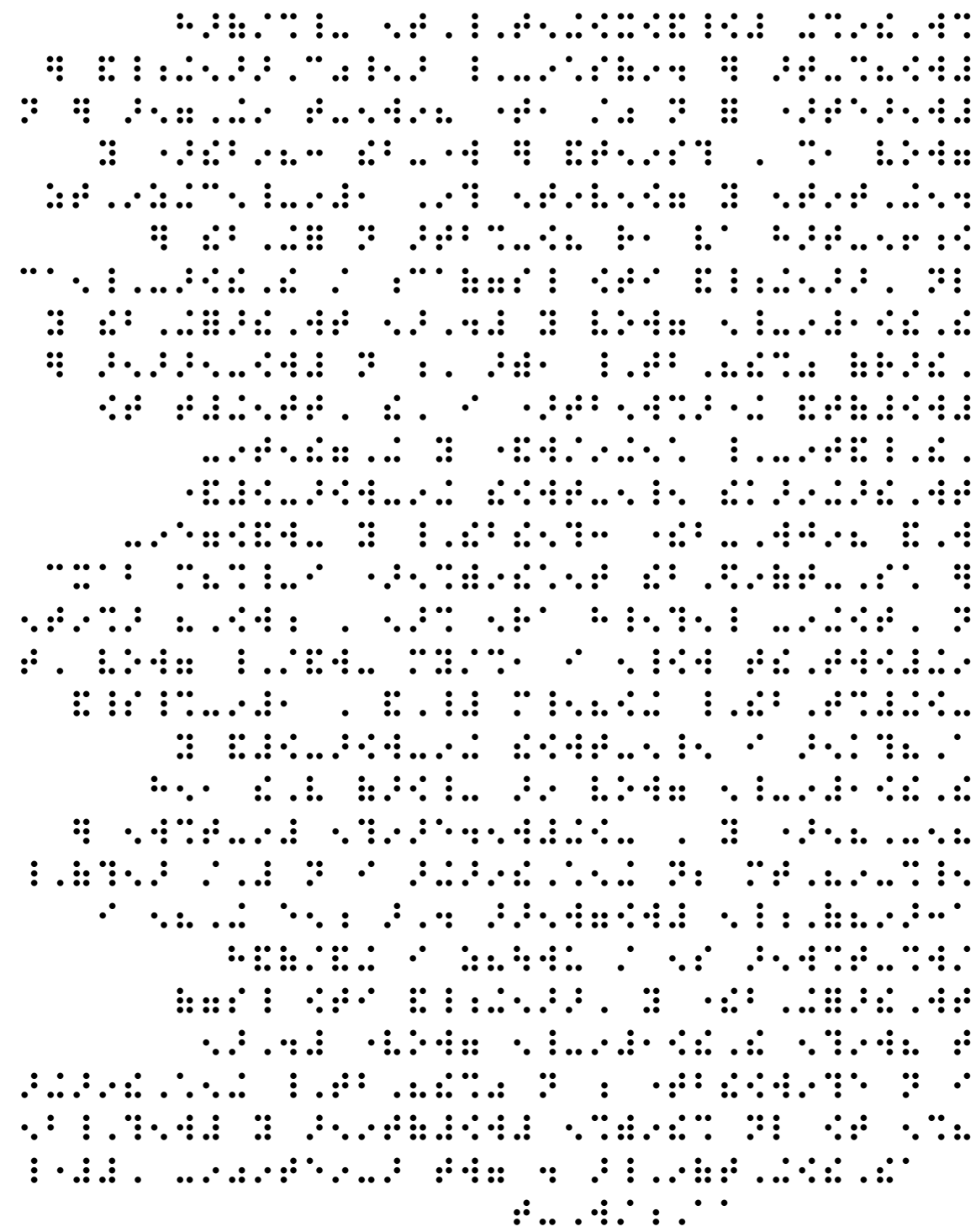

Table of Contents

List of Tables

List of Figures

Introduction

Nanoparticles play important roles in numerous and diverse fields, ranging from industry and medicine[1] to art[2] and environmental science.[3] Better understanding of the processes by which nanoparticles grow and undergo structural transformations could lead to the development of nanoparticle syntheses tunable for specific desired characteristics. Increased control over nanomaterial synthesis could benefit applications as broad as catalysis,[4-5] sensing,[6-7] recording,[7-8] and energy production.[9-10] The environmental impact of nanoparticles is also important, where predicting the fate and transport of elements and nutrients in the environment has far-reaching implications for agriculture, aquaculture, and public health.[11-13]

Crystal growth has been a rich area of study for hundreds of years, and two processes—coarsening (Ostwald ripening) and aggregation and recrystallization—have been considered major crystal growth mechanisms. However, these models cannot adequately explain the formation of structures such as crystal twins and dislocations.[14-16] Non-classical crystal growth has become increasingly recognized as an important area of study over the past several decades, and particle-mediated growth mechanisms, such as oriented attachment, can provide pathways for the production of nanostructures of controlled size, shape, and microstructure.[17] Chapter 1 is a review of oriented attachment and other forms of non-classical crystal growth with a special focus on the iron oxides.

Iron oxides are important in sequestration and mobilization of toxic elements, such as arsenic, lead, uranium, and plutonium.[18-19] Iron is the most abundant transition metal in the crust and critical for many life processes, but it is only bioavailable in its reduced form.[20] Iron oxide nanoparticles can grow, dissolve, phase transform, and directly and

indirectly participate in redox reactions. Reactivity depends on mineral identity and morphology. Different crystal faces have different energies and activities. Phase transformation can affect the ability of iron oxide minerals to sequester or release harmful elements.[13, 21] Phase transformation is often governed by thermodynamics,[22] but thermodynamics of nanoparticles can be very complex and behaviors are hard to predict, particularly when there are many variables, such as in natural settings.

Chapters 2 and 3 focus on crystal growth and phase transformations involving ferrihydrite nanoparticles. Ferrihydrite is a poorly crystalline iron oxyhydroxide that undergoes relatively rapid phase transformation to more stable iron oxide minerals.[23] Chapter 2 investigates the mechanism of hematite formation from 2-line ferrihydrite (named for the number of peaks in its X-ray diffraction pattern) and attempts to elucidate the individual roles of phase transformation and particle growth in this process. A wide range of characterization techniques were employed. Remanent magnetization studies provided particular insight and were able to detect vanishingly small amounts of hematite undetected by other techniques.

Iron oxides in natural settings exist in complex environments as compared to the laboratory, and this increased complexity is the emphasis of chapter 3. Here, 2- and 6-line ferrihydrite were mixed with goethite and/or hematite and aged at elevated temperature to investigate the effects of heterogeneous precursors on phase transformation. This represents a small step towards modeling the diversity of real environmental settings.

The redox reactivity of iron oxides has an important influence on their ability to participate in reactions. Indeed, redox reactions facilitated at iron oxide nanoparticle surfaces can be a critical part of the degradation of organic compounds[24-26] or the

reductive dissolution of the particles themselves.[27-31] Though the role of iron oxides in environmentally-relevant redox reactions is widely studied, the exact nature of electron transport in iron oxide nanoparticles has not been well-characterized. Chapter 4 examines electron transport rates in ferrihydrite nanoparticles in aqueous suspension as a function of particle size, pH, and the number of injected electrons.

Chapter 5 looks at nanostructures of a different type and is motivated by the need to understand nanoscale components of mixed nuclear waste. One legacy of nuclear research in the United States is an unknown amount of poorly-characterized radioactive waste, such as the 53 million gallons held in,[32] and up to one million gallons leaked from,[33] underground storage tanks at the Hanford Site near Richland, Washington. This waste may have the conditions necessary for the formation of actinide polyoxometalate (POM) nanoclusters. U60 is a uranium oxide peroxide nanocluster and is one such POM that has been synthesized under laboratory conditions.[34-36] Though actinide POMs have not been observed in nature or nuclear waste to date, the formation of uranium-based materials has been detected on the exterior of failed fuel cladding, and the formation of a U POM in liquid waste could be possible if sufficient uranium ions and peroxide (produced by the radiolysis of water) are present. One of the characteristics of POMs that make them so interesting and useful is their ability to undergo hierarchical self-assembly.[37] U60 has been observed to form hollow, spherical structures referred to as "blackberries" after the pioneering work of Liu and coworkers in transition metal POM self-assembly.[38-39] The formation of U60 blackberries is cation dependent.[40] However, U-POM blackberries are not stable when dry, so characterization to date has necessarily been in situ, and these structures have not previously been directly imaged. Here,

cryogenic transmission electron microscopy (cryo-TEM) was used to directly image POM secondary and tertiary structures for the first time. The data enabled detailed descriptions of trends in how structure, size, and morphology change upon addition of soluble cations.

As nanotechnology plays an increasingly important role throughout the world, it is critical to increase our understanding of the fundamental principles driving nanoparticle growth. Nanoparticle shape, size, and structural phase all influence their physical, chemical, optical, and electronic properties and affect their reactivity. This has implications in industry, where the synthesis of nanoparticles with targeted properties is a major goal, and in the environment, where nanoparticles play an important role in biogeochemical cycling of both beneficial and harmful elements and chemicals. Insight into the fundamentals of phase transformation, growth mechanisms, and self-assembly of nanoparticles and nanoscale objects will aid efforts in all of these fields.

Chapter 1 : Oriented attachment and non-classical formation in iron oxides

Jennifer A. Soltis[1] and R. Lee Penn[1]

[1]Department of Chemistry, University of Minnesota, Minneapolis, Minnesota 55455, United States

This chapter is in press in *The Iron Oxides*, Damien Faivre, ed. Wiley-VCH.

Introduction

Iron oxides are ubiquitous in Earth's environment and crust and can be readily synthesized in the laboratory. Many iron oxide minerals can undergo crystalline or mineral phase transformation to produce polymorphs (minerals with the same chemical formula but different structures, e.g. goethite (α-FeOOH), akaganeite (β-FeOOH), and lepidocrocite (γ-FeOOH)) or transform into minerals of different compositions (e.g., the transformation of goethite to hematite (Fe_2O_3)). The role of iron oxides in environmental and industrial applications is of particular interest because of their incredible diversity of structure, shape, and composition, all of which affect their chemical and physical behavior. Many desirable characteristics of iron oxide nanoparticles are shape dependent and understanding and controlling crystal growth is a long-sought-after goal.

Rochelle Cornell and Udo Schwertmann made significant contributions to expanding our understanding of many facets of iron oxide chemistry, as summarized in part in *The Iron Oxides: Structures, properties, reactions, occurrences and uses*.[23] This also includes major contributions to catalogs of nanoparticle syntheses (*Iron Oxides in the Laboratory:*

Preparation and Characterization)[41] and insights into nucleation, growth, and phase transformations in iron oxide nanoparticles.

Understanding crystal growth and phase transformations in iron oxide systems has changed greatly since Cornell, Schwertmann, and others began their work. Early on, it became clear that classical crystal growth could not adequately explain the myriad textures and morphologies observed for both natural and synthetic iron oxides. Classical crystal growth involves growth by diffusion of molecular-scale species from smaller crystals to larger ones, and the mechanism typically gives rise to crystals that have well-faceted shapes and that lack defects (except point defects). Growth by this process is referred to as coarsening or Ostwald ripening.[42-43] While random aggregation was also recognized to play an important role in iron oxide crystal growth, again, random aggregation could not readily explain observed textures and shapes. In particular, the formation of structural features like edge dislocations and twins remained a mystery.

Nonclassical crystal growth mechanisms have become widely recognized as important in a wide range of materials, including the iron oxides. Oriented attachment (OA), in particular, has been observed in numerous studies involving synthetic iron oxides. OA is a particle-mediated crystal growth mechanism in which primary crystallites come together, achieve crystallographic registry with respect to one another, and finally attach to form new secondary crystals. OA, also referred to as oriented aggregation or

epitaxial assembly,[44] was first described as "oriented attachment" by Penn and Banfield in titanium dioxide systems,[14-15, 45] and examples of crystallites that have characteristics consistent with growth by OA have been described in the scientific literature published before introduction of the term.[46-47] OA has been widely studied in materials such as metal oxides and oxyhydroxides,[14-15, 44-45, 48-57] selenides and sulfides,[58-60] and biominerals.[61-64]

OA can be described as a multi-step mechanism, which is depicted in Figure 1.1. Primary particles (I) reversibly form particle-particle complexes that lack any particular crystallographic orientation (II). In a molecular model of OA, these assemblies are analogous to outer sphere complexes, which can dissociate.[14, 65] Within the complexes, primary particles can rearrange via Brownian motion. If crystallographic registry is achieved, the result is a structural intermediate (III; previously referred to as a mesocrystal[66-70]) within which no direct particle-particle contacts have formed.[71] The space separating the primary crystallites is hypothesized to be filled with solvent and other dissolved species. In aqueous systems, the water molecules may be arranged in a crystalline fashion.[72] Such species must either be removed or incorporated into the final secondary crystallite (IV).[49, 65] It is important to note that, though one crystal growth mechanism may dominate, OA and coarsening frequently operate simultaneously.[58, 61, 73]

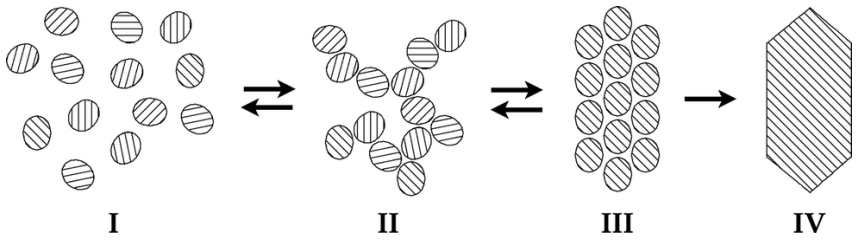

Figure 1.1: "Schematic illustrating oriented aggregation. Primary particles (I) reversibly form loose assemblies (II) analogous to outersphere complexes. Particles in the random assembly rotate and rearrange via Brownian motion until crystallographic alignment is reached (III). The particles can then irreversibly attach to form a continuous crystal (IV)."[74]

The rates of crystal growth via OA and coarsening depend on factors such as crystallite size and solubility, and the relative contributions from each mechanism can thus with time.[75] For example, the rate of OA (k_{OA}) is strongly size dependent, with growth via OA decreasing with increasing crystallite size.[49] The relative contribution by OA and coarsening depends on the both particle-particle interactions and the solubility of the crystallites. If a particular material is highly soluble, then growth will likely be dominated by coarsening. In contrast, sparingly soluble materials may be more likely to grow by OA or another particle mediated crystal growth mechanism. In the case of iron oxides, both solubility and surface charge depend strongly on pH. Thus, large changes in the relative contribution to growth by OA and coarsening would be expected. Finally, as the average crystal size increases with time, the relatively contribution to growth by multiple mechanisms would likely change substantially. For example, growth by OA will slow with increasing particle size. Similarly, the solubility of smaller crystals is higher than for larger crystals.

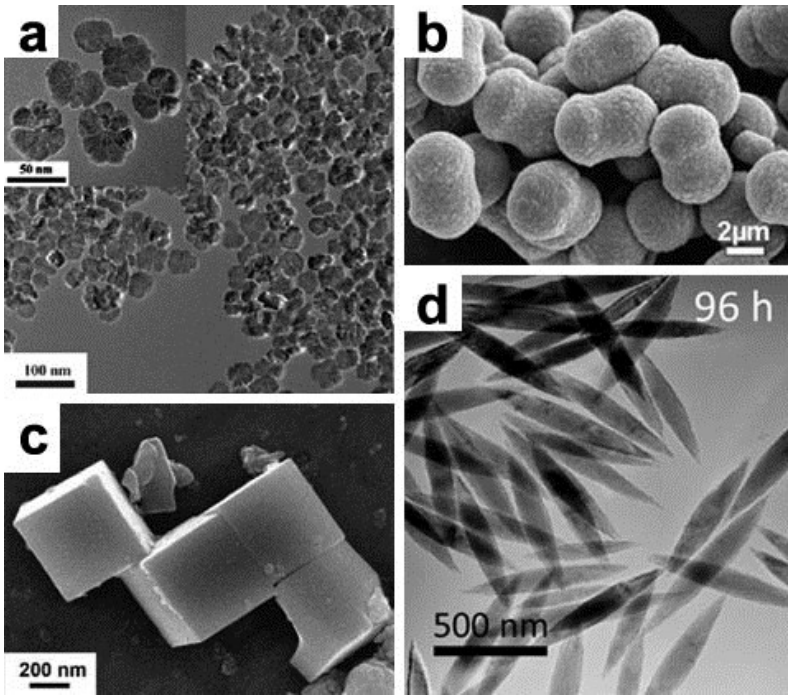

Figure 1.2: Electron micrographs of hematite nanoparticles showcase some of the wide variety of morphologies produced from growth via OA: (a) nanoflowers,[76] (b) peanuts,[77] (c) nanocubes,[78] and (d) spindles.[79] The scalebars in (a) are 100 nm and 50 nm (inset).

Nanocrystals with unique, symmetry-defying morphologies are often a hallmark of growth via OA.[14] Growth by OA yields a rich variety of particle morphologies, including twinned crystals, rods, ellipsoids, spindles, needles, prisms, hexagonal plates, diamonds, hollow and mesoporous spheres, dendrites, complex nanowire structures, and structures described as horseshoes, nanostars, elbows, butterflies, and nanoflowers.[65, 68, 76, 80-83] Particles of many different morphologies but the same composition may also result, with growth directed by reaction conditions. Figure 1.2 shows an array of electron micrographs of hematite nanocrystals where OA is the dominant growth mechanism, including spindles,[79] nanoflowers,[76] cubes,[78] and peanuts.[77]

These unique morphologies are sometimes the result of atomic-level structural differences that are a consequence of growth by OA. Twins and stacking faults may result when two-dimensional structural accord is achieved at the interface of two primary particles but not aligned along the axis perpendicular to the interface.[14] An example of twinning in a lepidocrocite crystal is shown in the transmission electron microscopy (TEM) images of **Figure 1.3**a and b. Lattice fringes, directly corresponding to the crystallographic structure of the nanoparticle, are highlighted with black lines in the high resolution image in **Figure 1.3**b.

When OA occurs across rough surfaces, defects such as edge dislocations can be incorporated into the secondary crystals.[14, 57] TEM images of an edge dislocation resulting from the assembly of TiO_2 nanoparticles are shown in **Figure 1.3**c and d. An arrowhead marks the edge of the terminating plane in the dislocation in **Figure 1.3**d. The lattice fringes nearest the dislocation are outlined in black to help guide the eye. These dislocations are energetically-strained compared to defect-free areas of the crystal and are sometimes eliminated through recrystallization.[61] Additional oriented attachment across such slightly misoriented primary crystallites could results in the incorporations of screw dislocations.[14]

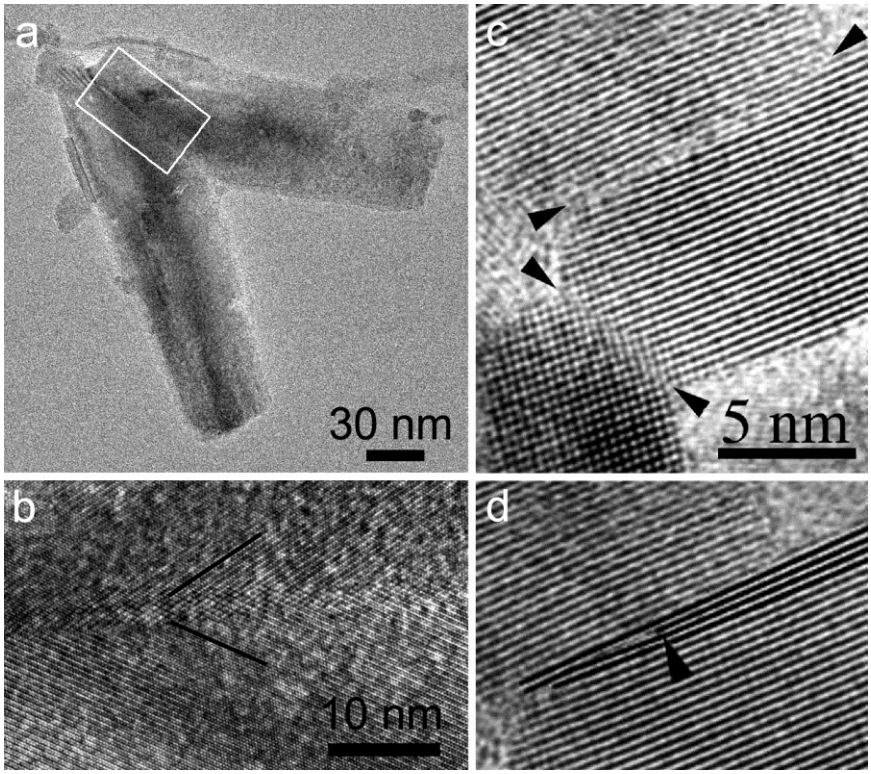

Figure 1.3: Low and high resolution TEM images showing twin and dislocation structures in nanoparticles grown via OA. (a) A twinned lepidocrocite (γ-FeOOH) nanoparticle prepared by aging 6-line ferrihydrite nanoparticles with 2 mM $FeCl_2$ in pH 7 MOPS (3-(N-morpholino)propanesulfonic acid) buffer under anoxic conditions for 21 hours. The area outlined in white is shown at higher resolution in (b). Black lines highlight the lattice fringes exhibiting symmetry across the twin boundary. (c) "HRTEM image of three attached TiO_2 particles. Arrowheads mark interfaces between primary particles. The edge dislocation at the upper interface is reproduced [in (d)], with lattice fringes around the terminating plane (arrowhead) highlighted for clarity."[14] Images (a) and (b) were taken by the authors. Images (c) and (d) are adapted with permission from Penn, R. L.; Banfield, J. F., Imperfect Oriented Attachment: Dislocation Generation in Defect-Free Nanocrystals. *Science* 1998, *281* (5379), 969-971, Fig 1.

OA in iron oxides in the literature:

The earliest descriptions of OA in the scientific literature predate the introduction of the phrase "oriented attachment." Bailey et al. used results from cryogenic transmission electron microscopy (cryo-TEM) to elucidate the formation of 1.5 μm hematite nanocubes from rafts of rod-shaped akaganeite nanoparticles aligned along <001>. They

demonstrated that the rafts of akaganeite rods yielded electron diffraction patterns consistent with single-crystal akaganeite in addition to single-crystal hematite, indicating that hematite had begun nucleating in the structure of the raft.[46] Ocaña et al. also reported on the "ordered aggregation" of small ellipsoidal hematite nanoparticles into larger crystalline structures[47] and Fischer and Schwertmann described a case ferrihydrite to hematite transformation that may also be an example of OA and interface nucleation.[84] Other examples undoubtedly exist.

Goethite:

Burleson and Penn proposed a two-step growth mechanism for the synthesis of goethite nanorods from a ferrihydrite precursor at pH 6.[85] The first step is a phase transformation of primary particles from ferrihydrite to goethite, followed by assembly of goethite primary particles into nanorods via OA.[66, 85] The rate of goethite growth via OA and the size of nanorods produced can be affected by temperature, pH,[85-86] ionic strength,[87] precursor particle size,[48-49] and the presence of chemical additives.

Work on goethite growth at low pH contrasts with studies by Schwertmann and Murad at high pH, which indicated that growth occurs via a dissolution reprecipitation mechanism.[88] No evidence of goethite growth via OA has been found in high-pH syntheses and it is thought that a dissolution precipitation mechanism dominates at high pH due to increased solubility of iron oxides at these pH levels.[89] Likewise, Cornell et al.

found support for a dissolution-precipitation mechanism in the transformation of ferrihydrite to goethite, hematite, and lepidocrocite at moderate pH. [90]

Hematite:

Hematite has also been found to grow via OA when produced by aging an acidic ferric chloride solution.[44] There are numerous other examples of growth of hematite via OA,[44, 76-79, 91] including one- and two-dimensional assembly of larger (>100 nm) primary particle building blocks, which are larger than any primary particles previously reported.[91] Dissolution precipitation[89-90] and internal dehydration mechanisms paired with aggregation (perhaps another early case of interface nucleation)[84, 92] are also commonly documented growth mechanisms in hematite nanoparticles.

Other iron oxides:

Feroxyhite (δ-FeOOH) has been observed to grow by assembly, possibly in an oriented manner.[44] Lepidocrocite rods were seen to form reversible crystallographically-ordered assemblies, but no aggregation was observed in lepidocrocite lathes.[93] Hockridge et al. conclude that their synthesized schwertmannite particles are composed of a ferrihydrite core surrounded by goethite needles that grew via OA.[94]

Natural samples:

Banfield et al. first reported on aggregation-based crystal growth in iron oxides in natural samples in 2000.[53] Ferrihydrite and goethite nanoparticles were observed coating, and in close proximity to, the iron-oxidizing bacteria *Gallionella* sp. and *Lepthothrix* sp. TEM imaging indicated the presence of crystallographically ordered chains of nanoparticles and goethite rods with edge dislocations consistent with growth via OA.

OA and phase transformation:

Phase transformations in iron oxides are often controlled by size-dependent thermodynamic relationships between initial and product phases—the new phase is not thermodynamically favored until crystallites of the initial phase have assembled to a critical size.[22] Bailey et al. and Frandsen et al. observed the assembly of akaganeite particles into larger single-crystalline rafts or clusters prior to transformation to hematite. The secondary structures then underwent phase transformation into hematite. [46 79] Frandsen et al. hypothesize that this phase transformation happens when the akaganeite clusters reach a critical size at which hematite is then thermodynamically favored.[22, 79]

X-ray diffraction patterns and electron diffraction revealed akaganeite and hematite were present simultaneously during much of the phase transformation and further growth of hematite particles. [46 79] Phase transformation in these systems may be attributed to the interface nucleation mechanism, in which a new mineral phase begins forming at the

interface between two surfaces of the initial phase.[95] Interface nucleation has been extensively researched in TiO_2, where it occurs after OA of primary particles. Several models describing this mechanism have been developed and will be discussed below.[45, 95-101]

Detection and characterization of growth by oriented attachment

Imaging:

Direct imaging of nanoparticles using transmission electron microscopy (TEM) and high-resolution TEM has long been the go-to techniques for identifying growth via OA. The detection of features such as crystal twinning, dislocations, and dimpled boundaries in TEM images can indicate relics of growth by OA.[74] Figure 1.4 shows a pair of TEM images of goethite synthesized from a ferrihydrite precursor.[85] The upper, lower resolution image shows the goethite rods produced by this synthesis. In the high-resolution image of a rod tip (Figure 1.4, lower), continuously crystalline regions and small defects are visible, consistent with growth by OA.[14-15, 45, 85] The dimpled edges of the rod have nodules similar in size and curvature to the precursor particles. These structures and morphological features can be indicative of growth via OA. The dimpled surface will gradually fill in via coarsening, with the morphological features characteristic of growth by OA becoming less and less obvious.[85]

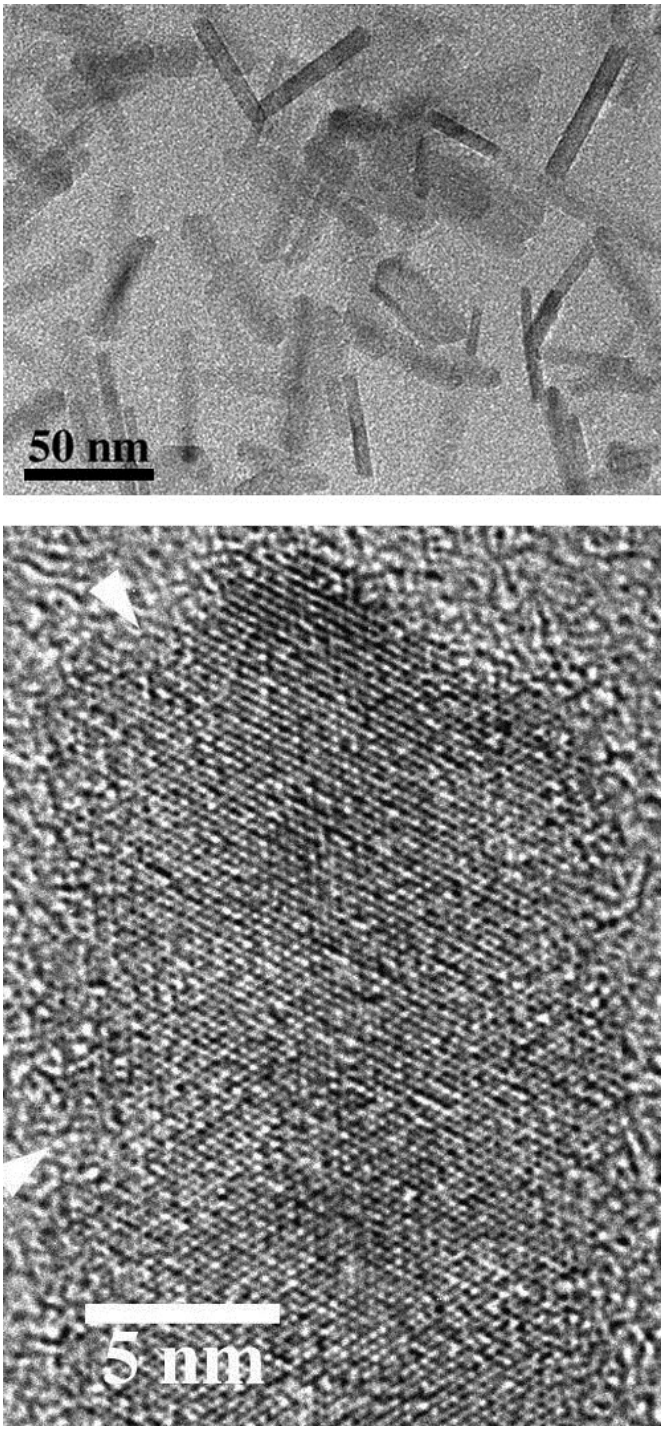

Figure 1.4: *(Upper)* TEM image of goethite nanoparticles. *(Lower)* HRTEM image a goethite nanoparticle tip. White arrowheads serve to highlight two of many regions containing defects. *(JEOL 2010, Pacific Northwest National Labs)*

Observations of textures consistent with crystal growth by OA are not necessarily sufficient for concluding a crystal has formed by OA. Indeed, features like dimples and

twins could form by other crystal growth mechanisms, including random particle attachment followed by recrystallization.[102] Similarly, a lack of such features is also not sufficient evidence for crystal growth by coarsening, since rough surfaces and defects can effectively be erased by competing mechanisms. Thus, correlative methods, such as tracking particle size distributions using in situ light and X-ray scattering methods, and in situ imaging methods like cryogenic TEM, are essential.[74]

Cryogenic and fluid cell TEM:

Two major challenges in conventional TEM are the ex situ nature of dry samples and the potential for artifacts introduced upon drying during specimen preparation. Cryogenic (cryo) and fluid cell TEM can be used to directly characterize particles in their liquid state. In cryo TEM, a thin film of sample is vitrified by plunging into liquid cryogen, which ideally results in vitrification of the solvent and preservation of the arrangement of nanoparticles in the solvent. In addition, vitrification yields a sample that facilitates direct imaging of nanoparticles as they exist in the liquid solvent because the solid amorphous solvent will not produce diffraction contrast in the TEM image.

Figure 5 shows a pair of cryo TEM images of the synthesis of goethite from ferrihydrite over 24 days at 80 °C. Prior to aging, primary particles reside in small clusters (Figure 1.1 stage II). The fraction of primary particles residing in rod-shaped structural intermediates (Figure 1.1 stage III) increases with time, and many of these

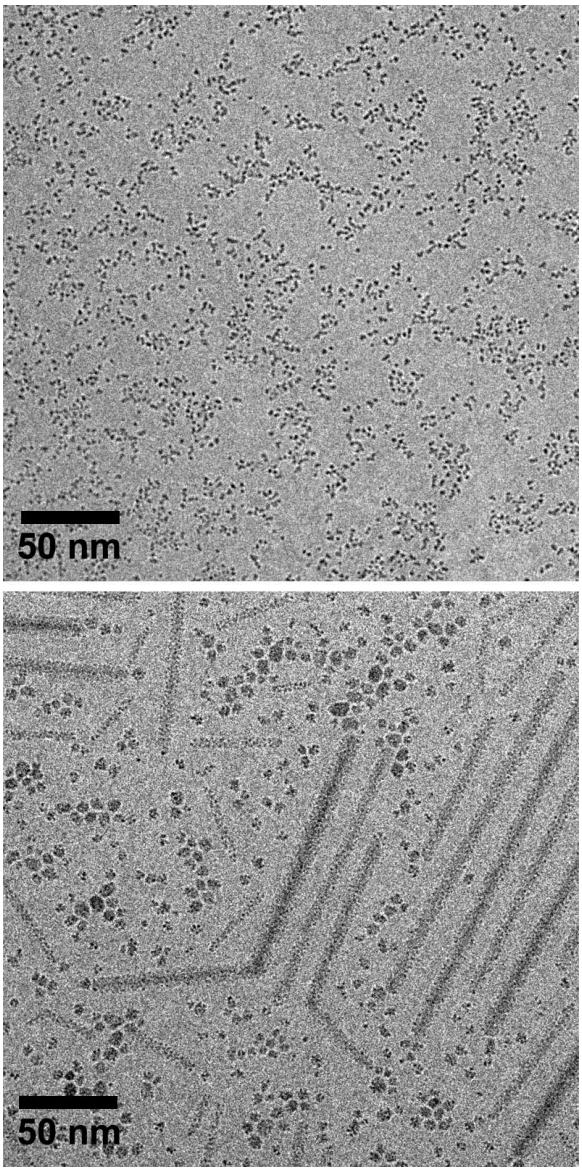

Figure 1.5: Cryo-TEM images of ferrihydrite nanoparticles prior to aging (upper) and structural intermediates (lower) formed during the synthesis of goethite from ferrihydrite 24 days at 80 °C. The primary particles comprising the structural intermediates lack direct contact with each other, visible in the lower image. Structural intermediates of V-shaped twinned goethite rods can also be seen. Synthesis and procedure are from Yuwono, V.; Burrows, N. D.; Soltis, J. A.; Penn, R. L., Oriented Aggregation: Formation and Transformation of Mesocrystal Intermediates Revealed. *J. Am. Chem. Soc.* 2010, *132*, 2163–2165, images by V. Yuwono.

intermediates are seen in the lower image (24 days). Electron diffraction patterns and lattice-fringe resolution images (not shown) are consistent with structural intermediates composed of crystallographically aligned particles.[66] Additionally, the structural

intermediates are similar in size and morphology to the final rod-shaped crystals. The angle of twinning of the twinned intermediates formed after 24 days is consistent with a single-crystal goethite twin.

A recent development in TEM sample holder technology enables direct imaging of nanoparticles in liquid suspension, which can yield unprecedented insight into the dynamics of particle-particle interactions. A fluid cell encloses a small amount of liquid sample between electron-transparent windows.[74, 103] Some fluid cell holders can accommodate single- or dual-input flow cells, permitting mixing experiments, or incorporate electrochemical and thermal controls.[103] While cryo TEM provides a "snapshot" of particle configuration at a particular moment in time, fluid cell TEM permits the continuous observation of particle movement, rearrangement, growth, and even dissolution. Data collection in fluid cell experiments is often in movie format.[61, 103-104]

OA in iron oxides has been directly imaged in real time via fluid cell TEM.[61] Ferrihydrite nanoparticles in aqueous suspension make repeated contact with one another until they achieve crystallographic alignment and form particle-particle attachments.[61] After particle attachments are formed, coarsening takes over as the dominant crystal growth mechanism and dimples resulting from the morphology of the starting particles are then filled in.[61] The rate of coarsening was quantified by measuring the elimination of

curved surfaces at particle-particle interfaces and found consistent with the dependence of chemical potential on interface curvature.[61, 105] This work directly demonstrated simultaneous OA and coarsening and that the relative influence of each process on growth varies over time and depends on crystal shape and size.[58, 61, 73, 106-108]

Both cryo and fluid cell TEM provide insight into in situ nanoparticle conformations that is not available through any other methods, but these techniques are not without risks. Beam effects are a major challenge in both techniques. In cryo TEM, excess exposure to the electron beam can cause crystallization or melting of the vitrified solvent, which decreases its electron transparency and can alter arrangements of nanoparticles as the solid matrix changes.[109] In fluid cell TEM, both the solvent and particles may be affected by radiolysis[110] and interactions with the windows of the fluid cell can also affect nanoparticle behavior.[73, 104, 111] Beam interactions may also increase the solubility of nanoparticles—the addition of an electron to a structural Fe^{3+} reduces it to the more soluble Fe^{2+}.[112]

Correlative methods:

While TEM methods enable acquisition of direct images of nanoparticles, with atomic-scale resolution readily feasible, the techniques produces images of vanishingly small amounts of material. The material imaged in a typical high-resolution micrograph is on the scale of attograms. Thus, techniques for analyzing larger amounts of material

are necessary for characterizing bulk samples, even when bulk refers to only a few milligrams (which could contain on the order of 10^{10}-10^{17} nanoparticles). Diffraction techniques, namely X-ray diffraction (XRD),[52, 58, 113] can be used to identify minerals and measure crystal domain lengths, including the detection of bimodal particle size distributions. Scattering techniques, such as small angle X-ray scattering (SAXS),[102, 114-115] small angle neutron scattering (SANS),[116] and dynamic light scattering (DLS)[114, 116-117] are used to measure particle sizes and size distributions. Finally, ultra-violet-visible (UV-vis) spectroscopy can be used to determine size from size-dependent optical properties of some nanoparticles,[118] though this technique has less applicability to nanoparticles (including some iron oxides) that do not change color or optical properties with size. An in-depth review of methods for characterizing growth via OA can be found in Penn and Soltis, 2014.[74]

Kinetics of growth by oriented attachment

The rich diversity in models for OA provides many possible directions for increasing our understanding of the nuances of the kinetics and mechanism behind this growth process. Major questions include: When is control governed by thermodynamics vs. kinetics? What is the rate-limiting step? Is growth reaction-limited or diffusion-limited? How does rate of growth vary with crystallographic direction and what impact does this have on aggregate morphology? These questions about kinetic control also have bearing

on the fundamental issue of the driving forces behind oriented attachment. Many of the models used for quantifying kinetics of OA are reviewed in Burrows et al., 2010.[119]

Kinetic models for OA often justifiably model nanoparticles as molecules.[14, 65, 82, 120-121] Nanoparticles are ca. one to three orders of magnitude larger than small molecules but far smaller than macroscopic crystallites.[82] Like molecules, they can diffuse, rotate, and translate in suspensions and undergo Brownian motion,[122-123] and molecules and nanoparticles are both small relative to the thickness of their electric double layer.[121, 124] Finally, collision reactions between molecules may result in the formation of a single new entity, just as reactions between nanoparticles can result in the production of a single object.[82] Aggregation of both molecules and colloids can be described by Smoluchowski theory,[125] which was used as a basis for many early models.

Transition state theory requires that reacting molecules (or nanoparticles) have sufficient kinetic energy to overcome the activation energy barrier and must undergo effective collisions if a new structure is to be formed.[121, 124, 126] This is considered in many of the models presented here by including separate non-bonding association and dissociation steps or by specifically taking into account attachment efficiency or the probability of successful attachment.[58, 65, 120, 124, 127]

Molecular dimer formation models

One of the earliest kinetic models was presented by Penn and makes an argument for a second-order rate law to describe growth via OA.[65] This model is simple and versatile and the rate laws produced have good correlation with experimental data on the kinetics of OA.[49, 86-87, 119] Primary particles reversibly form a particle-particle complex, which can either dissociate or irreversibly form oriented aggregates. Using either a steady state assumption or a rapid equilibrium assumption, a second order rate law of the general form

$$\frac{d[P-P]}{dt} = k'[P]^2 \qquad (1)\ ^{65}$$

can be derived, where P—P is an oriented aggregate, P is a primary particle, and k′ is the combined rate constant.

Later molecular dimer models characterized equivalent particle size rather than the concentration of primary particles remaining and also include a calculated collision frequency.[127] Equivalent particle size is defined as the radius of a sphere with equivalent volume to the attached particles.[127] The main variables are often easy to measure: r_t and r_0 are the average equivalent radii at times t and 0, respectively, and $[P]_0$ is the initial concentration of primary particles. k is the rate constant and can be determined by experiment.

$$r_t^3 - r_0^3 = \frac{k[P]_0 t}{1+k[P]_0 t} r_0^3 \quad (2)$$

This model only accounts for the formation of dimers and is therefore most appropriate for early growth.[119, 127] Though Penn's model seemingly is also in this category, it has been used to successfully describe experimental results in the growth of goethite nanorods consisting of ca. one hundred primary particles,[49, 86-87, 119] while the size-based model approaches a final effective particle radius that is equivalent to all primary particles having undergone a single coalescence process.[127] Despite this limitation, it was successfully applied to model growth in previously published data on several types of nanoparticles, including SnO_2,[127] ZnS,[58] CdSe,[128] and InAs,[128] with particle sizes measured from TEM images (SnO_2), XRD patterns (ZnS), and photoluminescence data (CdSe and InAs).

A substantial step forward in modeling crystal growth by OA involved incorporation of the contribution to growth by coarsening. Indeed, evidence for simultaneous growth by coarsening and OA has been described for many systems,[58, 73, 106] including hydrothermal coarsening of titanium dioxide [16, 45, 100, 107] as well as iron oxides. [61, 85] Huang et al. described a growth process with two distinct steps—initial growth dominated by OA followed by further growth by coarsening.[58] When equations for volume weighted

average particle size are applied to the rate of particle attachment by OA, the full model for OA is

$$D_t = \frac{D_0\left(\sqrt[3]{2}kt+1\right)}{(kt+1)} \quad (3)$$

where k is the rate constant, t is time, and D_t and D_0 are the volume weighted average particle diameter at times t and 0. This model also only accounts for the formation of dimers, but when the coarsening component (not shown here) is also included it describes well the growth kinetics of ZnS,[58] ZnO,[129] and TiO_2[100] nanoparticles.

Population balance model

Drews et al.[130] include two types of primary particles—fresh primary particles that cannot aggregate and mature primary particles that become the building blocks of secondary crystals—in a model that was later extended to include an arbitrary number of intermediate states between "fresh" and "mature" primary particles.[115] Their models can also account for the higher-order coalescence of two secondary crystals. In the initial case, where only one intermediate state exists, a fresh primary particle (A) can age or evolve into a mature primary particle (B) with a rate constant k_1 by the mechanism $A \xrightarrow{k_1} B$. The mature primary particles (B) are partially transformed and thus able further transform into or attach to crystalline aggregates (C) by the processes $B \xrightarrow{k_2} C_1$ and

$B + C_i \xrightarrow{K_i} C_{i+1}$ where k_2 is the rate constant of transformation from B to C, the index i is the number of primary particles ultimately consumed in the formation of the crystal, and K_i is the kernel for attachment of a mature primary particle (B) with any crystal (C). Mature primary particles cannot aggregate with other mature primary particles. In Mechanism II of their paper, crystals (C) can also undergo higher-order coalescence, $C_i + C_j \xrightarrow{K_{ij}} C_{i+j}$, where i and j are both index numbers and K_{ij} is the kernel for attachment of two crystals.

A novel aspect of this model is its ability to describe a stepwise crystal size distribution when an intermediate stage exists (mature primary particles B) and higher-order coalescence between crystals C is slow. It can also be expanded to account for an unlimited number of intermediate states (B_1 to B_m), Derjaguin-Landau-Verwey-Overbeek (DLVO) interactions between particles, dissolution of primary particles and decreases in dissolution rates as primary particles age, and changes in coalescence rate as primary particles age.[115]

Polymerization model

A model based on stepwise polymerization[131-132] has been used to describe the formation of linear structures via OA.[120] In the polymerization model, a primary particle is considered to be a molecule constructed of the body of the nanoparticle (A) surrounded

by two active surfaces (S) in the configuration S—A—S. The assembly of particles into a larger structure

$$S - A - S + S - A - S \rightarrow S - AA - S \rightarrow S - (A)_x - S \qquad (4)$$

results in the elimination of two active surfaces with the coalescence of each primary particle (monomer) to a polymer or the coalescence of two polymers together. The overall reaction can be modeled as a second order rate law with respect to the concentration of reactive surfaces if the rate constant, *k*, is constant,

$$v = \frac{d[S]}{dt} = -k[S]^2, \qquad (5)$$

and as a third order rate law if the rate constant varies with time or particle size:

$$\frac{d[S]}{dt} = k_0'[S]^3. \qquad (6)$$

Here, k_0' is the initial value of a variable rate constant. This model assumes that each particle or secondary structure has only two active surfaces and that all secondary structures are linear arrangements of primary particles.[120] The results of this model were compared against experimental data on OA of SnO_2 colloids,[133] which highly disfavor growth via coarsening, TiO_2 nanoparticles,[45] and TiO_2 nanorods,[134] and found to fit all datasets well.[120]

Modeling simultaneous OA, coarsening, and phase transformation

Quantifying contributions to growth by simultaneously operating mechanisms presents a particular challenge.[82] Zhang and Banfield developed the two-step model, which described both the phase transformation of amorphous titania to anatase and the kinetics of particle growth in the product phase.[97] When dry titania particles are aged at elevated temperatures the particles are not free to rotate (as they would be in liquid suspension) and OA is a random event that only occurs when neighboring particles are already crystallographically aligned. Phase transformation initiates, or is nucleated, at a particle-particle interface produced by OA[14-16, 53] and the rate of growth via OA can be quantified from α, the weight fraction of nanoparticles transformed to the new phase and D_0 and D_t, the average diameters of nanoparticles in the new phase at time 0 and time t, respectively:

$$\ln\left[\frac{1}{(1-\alpha)(D_0/D_t)^3} - 1\right] = \ln k_{in} + \frac{m-1}{m}\ln t \qquad (7)$$

Additional variables in this model are k_{in}, the rate constant of phase transformation via interface nucleation, and m, an exponent representing grain growth behavior (generally between 2 and 4).[95]

Expanding the model enables quantification of the relative contributions to phase transformation by simultaneous dissolution-precipitation (coarsening) and interface nucleation.[75]

$$\frac{(D_t/D_0)^3}{(1-\alpha)} - 1 = \left(1 + \frac{k_{in}N_0}{k_{dp}}\right)\left(e^{k_{dp}t} - 1\right) \quad (8)$$

Here k_{in} is the rate via interface nucleation, k_{dp} is the rate via dissolution-precipitation, and N_0 is the initial number of primary particles. This model can be applied to a wide range of experimental conditions and can describe phase transformation at both extremes of nanoparticle solubility (low solubility: IN-dominated, high solubility: DP-dominated) and at intermediate levels of solubility in which IN and DP both play substantive roles. Notably, the relative contribution from each mechanism can be quantified with time. The contribution to phase transformation due to IN (R_{IN}) can be expressed a fraction of the rate due to all mechanisms (R_{TOT}): [75]

$$\frac{R_{IN}}{R_{TOT}} = \frac{k_{in}N_0 \cdot e^{-k_{dp}t}}{(k_{in}N_0 + k_{dp})} \quad (9)$$

Results of applying this model to phase transformation in iron oxides using Eq. 9 are shown in Figure 1.6. Aqueous suspensions of 6-line ferrihydrite (6lnFh) and 4 wt% goethite/96 wt% 6lnFh were aged at pH 5 and 90 °C. XRD was used to track the phase composition over time, and k_{in} and k_{dp} were calculated by applying Eq. 8 to the results.

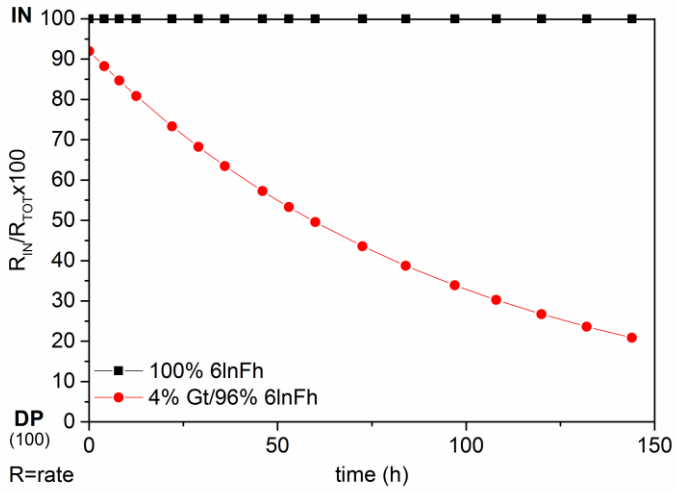

Figure 1.6: Quantifying phase transformation in suspensions of 6-line ferrihydrite (6lnFh) and 4 wt% goethite/96 wt% 6-line ferrihydrite (4% Gt/96% 6lnFh) aged at pH 5 and 90 °C.

Without the addition of goethite prior to aging, IN is the dominant mechanism by which goethite forms. In contrast, the addition of the more stable iron oxide, goethite, results in detectable and ever increasing contribution to phase transformation by DP (Figure 1.6). This makes sense since one would expect a significant solubility difference between the smaller 6lnFh nanoparticles and the larger and more stable goethite particles. However, IN still contributes substantively to the overall rate of phase transformation in this system.[135]

Thermodynamics

As with any chemical reaction, crystal growth processes have an activation energy barrier that must be overcome before growth can occur.[84, 87, 89] Growth may also occur if

an increase in crystal size is energetically favored.[15, 53, 61, 85, 136] The total Gibbs free energy of a nanoparticle is the sum of its surface free energy and bulk free energy,

$$\Delta G = \Delta G_S + \Delta G_B$$

where G is the Gibbs free energy, G_S is the surface Gibbs free energy, and G_B is the bulk Gibbs free energy. The total free energy of nanoparticles has significant contributions from surface energy due to their high surface area to volume ratios. When surface free energy contributes more to total free energy than bulk free energy does, total energy may be reduced by decreasing the surface area to volume ratio. As OA occurs, volume increases through the formation of new secondary crystals and surface area decreases through the elimination of surfaces at particle-particle interfaces.[53, 136] Coarsening can then fill in dimples left at particle-particle interfaces, further decreasing the surface area to volume ratio.[15, 61, 85]

Particle shape also has important implications for thermodynamic stability. Surface area to volume ratio changes dramatically when comparing particles with rough surface texture to spheres or those with neatly faceted faces. Different crystal faces have different energies.[137] Wulff constructions model equilibrium structures defined by the morphology with the minimum surface free energy, calculated as the product of surface energy and surface area of all exposed faces.[138] [126, 139] However, Wulff morphology cannot fully explain the variety of nanoparticles observed in natural and laboratory environments. The

use of elevated temperature in a synthesis, the failure of a synthesis to ever reach the equilibrium condition, alteration of surface energies due to adsorption or solvent interactions, and the incorporation of twins and growth of high-symmetry structures may all induce the formation of experimentally-observed non-Wulff morphologies.[137, 140]

Morphology and surface chemistry

In addition to affecting the stability of the primary particles, morphology can also affect their behavior when forming secondary structures. At the most basic level, particles with different shapes will assemble differently due to geometric constraints. The wide range of hematite crystals grown via OA is just one example of this, as shown in Fig 2.[44, 47, 76-78, 91] Equilibrium structures with smooth faces are also expected to behave differently than non-equilibrium structures or those with rough surfaces.[17]

Solvents and other chemical species often play an important role in directing growth by OA by adsorbing to nanoparticle surfaces to relax the energy of surface sites.[22] The extent of solvation depends on the energy of a particular crystal face and the thermodynamic stability of the mineral phase. For example, high-energy faces and thermodynamically stable phases (e.g., hematite) adsorb water more strongly.[22, 141]

When anatase (TiO_2) nanoparticle assembly was modeled using molecular dynamics, simulations of particles in vacuum revealed that they attach along their direction of approach, without further rotation or rearrangement, and form polycrystalline secondary

structures.[139, 142] However, when water vapor was included in the simulation, crystals underwent growth via OA. Hydrogen bonds formed between the surfaces of crystallographically aligned nanoparticles and the interparticle hydroxyls were eventually expelled to regenerate water and form direct Ti—O bonds.[142]

Simulations show that OA is more likely to happen along surfaces that have the greatest ability to dissociate water, consistent with experimental observations,[45, 142] even though these surfaces are usually not those that have the highest surface energy.[136] Although favoring the elimination of high energy surfaces may seem intuitive, the greater energy of solvation of high energy surfaces makes it more difficult to expose surfaces for particle-particle interactions[141] and low energy surfaces may be more reactive because adsorbates can desorb more easily.[45, 142-143] Adsorbates must desorb prior to assembly by OA or be incorporated as defects or impurities in the secondary structure,[49, 65, 144] so solvents that do not easily desorb or adsorbates that stabilize "too well" may inhibit assembly by OA.[86, 141-143, 145]

Face-dependent effects of solvents and additives have also been observed experimentally. In anatase nanoparticles, the energetic ordering of {001} vs {101} faces was reversed when synthesized from titanium butoxide at 250 °C in 110 mM NaF in oleic acid.[146] Not only did this have an effect on particle shape, the change in interfacial energy

also caused OA to occur most commonly on (001) faces,[146] rather than the {112} faces observed by Penn and Banfield after fluorine-free hydrothermal treatment of anatase.[45]

Forces governing assembly

Early work applied Derjaguin-Landau-Verwey-Overbeek (DLVO) theory to explain the role of particle-particle interactions in OA to reasonable success.[65, 67] DLVO theory considers both van der Waals attraction and electrostatic repulsion.[147-148] However, DLVO theory breaks down at distances of less than a few nanometers due to the near-complete overlap of the particles' electric double layers.[121] In cases of low electrostatic repulsion, particles may approach each other as the result of diffusion as modeled by Smoluchowski theory, but special solution conditions, such as high ionic strength, may be required to reach a level of repulsion low enough for this to occur.[121, 125] In sum, additional forces must be considered to explain the final steps of particle assembly.[149]

Electrostatic (Coulombic) forces are repulsive when two like-charged objects are considered (as is often the case in DLVO theory), but they can also be attractive when opposite charges are involved[150-151] and may be able to explain some aspects of particle assembly in OA.[61] A rapid jump to contact was observed in fluid cell TEM experiments after aligned particles came within ~1 nm of each other (a two- to four-fold increase in velocity), which only occurred when particles were crystallographically aligned.[61] The dependence on alignment suggests that electrostatic interactions play a role, as a

mismatch in the alignment of the crystal lattices would cause anion-anion and cation-cation repulsion and prevent assembly.[61] Though anisotropically polarized van der Waals forces cannot be ruled out, Coulomb interactions are hypothesized to be the source of this force[61] and molecular dynamics simulations have shown that Coulombic forces make the greatest energetic contribution to growth via OA in ionic crystals.[136]

Osmotic and solvation forces can be applied at distances of a few layers, or less, of solvent molecules.[61, 149] Solvation forces occur due to differences in ordering of solvent molecules between those in close proximity to nanoparticle surfaces and those in the bulk liquid.[149] Solvent molecules at particle surfaces or in confined spaces such as interparticle gaps transition from solid-like ordering to bulk solvent behavior as the distance from the particle surface increases. Smooth surfaces have a higher degree of solvent ordering, and therefore stronger solvation forces, than do rough ones.[123] The decrease in ordering with distance from a surface has been modeled previously in simulations,[123, 152-153] and detected experimentally with crystal truncation rod modeling of X-ray reflectivity measurements, e.g. on goethite (100)[72] and mica (001)[154] surfaces. Solvation forces can cause particle to rapidly align in configurations with free energy minima and may be more significant in directing nanoparticle alignment and assembly than van der Waals interactions.[123] They can also stabilize colloids, sometimes so strongly that particle-particle attachment will not occur.[149]

Future Work

The widespread global presence of iron oxides and the importance of these minerals to global iron cycling, biological processes, and industry makes understanding their growth and phase transformation critical for advances in many areas of study. Both growth and phase transformation in iron oxide nanocrystals occur via multiple, competing mechanisms. The relative contributions to crystal growth by these mechanisms can change dramatically with conditions, such as pH, solubility, crystallite size, and phase composition. Likewise, phase transformations also occur via competing mechanisms, such as the IN and DP mechanisms described above. Furthermore, as the particle size distribution and phase composition evolves with time, the relative contributions similarly evolve. For example, phase transformation initially dominated by IN may have increasing DP character with time, and crystal growth initially dominated by OA may become dominated by coarsening as the average crystal size increases. These competing, dynamic mechanisms make characterization and modeling of iron oxide growth difficult and advances in understanding are all the more rewarding.

One of the hallmarks of OA is unique crystal shapes and symmetry-defying morphologies. Textured surfaces and atomic-level defects are common in crystals grown via OA, and yet none of the above characteristics can be used to definitively identify that OA has occurred. Dimples can be filled in by coarsening, defects can be erased through

recrystallization, and the unique crystal shapes of OA can also be due to other growth mechanisms, such as random aggregation followed by recrystallization. Instead, a multi-technique approach is required and the growth process must be examined holistically.

Modeling crystal growth and phase transformation is one method for detecting OA. Several models exist, such as the simple dimer formation model or the combined IN and DP model. Further advances in modeling may lead to a predictive understanding of crystal growth and phase transformation in iron oxides. Ideally, detailed knowledge about iron oxide crystal growth will facilitate improved understanding of past and predictions of future behavior of geologic materials as well as enable purposeful control of crystal growth and phase transformations in synthetic conditions to produce nanoparticles with desired properties. Advances in understanding growth and phase transformation are expected to be generalizable, leading to predictions and synthetic control in other nanocrystalline materials.

A better understanding of thermodynamic vs. kinetic control of OA would also lead to further tuning of nanocrystalline materials. Thermodynamic control is important for producing nanoparticles with equilibrium structures, which are often related to Wulff morphologies, while kinetic control is important for the synthesis of non-equilibrium structures. Is OA, with its distinctive symmetry-defying morphologies, under thermodynamic or kinetic control and how can reaction conditions be tuned to favor one

pathway over the other? Synthetic control could also be furthered by better understanding the forces that govern assembly and attachment of particles. Finally, modeling growth by OA in complex systems, including mixed-phase precursors and situations where other growth mechanisms play a prominent role, would also benefit from additional development. Though the understanding of crystal growth by OA has advanced tremendously since it was first described as such in 1998, many fundamental questions remain and this is a rich area for future research.

Chapter 2 : Transformation and growth of hematite from 2-line ferrihydrite

Jennifer A. Soltis,[1] Benjamin Gilbert,[2] Joshua M. Feinberg,[3] R. Lee Penn*[1]

[1]Department of Chemistry, University of Minnesota, Minneapolis, Minnesota 55455, United States
[2]Earth Sciences Division, Lawrence Berkeley National Laboratory, Berkeley, California 94720, United States
[3]Institute for Rock Magnetism, N. H. Winchell School of Earth Sciences, University of Minnesota, Minneapolis, Minnesota 55455, United States

Introduction

Iron is the most abundant transition metal in the Earth's crust and is required for many life processes. Iron sequestration into, and release from, iron-bearing minerals plays important roles in the movement of iron and energy through the environment. The iron biogeochemical cycle includes a diversity of chemical transformations, from iron precipitation as oxides, sulfides, or other solids to dissolution of iron-bearing solids; transport as dissolved species through soils and groundwater; and abiotic and biotic redox reactions (e.g., biotic reduction by *Geobacter* and *Shewanella*[155-157] and oxidation by *Gallionella* and *Leptothrix*[158] bacteria).

Iron oxide and oxyhydroxide minerals, referred to collectively as the iron oxides, generally have high redox reactivity, high surface activity, and high surface area (frequently >100 m^2/g, even for naturally occurring deposits).[23] At all stages of iron oxide growth and phase transformation, these minerals can adsorb and desorb heavy metals and arsenic,[11, 30, 159] facilitate reduction-oxidation reactions at their surfaces,[158, 160] dissolve and re-precipitate,[53, 161] and grow into larger structures.[53] Changes in accessible surface area and surface chemistry due to growth and mineral phase transformations affect the chemical behavior of these minerals in environmental systems. Redox reactivity, [162]

solubility,[163] and interactions with heavy metals[13, 21] are just three of many processes that can be affected.

The hydrous ferric oxide ferrihydrite (Fh, $Fe_5HO_8 \cdot 4H_2O$)[23] is a common early product of both biotic and abiotic precipitation.[23, 161] Fh is a poorly crystalline material that occurs only at the nanoscale and is widely present in the crust, soils, and freshwater and marine systems.[161] Fh is typically classified by the number of peaks observed in its X-ray diffraction patterns, e.g. 2-line or 6-line. It is a precursor to other more crystalline iron oxides, such as hematite (Ht, Fe_2O_3) and goethite (Gt, α-FeOOH), two of the three most abundant naturally-occurring iron oxides, and is metastable with respect to these minerals.[22-23, 161] Ferrihydrite, goethite, and hematite all share a common framework of hexagonally close-packed oxygen atoms, which supports the idea of pseudomorphic transformations among the three materials.[23] In fact, early work in the crystallography of ferrihydrite hypothesized that it was an extremely defect-laden form of hematite,[164] and there still is no consensus about its exact structure, or how it relates to the structure of hematite.[165-173]

Understanding phase transformations in iron oxides is important for understanding their past and predicting their future interactions with the environment. For example, ferrihydrite is only found in deposits dating from the Pleistocene or younger (<2.6 mya) because older deposits have already undergone phase transformation into thermodynamically more stable minerals.[161] Two important mechanisms of phase transformation are closely linked to mechanisms of crystal growth. Indeed, phase transformation and crystal growth often occur simultaneously, and it can be difficult to separately characterize each of the contributing mechanisms.[174] Phase transformation by

dissolution precipitation (DP) is similar to crystal growth by coarsening, with the mass fraction of the more stable phase increasing at the expense of the dissolving phase. Transformation by interface nucleation (IN) occurs when the new crystal phase nucleates at the interface between two surfaces. Recrystallization then occurs as a solid-state process that involves propagation of the new phase through the remaining volume of precursor crystals.[95] This may be induced by oriented or slightly misoriented alignment of two precursor crystals at a particle-particle interface, similar to the assembly of crystallographically-aligned particles in growth by oriented attachment (OA).[15] OA is a non-classical crystal growth mechanism in which smaller crystals align in a crystallographically ordered manner prior to forming larger crystals[14, 65, 67] and has been found to occur in a wide range of mineral systems,[44, 65, 68, 175-180] including the iron oxides.[66, 68, 181] Just as coarsening and OA typically both operate simultaneously but to different extents during crystal growth, so can DP and IN during phase transformation.[75, 98, 182]

The transformation from ferrihydrite to both goethite and hematite has been well studied and is dependent on the nature of the Fh (e.g., 2-line vs. 6-line), temperature,[23, 89, 183-185] pH,[86, 88, 183, 186] and other synthesis conditions.[84, 87-88, 183, 187-188] For example, at low pH levels, the growth of goethite nanorods from a 6-line Fh (6lnFh) precursor occurs via a multi-step mechanism in which primary particles first phase transform and then undergo OA.[66, 85] Though OA is the dominant growth mechanism in the growth of goethite from 6lnFh at low pH, the progressive loss of features like dimples on particle surfaces is evidence for additional growth by coarsening.[85] On the other hand, goethite growth at high pH is dominated by dissolution-precipitation.[88]

Phase transformation and growth can also occur when the starting material first assembles into larger structures, then transforms to the new phase, as in the transformation from akaganeite to hematite.[79] Many iron oxides exhibit size-dependent phase stability, in which changes in particle size and surface area:volume can increase or decrease total free energy.[22, 189] Phase transformation to hematite is favored when akaganeite particles reach a critical size at which the combined bulk and surface Gibbs free energy of the akaganeite particles is greater than that of hematite particles of similar dimensions.[79] A complete picture of the factors favoring one growth mechanism over another, or the order of aggregation and phase transformation, remains elusive.

Elucidating growth and phase transformation mechanisms for more poorly crystalline 2-line ferrihydrite (2lnFh) presents additional challenges due to difficulties associated with imaging poorly-crystalline material, the ongoing uncertainty over its exact crystal structure,[165-169] and an inability to quantify the material via Rietveld refinement of X-ray diffraction (XRD) patterns. Much past research in phase transformation has drawn heavily upon these techniques (e.g., kinetics of ferrihydrite to goethite transformation based on transmission electron microscopy (TEM),[48, 87] kinetics and mechanism of phase transformation in titania polymorphs based on XRD data,[95, 101, 182] and kinetics and mechanism of phase transformation from akaganeite to hematite using data from both XRD and TEM[79]).

Low temperature magnetometry is a complementary technique that relies on the use of superconducting quantum interference device (SQuID) sensors to measure induced and/or remanent magnetization of a sample. Low temperature magnetometry has been an important tool in the Earth and materials sciences that has been so far underused in

studies on the fundamentals of nanoparticle growth and phase transformation. Magnetic measurements can provide information about thermally-dependent transitions that are diagnostic of mineral identity and can also be used to estimate average particle sizes and the degree of structural order or crystalline defects in a sample.[190-193] SQuID sensors are also exquisitely sensitive to small amounts of magnetic material, particularly for ferromagnetic materials, and can detect mineral concentrations at levels far lower than XRD methods.

In this study, we employ conventional and cryogenic transmission electron microscopy, X-ray diffraction, oxalate dissolution, and low temperature magnetometry to elucidate the mechanism of 2lnFh to hematite phase transformation. Magnetic measurements in particular lend critical insight into this system, showing the hematite crystals were present at smaller sizes and lower quantities than detected before, and that 2lnFh particles possibly undergo phase transformation before assembly into large hematite crystals.

Materials and methods

All labware was washed in 4 M nitric acid and triple-rinsed with Milli-Q water (Millipore, 18.2 MΩ·cm resistivity) prior to use. Milli-Q was also used for all solutions and dialysis procedures.

Hematite was synthesized following a procedure adapted from Schwertmann and Cornell, Method 6.[41] First, 2-line ferrihydrite (2lnFh) was synthesized. While stirring, 300 mL of 0.89 M potassium hydroxide (Mallinckrodt) was added to 500 mL of 0.20 M ferric nitrate (Fisher) in 100 mL aliquots. An additional 200 mL of Milli-Q water was added with sufficient oxalic acid dihydrate (J. T. Baker/Mallinckrot Baker) to a produce a

suspension with a total oxalate concentration of 2 mM. The rich brown suspension was stirred for an additional three minutes.

The final suspension was placed into dialysis tubing (Spectra-Por #7 dialysis tubing, MWCO = 2000 g/mol) and dialyzed against Milli-Q water while refrigerated at 10°C. No more than 250 mL of ferrihydrite was dialyzed per 2 L of Milli-Q water. Water was changed every 1-2 hours for four changes and every four hours for two additional changes. The samples were left in dialysis overnight following the final water change. Dialyzed suspensions were combined and pH adjusted with potassium hydroxide solution such that the final pH was 6.5 when the suspension was mixed with equal volumes of Milli-Q water (pH ~5.7).

Samples were aged in a water bath at 90 °C, unless otherwise noted, in a series of 15 mL centrifuge tubes. Each tube was filled with 2.5 mL of Milli-Q water, tightly capped, and placed in the water bath. When the water temperature had reached 90 °C, 2.5 mL of room-temperature 2lnFh stock suspension was added to each tube. Tubes were quickly uncapped and re-capped during this process to minimize vapor loss. The hot injection step was performed at a rate of three tubes per minute, and the time of 2lnFh addition was recorded after every third tube so that the aging time could be adjusted to compensate for the time required perform the hot injection step on each tube.

The temperature of the suspensions was monitored by thermometers placed into three additional tubes prepared by the hot injection technique, and these samples reached 90 °C less than fifteen minutes after the injection of 2lnFh stock suspension into the hot water. These tubes were equipped with caps that fit closely around the thermometers to prevent changes in temperature due to evaporative cooling.

Three sealed centrifuge tubes were removed from the water bath at each designated sampling time and immediately plunged into an ice bath. Cooling to room temperature or lower took less than four minutes for all samples. Each sample was split into two aliquots: one for analysis via oxalate dissolution and one for drying. The dry samples ranged in color from dark brown (initial) to reddish-orange (final).

Two additional samples of 2lnFh were prepared with the dialysis step omitted, one with and one without 2 mM oxalate. These samples were freeze dried by freezing using liquid nitrogen immediately after synthesis and drying under vacuum in a lyophilizer.

Characterization Methods

X-ray Diffraction

Dried samples were ground with an agate mortar and pestle and front packed into an aluminum sample holder fitted with a zero-background quartz window. X-ray diffraction (XRD) patterns were collected with a PANalytical X'Pert Pro MPD theta-theta diffractometer with a cobalt K-α source (wavelength 1.79 Å) and an X'Celerator detector over the range of 20-80° 2θ. The experimental results were compared with the reference powder diffraction file (PDF) for hematite (#33-664). 2lnFh does not have a PDF on file with the International Center for Diffraction Data, but it can be identified by the presence of two broad peaks centered at approximately 1.3 and 2.2 Å.[165-169]

Line broadening analysis was performed by applying the Scherrer equation[194] to the full width half maximum measurements of selected peaks obtained from fitting in X'Pert HighScore Plus. Past work using this instrument indicates that a first standard deviation of 10-20% of the calculated particle size is typical when replicate measurements are made of the same sample.[100-101]

Synchrotron Diffraction

Wide-angle X-ray scattering (WAXS) data were collected at 90 keV (wavelength 0.1080 Å) from powdered samples placed inside hollow Kapton tubes at beamline 11-ID-C of the Advanced Photon Source (APS) at Argonne National Laboratory using a Mar 2D image plate detector. Between 10 and 15 two- or five-minute exposures from an empty tube and each sample were acquired, respectively. The program Fit2D[195] was used to calibrate the detector geometry using data acquired from a Si standard to bin each 2D pattern onto a 1D q axis, where $q = 4\pi \sin\theta / \lambda$, q is the momentum transfer, θ is the scattering angle in degrees, and λ is the wavelength of radiation. The WAXS patterns were scaled prior to subtraction to reveal structural changes with time.

Preferential dissolution/UV-vis

The method for the preferential dissolution of poorly-crystalline iron oxides by ammonium oxalate was adapted from the *Soil Survey Laboratory Methods Manual (SSLMM)*, protocol 4G2a1a2.[196]

Aliquots of each suspension were diluted 1:10 with 0.2 M pH 3 ammonium oxalate buffer (oxalic acid (JT Baker) and ammonium oxalate (Sigma Aldrich)) into microcentrifuge tubes and allowed to sit in the dark in an ice bath for three minutes. The cold temperature and dark conditions were chosen to prevent dissolution of the more crystalline iron oxides, such as hematite.[197] The digested samples were then removed from the ice bath and centrifuged for six minutes. The supernatants were collected and analyzed via ultra violet-visible (UV-vis) spectroscopy. The ammonium oxalate buffer and digested samples were stored in a refrigerator and used or measured within 48 hours to minimize growth of microorganisms.[196]

Supernatants were loaded into 1 cm quartz cuvettes, and the absorbance of 430 nm light was measured using an Agilent 8453 UV-vis spectrometer.[196] For solutions too dilute for colorimetric measurements with oxalate, a modified ferrozine assay was performed. The solutions were diluted 1:10 in Milli-Q water, and 100 μL of the diluted solution was added to 900 μL of the ferrozine assay solution, which contained 500 ppm ferrozine (Acros) in 0.2 M ammonium acetate (Fluka) and 5 mM ascorbic acid (Acros). Each sample was prepared in triplicate, and absorbance was measured at at 562 nm. The addition of ascorbic acid results in the reduction of dissolved Fe(III) to Fe(II), which makes the assay sensitive to total iron, rather than selective to Fe(II).[198] The dissolved iron in these solutions is expected to be entirely Fe(III).

In both cases, calibration curves were constructed from absorbance measurements of ferric nitrate standard solutions in oxalate buffer or the ferrozine assay solution.

Transmission Electron Microscopy

Transmission electron microscopy (TEM) images were collected using an FEI Tecnai T12 microscope operating at 120 kV or an FEI Tecnai G^2 F30 microscope operating at 300 kV. Both microscopes are equipped with Gatan charge-coupled device (CCD) cameras and use Gatan Digital Micrograph v3 to process images. Further image analysis was performed using ImageJ (v1.43m and later), a public domain NIH image processing and analysis program written by Rasband.[199] Specimens were prepared by diluting 20 μL of sample into 3 mL of Milli-Q water, sonicating for 30 seconds, and placing a single drop of diluted suspension onto the carbon-coated side of a 200 mesh Cu holey carbon grid (Structure Probe, Inc.). Grids were allowed to dry under ambient temperature and humidity.

Cryogenic (cryo) TEM specimens were prepared using a Vitrobot (FEI Mark IV) under 100% relative humidity. A 2lnFh suspension aged at 90 °C for 6 h was previously quenched in an ice bath and taken directly to the microscopy preparation lab. One specimen was vitrified without further treatment. The second was treated via the oxalate dissolution process as described above and vitrified 7 minutes after mixing with oxalate buffer (samples prepared for Fe(III) analysis had a total exposure time to oxalate buffer of 9-10 minutes).

Three microliters of suspension were placed onto a 200 mesh Cu lacy carbon grid (Structure Probe, Inc.), blotted with filter paper for 2 seconds, and plunged into liquid ethane (-183 °C) to vitrify the water and form a relatively electron-transparent solid. The grid was then transferred to a storage box held under liquid nitrogen (-178 °C). All subsequent handling of the prepared grids occurred under liquid nitrogen to maintain cryogenic conditions. Samples were imaged using an FEI Tecnai G^2 F30 TEM fitted with a cryogenic sample stage and operated at 300 kV. Images were collected with a Gatan charge-coupled device (CCD) camera using Gatan Digital Micrograph.

Preparation of samples for magnetic measurements

The dried, ground samples were prepared for magnetic measurements after XRD patterns had been collected. At least 100 mg of each sample was tightly packed into a gelatin or cellulose capsule. Powdered sugar was used as filler material to prevent unwanted vibration in samples with low sample volume. The sample capsules were tared before loading and massed before the addition of powdered sugar to obtain accurate iron oxide mass measurements.

Magnetic measurements

All magnetic measurements were performed at the Institute for Rock Magnetism, University of Minnesota, using a Quantum Designs Magnetic Properties Measurement system instrument (MPMS-5S). Samples were first imparted with a 2.5 T room temperature saturation remanent magnetization. The 2.5 T field was then turned off and the intensity of the remanent magnetization was measured during cooling from room temperature to 20 K and then back to room temperature in the presence of either a ±5 mT DC field. While it is possible to collect measurements in the MPMS using a "zero-field" environment, in reality there are often small, temporally variable residual fields that can create unwanted induced magnetizations in magnetic samples. It is possible to minimize these residual fields to a value <0.5 mT prior to the beginning of an experiment; however, this calibration process is time consuming and is often rendered inaccurate after a 2.5 T field is produced. The 5 mT DC fields used in this study allow us to create a controlled, repeatable magnetic environment in which to measure the samples. An example of raw data as collected from the SQuID magnetometer is shown in Figure 2.1a.

Magnetic data collected during thermal cycling were then fitted with a Curie-Weiss Law relationship. There are several formulations of the Curie-Weiss relationship and here we used the following, which is optimized for data collected right up to a material's blocking temperature,

$$M = a/(T - b)^c$$

where the specimen's magnetization, M, is defined as the inverse relationship with temperature, T. The coefficients a, b, and c are parameters that are fit to the data. Earlier studies on the magnetic properties of similar superparamagnetic ferrihydrite calculated

blocking temperatures of ~ 35 K.[200-201] A Curie-Weiss relationship was fitted to data collected between 55 and 130 K, which corresponds to the interval that showed the most pronounced effects of ferrihydrite's magnetic blocking. It also avoided any data contamination from hematite, which is thought to only have a minor defect moment at temperature below the Morin transition.

If the ferrihydrite samples in this study were simply collections of superparamagnetic ferrihydrite, then the Curie-Weiss relationships would fit the data above 130 K very well. However, as can be seen in Figure 2.1b, the Curie Weiss relationship does not fit all of the data at temperatures above 130 K. The difference between this theoretical magnetic behavior and the data is primarily the effect of trace quantities of hematite in the sample. Figure 2.1c shows an example of the how the magnetic data were processed and how a non-specialist in magnetic methods should interpret the results. Changes in slope or hysteresis between the cooling and heating curves observed in the 240-265K range indicate Morin transitions associated with hematite grains ≥100 nm, while those in the 165-230K range indicate the Morin transitions for grains ≤90 nm.

Results and Discussion

Major phase composition

XRD results (Figure 2.2) demonstrate that the amount of hematite increased and ferrihydrite decreased with time at 90 °C, until the sample consisted of pure hematite. In the un-aged (0 h) sample, only 2lnFh peaks are visible. Low-intensity peaks for hematite are first visible after 2.5 h of aging, and only hematite peaks are present after 10 h. Some, but not all, samples had detectable hematite after 2 h of aging. The color of the nanoparticle suspensions changed from dark brown to red orange as hematite content increased.

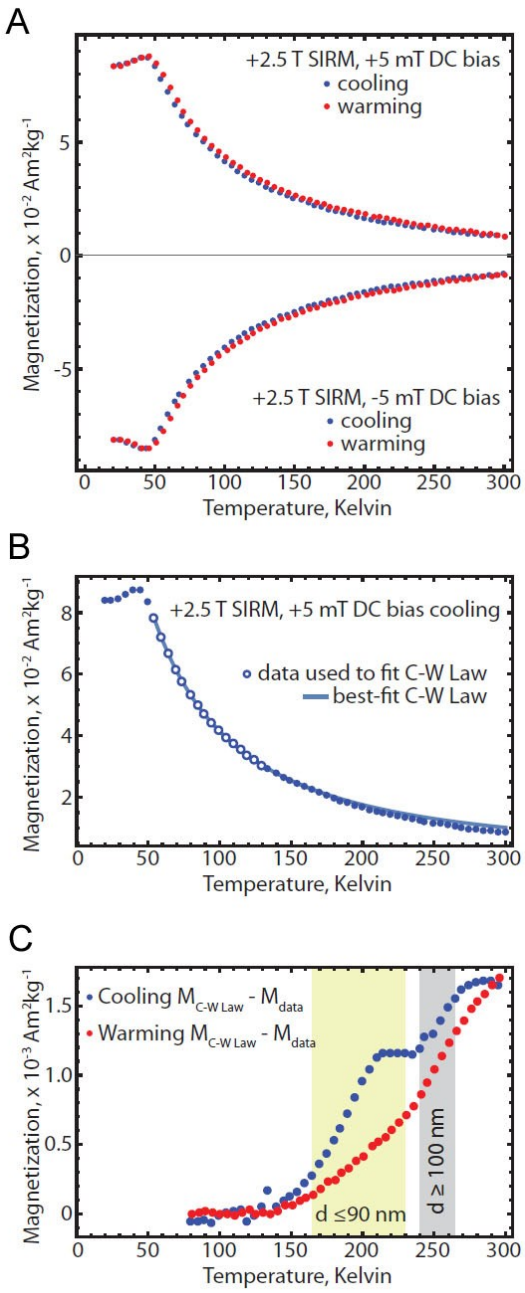

Figure 2.1. An explanatory figure to demonstrate how magnetic data is processed. (A) The raw data as it is collected from the SQuID magnetometer. The 2.5 T room temperature saturation magnetization is measured during thermal cycling from 300 to 20 to 300K in the presence of a positive or negative 5 mT DC bias field. (B) An example of fitting a Curie-Weiss relationship to a subset of the data that is detected almost entirely by the superparamagnetic ferrihydrite in the sample. (C) The residual magnetization in the sample (+5 mT DC bias) after the contribution to magnetization from ferrihydrite has been removed. The dark gray box shows the 240-265K range of observed Morin transitions for grains ≥100 nm.[192] The yellow box shows the 165-230K range of observed Morin transitions for grains ≤90 nm.[192]

XRD patterns further demonstrate that the hematite crystal size increases with aging time. The size of the crystals along several crystal directions, quantified by XRD line broadening analysis using the Scherrer equation,[194] are shown as a function of aging time in Figure 2.3. Measurements from experiments performed using two batches of 2lnFh show an increase in crystal size along the Ht (012), (104), and (110) planes and are in good agreement.

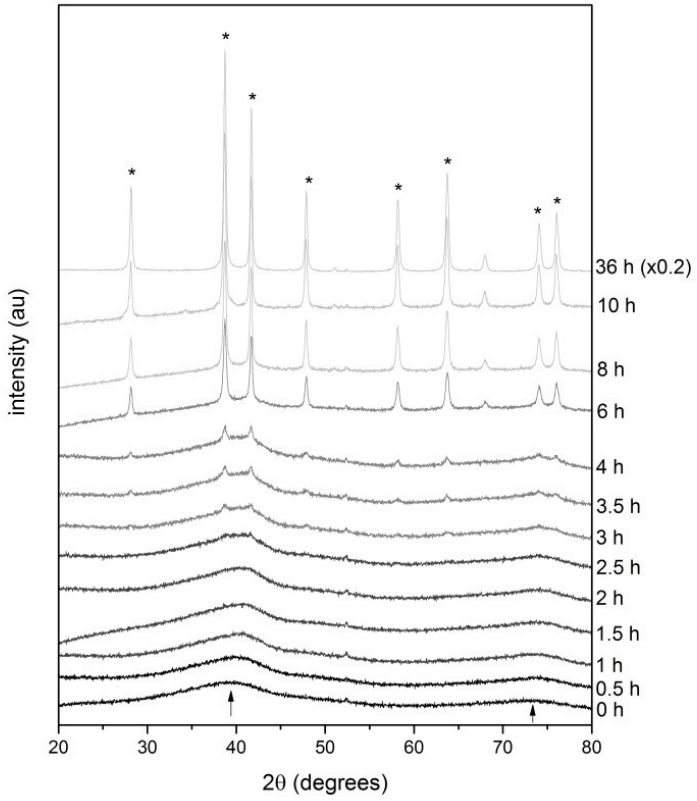

Figure 2.2. X-ray diffraction patterns of samples collected after aging a suspension of 2-line ferrihydrite at pH 6.5 and 90 °C for 0-10 h. Co K-α radiation was used to collect the patterns. Diffraction peaks for 2-line ferrihydrite are indicated with arrows (no PDF). Peaks for hematite are indicated with * (PDF #33-664). Peaks at 53 ° 2θ are background peaks from the Al sample holder. Patterns are vertically offset for clarity.

Synchrotron X-ray diffraction measurements are also consistent with increasing hematite content (Figure 2.4). Difference patterns were obtained by subtracting the synchrotron diffraction pattern of an unheated 2lnFh sample from the patterns for aged

samples (0.5-4.0 h). The small shoulder at ca. 2.4 $Å^{-1}$ after 2.5 h of aging is the first indication of hematite in the sample, and this shoulder coincides with the most intense of the peaks (at 2.3 $Å^{-1}$) in the synchrotron diffraction pattern of pure hematite, which is shown at the bottom of Figure 2.4. The hematite peaks beginning to emerge in the difference patterns can be compared to the diffraction pattern for pure Ht aged for 36 h (not a difference pattern) at the bottom of the figure.

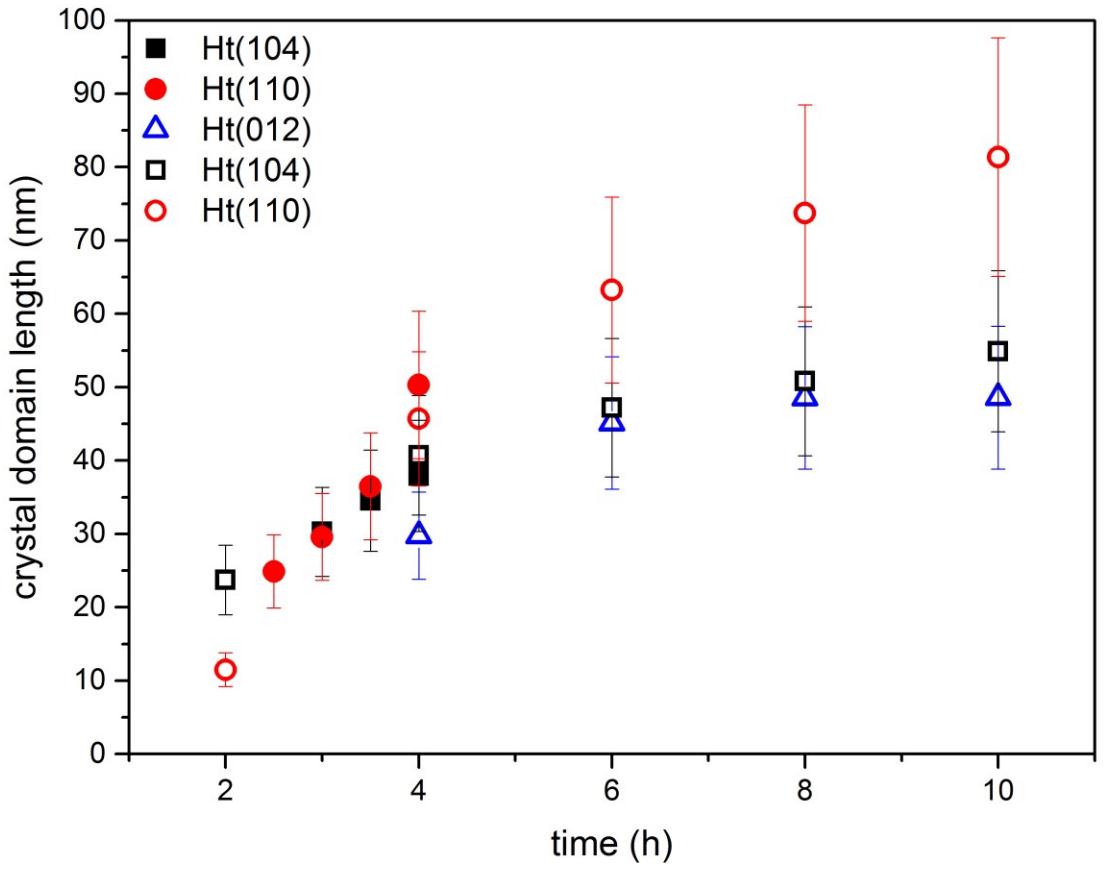

Figure 2.3. Hematite crystal domain lengths along (012), (104), and (110) as a function of aging time, with two different batches of ferrihydrite (open and closed symbols) used as the starting material. Error bars represent 20% of the calculated domain length and approximate the first standard deviation.[100-101]

X-ray diffraction methods typically have detection limits of ca. parts per thousand, at best. Thus, magnetic measurements, which can have substantially lower detection limits,

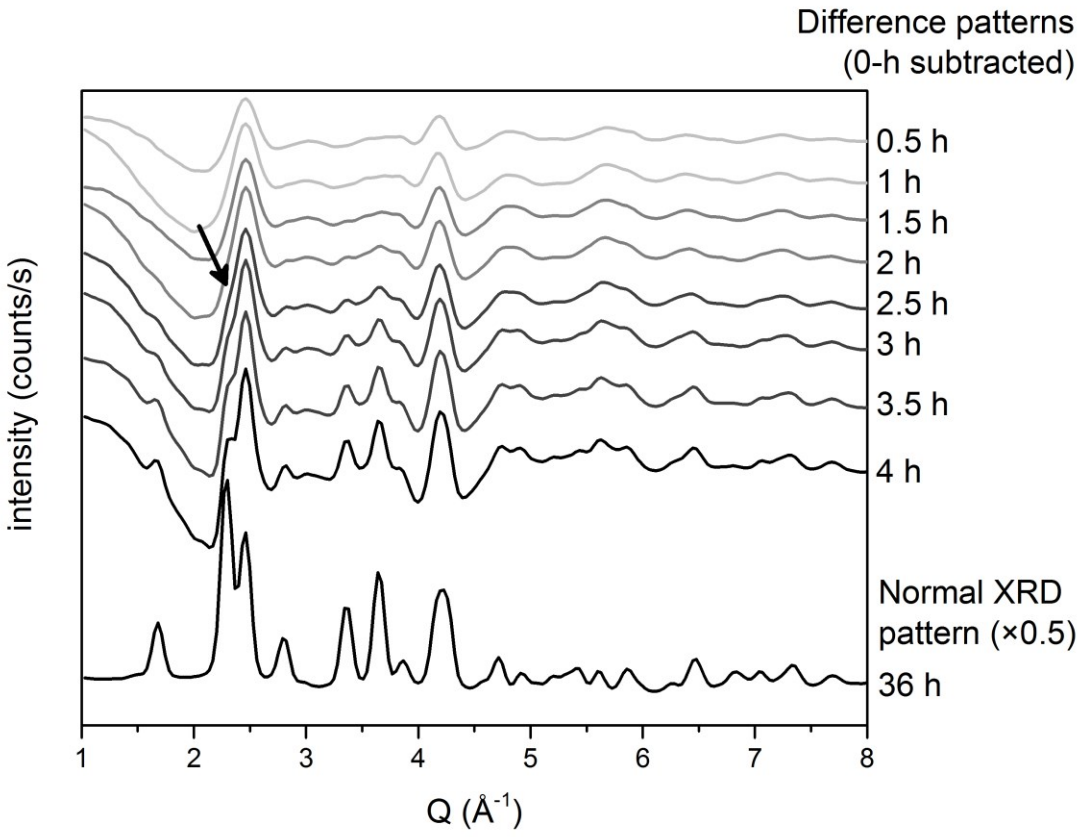

Figure 2.4. Synchrotron X-ray diffraction patterns of 2-line ferrihydrite aged at pH 6.5 and 90 °C. The pattern for pure hematite (aged for 36 h) is shown at the bottom. Difference XRD patterns for samples aged 0.5-4 h are shown above and were calculated by subtracting the 0-h pattern from the measured pattern for each aged sample. The first visible shoulder, indicating the presence of a small amount of hematite, is marked with an arrow in the 2.5-h sample.

were employed to quantify hematite in samples collected at earlier times. Hematite can most clearly be observed in low temperature magnetometry by its Morin transition (T_M), which is observed as a sudden decrease in magnetization during cooling as magnetic moments change from oriented within the mineral's basal plane at temperatures $>T_M$ to oriented normal to the basal plane at temperatures $<T_M$. There is a grain-size dependence to the Morin transition, with grains ≥100 nm displaying magnetization loss between 240-265K, while grains ≤90 nm yield T_M between 165-230K.[192] In general, T_M also shifts to lower temperatures when particles have high internal strain, high surface to volume

ratios, are doped with non-Fe cations, or have high levels of defects.[191] Finally, hematite grains that are exceedingly small or defect-rich can exhibit significant thermal hysteresis in T_M between heating and cooling.[192]

As with the XRD results, magnetic measurements show the mass fraction of hematite increased with aging time. Magnetization curves for 2lnFh synthesized and aged under different conditions are displayed in Figure 2.5. Magnetic measurements demonstrate that suspensions of ferrihydrite prepared with 2 mM oxalate, air-dried, and aged at 90 °C for 0-3 h show that hematite content, particle size, and crystallinity increase with time (Figure 2.5c-f). Each of the aged samples displays Morin transitions that are consistent with hematite grain size distributions include both larger grains (≥100 nm) that would produce standard T_M as well as smaller grains (≤90 nm) that would produce depressed T_M values. The magnetic contributions from small grains are more significant in samples aged for shorter times. It is also notable that the difference between the cooling and heating cycles becomes negligible as aging times increase. In similar syntheses, the earliest formation of hematite detectable via XRD did not occur until the suspension had been aged for 2.5 h.

Both air-drying and the use of oxalate during synthesis were found to increase the amount and crystallinity of hematite formed. A T_M, albeit with very low magnetization, is identifiable even in the oxalate-free, freeze-dried 2lnFh sample (Figure 2.5a), showing that a trace amount of small, defect-rich hematite nanoparticles is present in the as-synthesized Fh. This demonstrates that hematite is nucleating during the synthesis of the 2lnFh precursor at levels that were undetectable by either X-ray diffraction technique.

Oxalate is commonly used in hematite syntheses and may promote hematite formation.[41, 84, 202] The addition of 2 mM oxalate to a 2lnFh synthesis that was subsequently freeze-dried increased the amount of hematite formed and decreased its level of crystal defects (Figure 2.5b), and air-drying a similar suspension further increased the amount and crystallinity of the hematite produced (Figure 2.5c). This can be seen by an increase in residual magnetization and the amount of hysteresis between cooling and heating. We conclude that some phase transformation occurred during the days-long air-drying process.

Increased magnetization at ca. 120 K, which was observed in several of the samples, corresponds with the Verwey transition diagnostic of magnetite (Fe_3O_4).[190] Due to magnetite's strong ferrimagnetic character, signals of this amplitude may be due to the presence of only a single grain of magnetite. There was no source of Fe(II) in the 2lnFh synthesis and very low quantities of compounds with any reducing capacity (2 mM oxalate). Additionally, all syntheses and reactions were performed in air, making the formation of magnetite during synthesis unlikely. Therefore, the magnetite signal is attributed to very low levels of contamination (e.g., one to several nanoparticles).

Particle shape and aggregation state

TEM images (Figure 2.6) of samples aged for 0-6 h also show that hematite content increases with aging time. Initially, little diffraction contrast is observed in the large aggregates of primary particles, and diffraction contrast of the primary particles increases with aging time. The un-aged and 2-h sample are very similar in appearance, even though magnetic results indicate that small hematite particles are present in greater amounts after aging. After three hours, hematite particles were visually identifiable in the images.

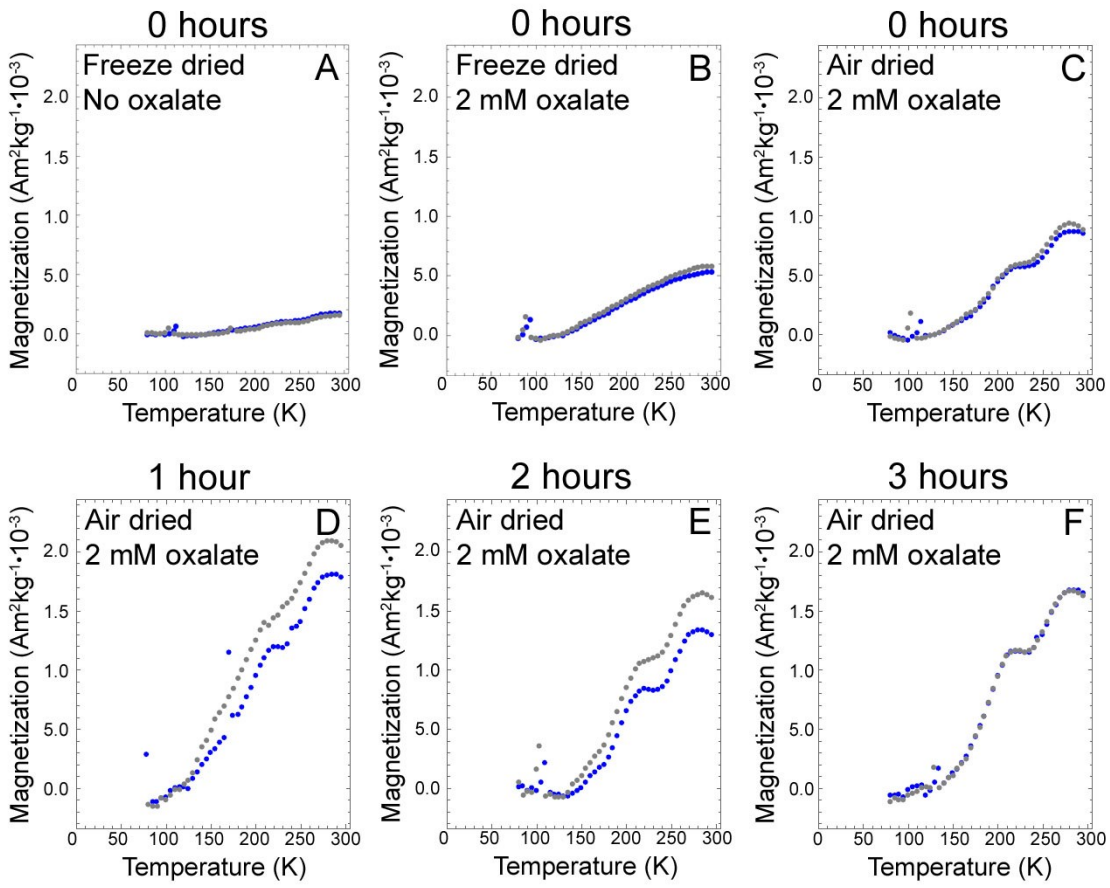

Figure 2.5. Temperature vs. residual magnetization upon cooling (grey dots) and heating (blue dots) for differently aged 2-line ferrihydrite. Top row: Samples prepared without any aging at elevated temperature. Left: 2lnFh prepared without oxalate and freeze dried immediately after synthesis. Middle: 2lnFh prepared in the presence of 2 mM oxalate and freeze dried immediately after synthesis. Right: 2lnFh prepared in the presence of 2 mM oxalate, dialyzed at 10 °C for 24 h, and air dried at room temperature. Bottom row: 2lnFh prepared in the presence of 2 mM oxalate, dialyzed at 10 °C for 24 h, aged for 1-3 h at 90 °C, and air dried at room temperature.

Lattice fringes visible in the high-resolution image (Figure 2.6, middle right) have spacing consistent with hematite (012) planes. Though the hematite particles appear to have a wide range of morphologies, they are relatively monodisperse, and a tilt series of TEM images showed that a single particle could appear rhombahedral, hexagonal, or irregularly shaped depending on its orientation relative to the electron beam (Figure 2.S2).

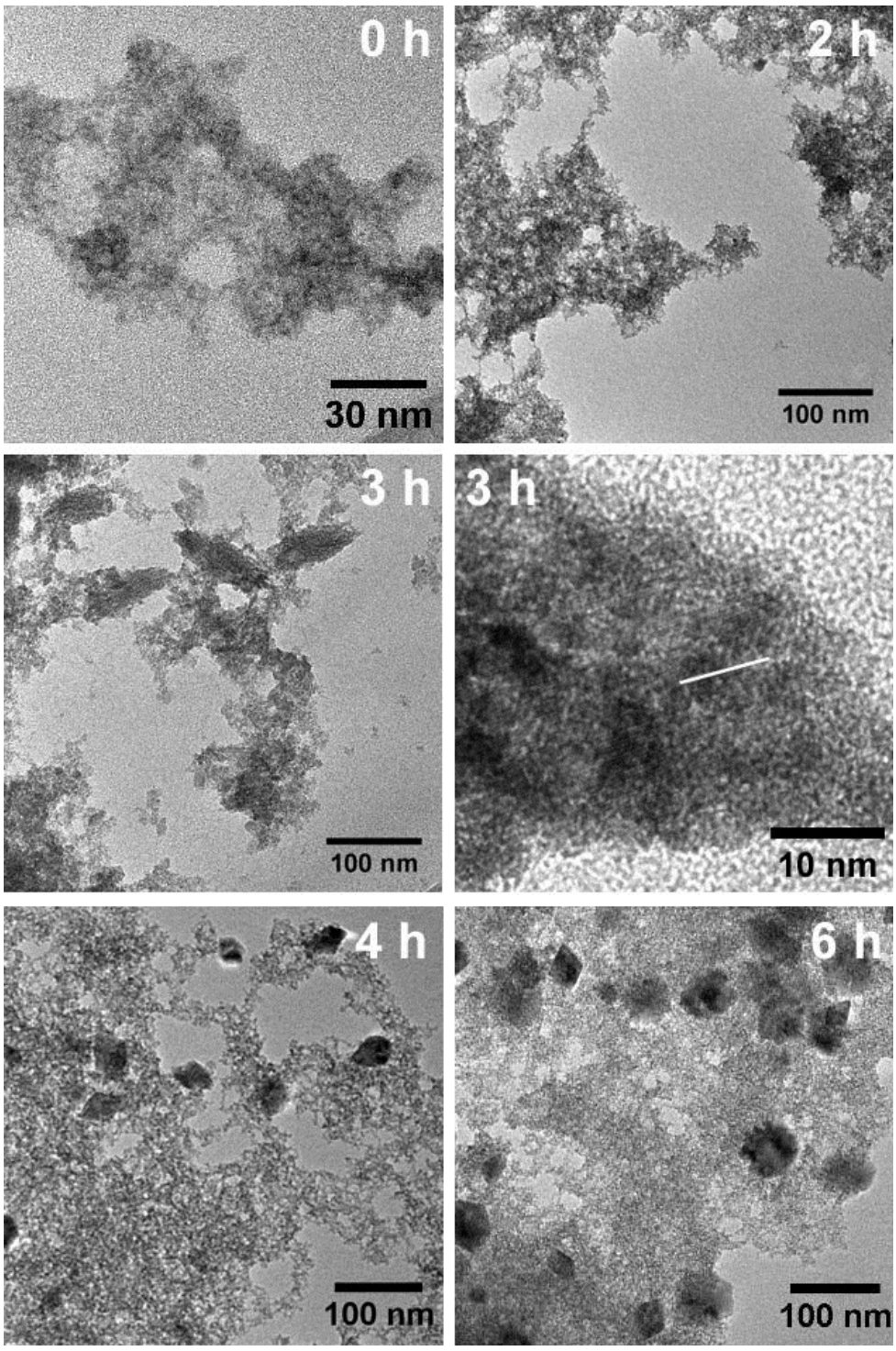

Figure 2.6. Time-resolved TEM images from the synthesis of hematite from an aqueous suspension of 2-line ferrihydrite aged at 90 °C. At 0 h and 2 h, only primary particles are visible. After 3, 4, and 6 h, a mixture primary particles and large hematite crystals can be seen. 3 h sample, right image: The earliest sample in which hematite could be identified, based on lattice fringe spacing, was 3 h. The white line parallels the hematite (012) lattice fringes.

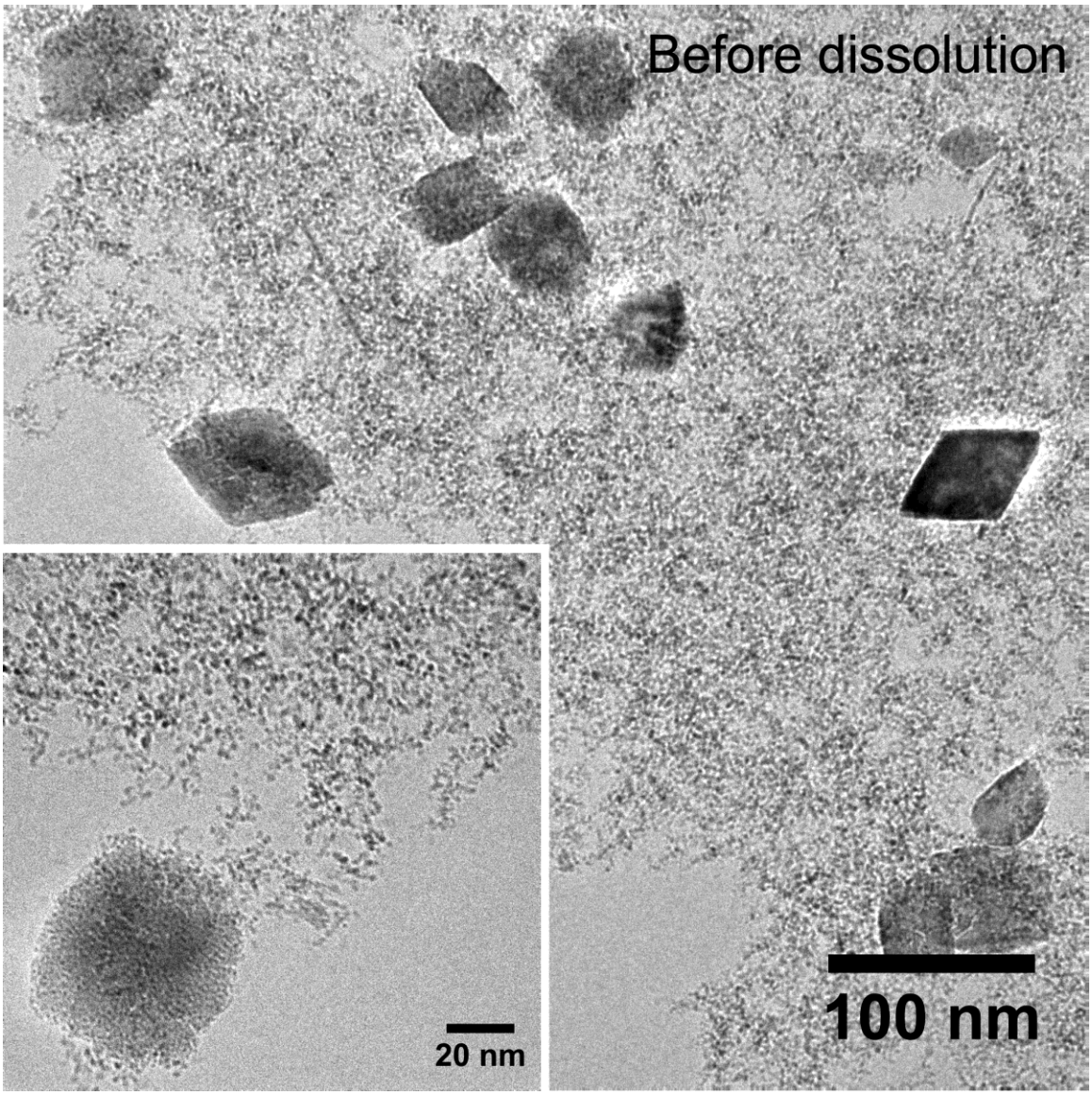

Figure 2.7. Cryo-TEM images of 2lnFh aged for 6 h at 90 °C prior to vitrification. Primary particles—likely a mix of 2lnFh and hematite—and high-contrast, 30-80 nm hematite particles are both visible in the sample vitrified after 6 h of aging. Inset: higher magnification image showing texture of a large hematite particle.

Aggregation of nanoparticles is a common drying artifact of conventional TEM specimen preparation, so an in situ technique, such as cryo-TEM, is needed to gain insight into the actual aggregation state of the particles in suspension. Figure 2.7 shows a cryo-TEM image of a specimen vitrified after 6 h of aging. The primary particles were highly aggregated, and large hematite crystals were always seen in proximity to these

fractal-like structures. The small particles have a wide range of contrast, which is mos likely the consequence of diffraction contrast. Thus, we conclude that there is a range of crystallinity in the small particles. The hematite crystals in the higher-magnification inset appears to be made up of many small subunits, consistent in size with the primary particles, and are relatively uniform in contrast, which would be expected if the particles were crystallographically aligned (perhaps through OA). A small amount of nanorods were also seen, consistent in shape with goethite,[23, 66] but goethite was not detected by any of the other characterization techniques.

Kinetics

The consumption of primary particles—2lnFh and similarly-sized hematite—in the formation of large hematite crystals was measured using preferential dissolution by an oxalate buffer. Preferential dissolution by oxalate is commonly used in soil science to determine the content of poorly-crystalline iron in a soil sample by exploiting the difference in dissolution rates between poorly-crystalline and well-crystalline iron-containing minerals (e.g., $k_{2lnFh} >> k_{hematite}$).[163, 196] Small hematite particles also dissolve more rapidly than larger ones, presumably due to their higher surface area and an increase in surface structural disorder (Figure 2.S1). The amount of dissolved Fe(III) is proportional to the amount of iron contained in primary particles and can be used to determine the rate at which primary particles are consumed to form large hematite particles.

Linear trends in a plot of inverse $Fe(III)_{aq}$ concentration vs time (Figure 2.8a) indicate that the consumption of primary particles follows a second-order rate law. This is consistent with a particle-mediated crystal growth mechanism, such as OA. Consumption of primary particles was also found to be more rapid when 2lnFh suspensions were aged

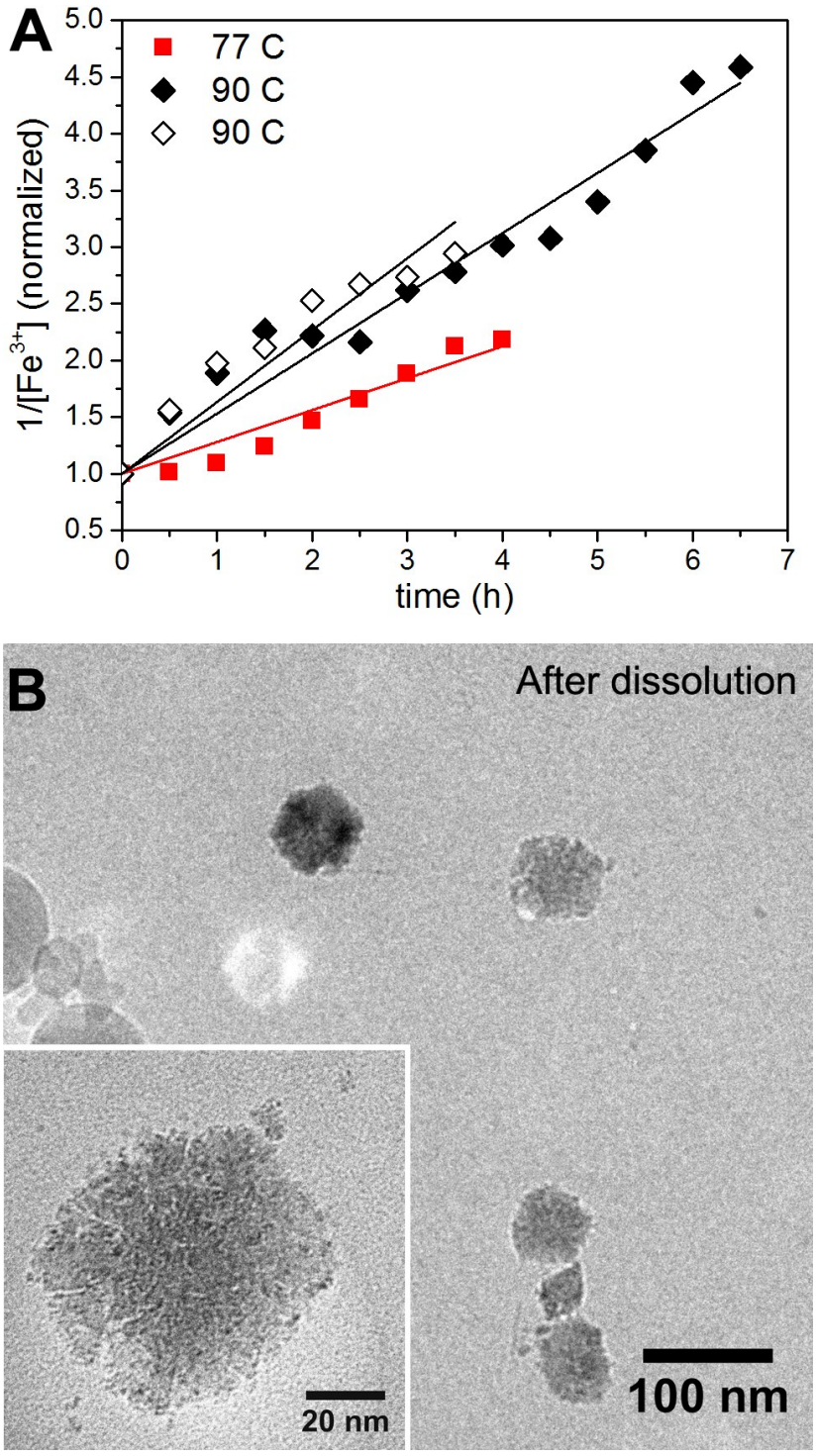

Figure 2.8. A) Inverse concentration of Fe(III) (aq) after preferential dissolution by oxalate as a function of aging time for samples aged at 77 (solid squares) and 90 (solid and open diamonds) °C. [Fe(III)] is directly proportional to the concentration of primary particles remaining at each sampling time. B) Cryo-TEM image of a sample treated with the preferential dissolution process for 7 min prior to vitrification. Many large hematite particles remain, but few primary particles are visible.

at 90 °C, rather than 77 °C, showing that the rate of this reaction is temperature-dependent. Though the mineral phase cannot be determined from oxalate dissolution alone, a pellet consistent in color with the final hematite suspensions was visible to the eye after centrifuging a sample that had been aged for 0.5 h at 90 °C and treated with the preferential dissolution process.

Cryo-TEM images of a suspension aged for 6 h at 90 °C and treated with the preferential dissolution procedure before vitrification (Figure 2.8b) show hematite crystals consistent in shape and size with the pre-dissolution sample (Figure 2.7) and the conventional TEM images. Very few small particles can be seen, leading us to the conclusion that preferential dissolution by oxalate buffer was effective at dissolving primary particles.

Implications for phase transformation and growth

The formation of small hematite particles could occur along many possible pathways. Small hematite domains were observed in the as-synthesized 2lnFh, which could provide nucleation sites for the propagation of hematite throughout an aggregate in a solid-state phase transformation. This is similar to the final steps of the proposed model of akaganeite to hematite transformation presented by Frandsen and Legg et al., in which additional akaganeite particles aggregate onto large hematite particles and then phase transform.[79] On the other hand, ferrihydrite could transform into small hematite particles, which then assemble via OA. In this case, transformation could be induced via interface nucleation (IN) if two particles made transient contact and formed an interface at which the new phase could nucleate, but did not form particle-particle bonds before disaggregating. Hematite growth could also occur by the dissolution of ferrihydrite and

precipitation of the dissolved species onto pre-existing hematite nuclei. Finally, the formation of hematite from the aggregation of ferrihydrite particles followed by solid-state phase transformation cannot be ruled out as an additional pathway concurrent with one or more of the others proposed.

Our data support several of these possible pathways. The texture of the hematite particles observed in TEM images supports a particle-mediated growth mechanism (Figures 6, 7, and S2), and only rules out DP as the dominant route of hematite formation. Peak broadening analysis (Figure 2.3) indicates that >20 nm hematite particles are present as early as 2 h of aging. The XRD data could indicate that ferrihydrite aggregated into large structures prior to transformation or that small hematite particles had already assembled into a larger structure via a process such as OA.

The observed diffraction contrast in TEM images (Figure 2.6 and Figure 2.7) suggests that small crystalline particles formed prior to aggregation into larger structures. The hematite structural intermediates seen in Figure 2.7 and Figure 2.8 (insets) are reminiscent of the structural intermediates interpreted as evidence for OA in goethite crystal growth in which phase transformation precedes aggregation.[66, 74] Magnetometry results also support the hypothesis that small hematite particles form first, followed by aggregation.

With the exception of DP, all of the proposed mechanisms are types of particle-mediated growth and would be consistent with a second order rate law,[65] as observed via preferential dissolution (Figure 2.8a). Particles may assemble before or after phase transformation. DP and coarsening also to play a role, e.g., by filling in the dimpled

surfaces of the large hematite nanoparticles, such as those seen in Figure 2.6, Figure 2.7, and 2.S2.[174, 203]

The order of phase transformation and crystal growth, and mechanisms by which these processes occur, have important environmental impacts. Iron oxides play significant roles in the sequestration of arsenic and heavy metals, and understanding the release of these elements due to dissolution or their uptake during precipitation, phase transformation, and crystal growth will aid in making more accurate predictions about the fate and transport of these elements through the environment.

Conclusion

Several possible mechanisms for phase transformation and growth of hematite from 2lnFh have been discussed. Low temperature magnetometry data demonstrate the presence of small, poorly crystalline hematite particles at very early aging times and support the hypothesis that small 2lnFh particles first phase transform, then aggregate or serve as sites for aggregation of additional ferrihydrite. Measurements of remanent magnetization detected and identified hematite at lower concentrations and higher defect levels than the X-ray diffraction techniques used here. Evidence was also seen for the rapid formation of large hematite particles, supporting the hypothesis of assembly followed by rapid transformation. Ultimately, we conclude that 2lnFh undergoes phase transformation before assembly into larger particles, but do not exclude the possibility that both of the proposed mechanisms operate simultaneously.

Acknowledgements

We thank Valeri Petkov for assistance with synchrotron X-ray diffraction experiments. Work at the Advanced Photon Source was supported by DOE under Contract DEAC02-06CH11357.

Participation of J. Soltis and R. L. Penn in this research is funded by the National Science Foundation (#0957696). Soltis also receives funding from the University of

Minnesota IPrime Nanostructural Materials and Processes Program and the Department of Chemistry Newman and Lillian Bortnick Fellowship.

Participation of B. Gilbert in this research was supported by the Director, Office of Science, Office of Basic Energy Sciences, of the U.S. Department of Energy (BES-DOE) under Contract No. DE-AC02-05CH11231

Participation of Joshua M. Feinberg and the Institute for Rock Magnetism in this research is funded by the NSF-EAR Instrumentation and Facilities #1339505.

Supplemental Information

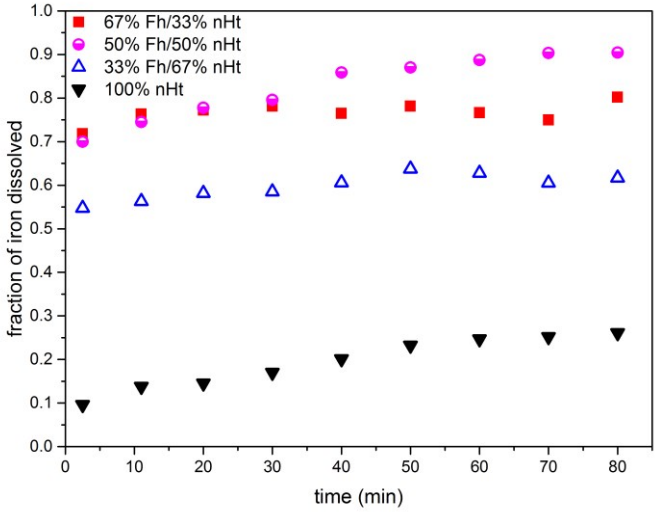

Figure 2.S1: Fraction of total iron dissolved via preferential dissolution in oxalate buffer of known mixtures of 7 nm hematite particles (nHt) and 2-line ferrihydrite (Fh). Samples were kept on ice and in the dark during the dissolution process.

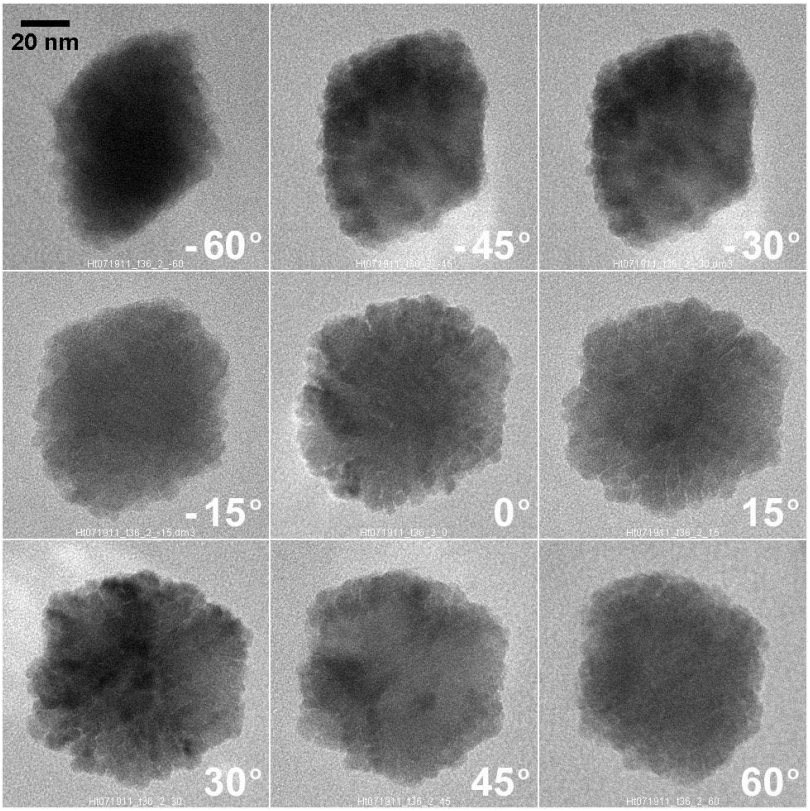

Figure 2.S2: TEM images of a hematite particle after 36 hours of aging at 90 °C. The particle is tilted an additional 15 degrees in each image in succession from -60° to 60°. Scale bar is 20 nm and is the same for all images. Note particularly the rhombohedral presentation at -60° and hexagonal presentation at 30°, a total rotation of 90°.

Chapter 3 : Heterogeneous phase transformation in iron oxides

Jennifer A. Soltis,[1] Jacqueline Harapan,[1] and R. Lee Penn[1]

[1]Department of Chemistry, University of Minnesota, Minneapolis, Minnesota 55455, United States

Introduction

Iron oxides and oxyhydroxides (collectively referred to here as iron oxides) are naturally occurring materials that play critical roles in the environment. Iron oxides are redox active, and Fe(II) can serve as a reductant towards harmful natural and anthropogenic compounds.[13, 23] Iron oxides also can adsorb and absorb toxic elements such as arsenic and heavy metals and, thus, affect their mobility in the environment. For example, arsenic can be immobilized in or on iron oxide particles, which can effectively serve to sequester it from drinking water sources.[30, 204] In contrast, when arsenate is reduced to the more soluble arsenite, the mobility of arsenic can be enhanced.[204] Finally, the iron oxides have many industrial[205-206] and medical[207-209] uses due to their low cost, high abundance, and low toxicity.[19, 23, 161]

Phase transformations in iron oxides are exquisitely sensitive to reaction conditions such as temperature,[23, 89, 183-185] pH,[86, 88, 183, 186] ionic strength,[87] and the presence of organic compounds[84, 187-188] and microorganisms,[19, 158, 210-212] which all vary widely in natural settings. Additionally, it is common to find iron oxides in the presence of other metal oxides and metal sulfides,[23] e.g. alongside pyrite (FeS_2) in acidic mine drainage environments.[19, 213] The complexity of natural settings obfuscates attempts to elucidate iron oxide growth and phase transformation in the environment.

Three common naturally occurring iron oxides phases are goethite (α-FeOOH), hematite (α-Fe_2O_3), and ferrihydrite ($Fe_5O_8H•4H_2O$).[19, 23, 161] Ferrihydrite (Fh) is a poorly-crystalline iron oxyhydroxide that is thermodynamically metastable with respect

to goethite and hematite, both of which are substantially more crystalline[23] and have a lower Gibbs free energy of transformation.[22] Fh readily transforms into these two minerals and can also produce lepidocrocite under appropriate reaction conditions.[90, 186 214]

Fh is often referred to as 2-line or 6-line ferrihydrite based on the number of peaks on its X-ray diffraction pattern (Figure 3.1), though synthetic samples in which two to eight peaks have been produced.[173] Ferrihydrite exhibiting only two peaks in its XRD pattern is generally considered less crystalline than ferrihydrite exhibiting more peaks.[170] However, the exact structure of Fh is not well understood, nor are the structural relationships between the various forms of Fh.[165-169, 173, 215-222] Some studies suggest that 2-line Fh (2lnFh) is more disordered, less stable, more reactive, and has a greater number of defects and vacancies than 6-line Fh (6lnFh),[223] and these differences may be great enough that the two forms are distinctly different structures.[170-171] Early studies of Fh structure compared it to highly disordered hematite.[164]

Three important crystal growth mechanisms that affect phase transformation in the iron oxides are coarsening (Ostwald ripening), aggregation followed by recrystallization, and oriented attachment (OA).[174] Coarsening occurs when particles grow via the net movement of atoms or ions from small particles to larger ones. Aggregation occurs when crystals attach or aggregate with no particular alignment, then form a new single crystal via recrystallization or dissolution and reprecipitation. OA, non-classical case of crystal growth, occurs when crystals achieve crystallographic orientation with respect to each other prior to attachment and the formation of larger crystals.[66, 74, 174] Solvent and other

dissolved species are removed from the spaces separating the oriented particles before attachment occurs or are otherwise incorporated as defects in the product crystal.

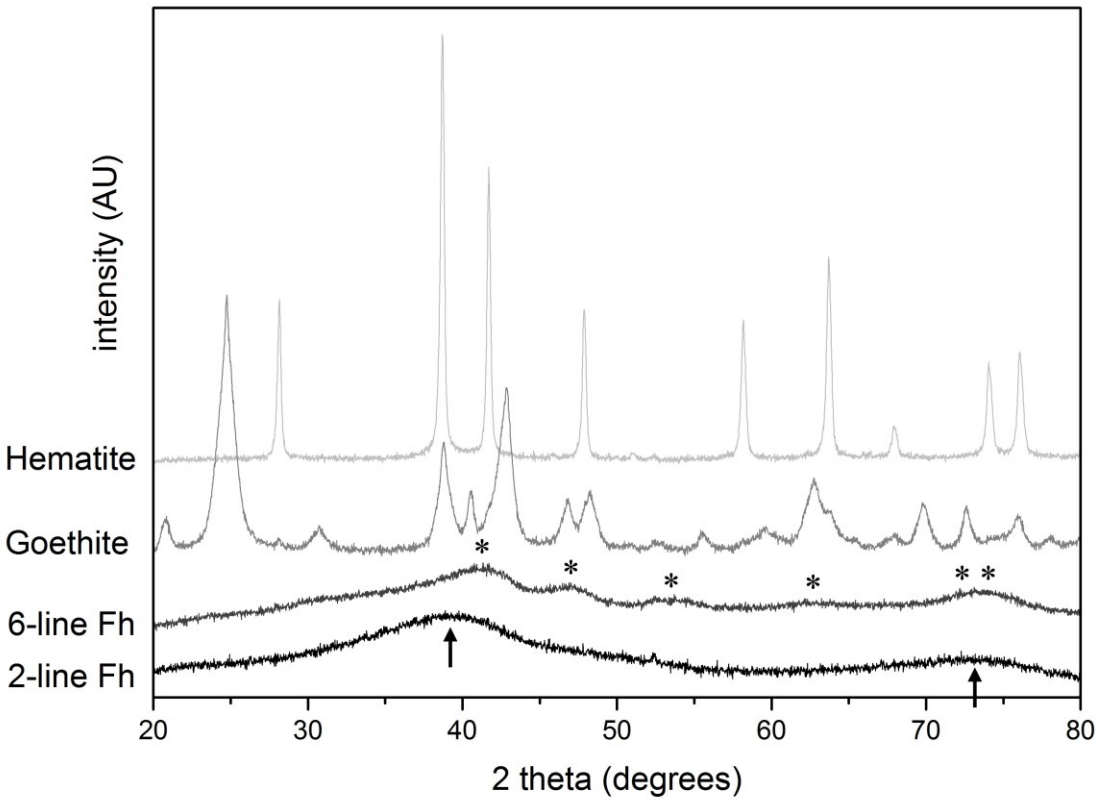

Figure 3.1: Representative XRD patterns for 2-line and 6-line ferrihydrite (Fh), goethite, and hematite collected with a Co X-ray source. The two peaks of 2-line Fh are marked with arrows; the six peaks of 6-line Fh are marked with asterisks.

Many materials exhibit size-dependent thermodynamic stability as a result of the balance between surface free energy and bulk free energy.[22, 101, 224-225] The total free energy of a nanoparticle is the sum of its surface and bulk Gibbs free energies. When surface area:volume is high, the thermodynamic stability of the nanoparticles is dominated by contributions from surface free energy, while when surface area:volume is low, the thermodynamic stability of the nanoparticles is dominated by contributions from bulk free energy. Small particles with high surface area:volume are stabilized by low surface free energies. If surface free energy is high compared to bulk free energy, particle

shapes with low surface area:volume are favored. Volume can increase, and relative surface area decrease, through particle growth by coarsening or aggregation. This decreases the surface area:volume ratio and increases the relative influence of bulk free energy on the total energy of the system. At critical particle sizes, transformation to a more thermodynamically stable phase may be favored.[22] Indeed, much research shows that the structure of an initially formed nucleus is often distinct from that of the bulk phase.[22, 189]

A classic example of size dependent phase stability can be seen in the titanium dioxide phases anatase, brookite, and rutile, each of which is thermodynamically stable in a particular size range.[101, 226-227] Anatase and brookite are the dominant phases when particles are smaller than ca. 15 nm, and rutile is the dominant phase at larger particle sizes.[227] Anatase and brookite have lower surface free energies as compared to rutile, which has the lowest bulk free energy. When anatase and brookite particles reach a critical particle size, phase transformation to rutile occurs because the bulk energy contribution outweighs that of the surface energy contribution.[100-101, 182]

Evidence for phase transformations driven by both interface nucleation (IN) and dissolution precipitation (DP) has been observed in the titanium dioxides[45, 95, 98, 100-101, 182] as well as other materials.[79, 225, 228-230] When IN dominates, the new phase nucleates at the interface between two precursor particles and propagates via recrystallization.[95] This is illustrated in Figure 3.2, where a new mineral phase (black) is formed at the interface between two particles of the initial phase (white), and the new mineral phase propagates away from the initial nucleus. IN sites may be formed at particle-particle interfaces produced by random aggregation or OA,[101] and phase transformation via IN can be an

indicator of particle-mediated growth.[17] In DP, less stable particles dissolve, and dissolved species diffuse to the more stable, already existing nanoparticles. The relative contribution to phase transformation from IN and DP depends on reaction conditions, and transformation via DP in particular is highly dependent on solubility. In the case of the formation of rutile from anatase, DP was observed to dominate growth and phase transformation under hydrothermal conditions at pH 1, where titanium dioxide is relatively more soluble, while IN was observed to dominate at pH 3, where it is sparingly soluble.[100, 182] All of these growth and phase transformation processes may occur simultaneously and to different extents, which complicates quantification of the relative contributions from each mechanism.[61, 74, 119, 174]

Past work with the iron oxides has largely focused on the transformation of initially phase-pure samples of iron oxides or (non-iron) metal-doped iron oxides.[23, 41, 48, 84-90, 183, 185, 187, 231-232] Here, we present results demonstrating that small amounts, or "spikes," of more stable iron oxides may promote targeted phase transformation and can lend further insight into the mechanism of phase transformation in iron oxides. Aging a suspension of 2lnFh spiked with goethite at elevated temperatures resulted in the formation of both hematite and goethite, while aging a pure 2lnFh suspension produced only hematite. In contrast, aging a suspension of 6lnFh resulted in the formation of hematite and goethite when spiked with hematite, but goethite alone when not spiked. A significant increase in the rate of phase transformation in hematite-spiked 6lnFh was observed, but no similar increase in rate was observed in the aging of spiked 2lnFh. Understanding the phase transformation of these materials will increase understanding of their behavior in

heterogeneous natural systems and may lead to better predictions of environmental fate and transport and increased synthetic control of nanoparticles for industrial applications.

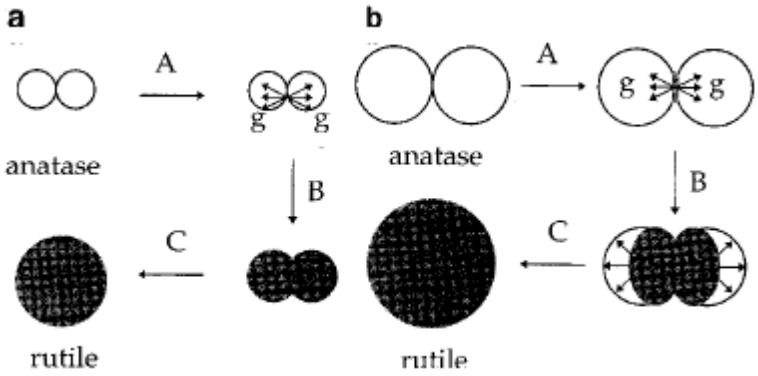

Figure 3.2: "Diagram showing steps involved in the phase transformation of nanocrystalline anatase particles over shorter reaction times (a) and over longer reaction times (b). The *g* is the nuclei growth rate." Reproduced from Zhang and Banfield, 1999.[95]

Materials/Methods

All labware was washed with nitric or oxalic acid and triple rinsed with Milli-Q water (Millipore, 18.2 MΩ·cm resistivity) prior to use. Milli-Q water was used for all synthesis and dialysis procedures.

Nanoparticle syntheses

The aqueous suspension of 6-line ferrihydrite was prepared by following the method of Penn *et al.* by adding an equal volume 0.48 M sodium bicarbonate (Fisher Scientific) to 0.4 M ferric nitrate (Sigma Aldrich) via peristaltic pump over ca. 10 min at room temperature.[85] The suspension was stirred during the addition of the base and for an additional three minutes afterward. A microwave anneal step was performed by microwaving the suspension (Samsung, 900W) until it reached a rolling boil, with shaking every 30 seconds. The microwave anneal step has been found to increase homogeneity in the final particles.[85] The suspension was cooled in an ice bath to room temperature and dialyzed at 10 °C in Spectra-Por #7 dialysis tubing (MWCO 2000)

against Milli-Q water. The water was changed every three or more hours for a total of nine changes.

The 2-line ferrihydrite aqueous suspension was prepared using a modified version of that published by Schwertmann and Cornell (2000).[41] 150 mL of 1 M potassium hydroxide was added to 200 mL of 0.2 M ferric nitrate while stirring at room temperature, followed by the addition of 0.10 g oxalic acid dihydrate (Mallinckrot Baker) and 80 mL Milli-Q water. The suspension was dialyzed following the same procedure as for 6-line ferrihydrite.

Goethite was synthesized by adding 250 mL of 2.5 M potassium hydroxide (Mallinckrodt) to 60 mL of 0.5 M ferric nitrate at a rate of 20 mL/min with stirring. The resulting suspension was aged at 60 °C for 100 h and subsequently cooled to room temperature and dialyzed as above.[233]

Hematite was synthesized after Schwertmann and Cornell (2000), Method 6.[41] 2-line ferrihydrite was synthesized, adjusted to pH 6.5, and aged at 90 °C for 36 hours, then cooled to room temperature and dialyzed as above.

Preparation and aging

All iron oxide suspensions were adjusted to pH 5 after dialysis by adding sodium hydroxide or nitric acid as necessary. Mass loading was determined by drying 1.000 mL, 2.000 mL, 5.00 mL, and 10.00 mL of each suspension and measuring the mass of the dried samples. Mass was plotted as a function of suspension volume and the data were fit with a linear regression to determine the mass loading of the suspensions in mg/mL.

Samples were prepared for aging by spiking each of the ferrihydrite precursor suspensions with goethite and/or hematite suspensions. Suspensions containing iron

oxide solids that were 100 wt% 6-line ferrihydrite (6lnFh) and 100 wt% 2-line ferrihydrite (2lnFh) were prepared. Mixed-phase samples are labeled with the mass fraction of the secondary phases, reported as wt% of iron oxides. Hereafter, this value is simply reported as the weight percent with respect to the total suspended solids.

Each mixture was placed into polyethylene centrifuge tubes in aliquots of 7 mL. The capped tubes were placed into an oven held at 90°C. Individual tubes were removed from the oven at designated times, after which they were immediately plunged into an ice bath to quench phase transformation and growth. They were poured into weigh boats to dry at room temperature. Samples that were not immediately set out to dry were stored at 10 °C for up to 3 days. Samples were sonicated to dislodge settled nanoparticles from the bottom of the centrifuge tubes prior to being poured into weigh boats.

Two control samples, one containing 3.5 wt% Ht/96.5 wt% Gt and one 10 wt% Ht/90 wt% Gt, were also prepared to test for detectable phase transformation of goethite to/from hematite under these conditions. These samples were placed into 121 mL glass reactors and sealed with crimp caps to prevent evaporation during prolonged aging. One reactor of each mixture was sacrificed every 3-4 days for three weeks. Samples were then poured into weighing boats to dry.

Characterization: X-ray diffraction

All dried samples were prepared for X-ray diffraction (XRD) by grinding using an agate mortar and pestle. Ground samples were front-packed into a zero-background quartz holder. XRD patterns were collected over the range of 20-80° 2θ using a PANalytical X'Pert Pro MPD theta-theta diffractometer equipped with a cobalt K-α source (wavelength 1.79 Å) and an X'Celerator detector. Patterns were compared with

the reference powder diffraction files (PDFs) for 6-line ferrihydrite (#29-712), goethite (#29-713), and hematite (#33-664). Representative experimental diffraction patterns are shown in Figure 3.1.

To date, there is no structural model of ferrihydrite that adequately describes all of the features seen in its XRD pattern,[166, 168-169, 215-217, 222] which precludes analysis of the XRD patterns via Rietveld refinement. Instead, calibration curves were constructed from XRD patterns of known ratios of goethite and hematite each mixed with 2lnFh and 6lnFh,[183] and patterns are shown in Figure 3.S1. The areas of the goethite (101) and hematite (012) peaks were measured using X'Pert Highscore Plus. Peak area was plotted as a function of wt% goethite or hematite and fit with a linear regression.

Line broadening analysis was performed by applying the Scherrer equation to the full width half maximum determined from peak fits of the goethite (101) peak.[194] Origin 2015 was used to fit two GaussAmp curves to each peak.

Transmission electron microscopy

Each specimen for conventional transmission electron microscopy (TEM) was prepared by sonicating a small amount of dried, ground iron oxide sample in MilliQ water for 30 minutes, then casting a single drop onto a 200 mesh copper TEM grid coated with a layer of holey carbon (SPI Supplies, Inc). Grids were allowed to dry under ambient conditions.

Cryo-TEM specimens were prepared using 200 mesh copper TEM grids coated with lacey carbon (SPI Supplies, Inc). Grids were charged for 60 seconds using a Pelco Glow Discharger. A 3-μL drop of each aqueous iron oxide suspension was placed onto the carbon side of a charged grid and loaded into an FEI Vitrobot automated plunge freezer

(Mark IV). The grid was then blotted with filter paper for 2 seconds (-2 mm offset) and plunged into liquid ethane after a 1-second relaxation period. All subsequent handling, including transfer to a storage box, took place under liquid nitrogen to maintain cryogenic conditions.

Specimens were imaged using an FEI Tecnai G^2 F30 field-emission gun transmission electron microscope equipped with a cryo stage and operated at 300 kV. Cryo-TEM images were collected using a cryo holder held at -178 °C and using low-dose conditions. Images were captured with a Gatan UltraScan charge-capture device camera operated via Digital Micrograph v3.

Images were processed with ImageJ v1.48q (a public domain image processing and analysis program from the National Institutes of Health[199]) and altered only by cropping, rotating, and/or applying linear adjustments to brightness and contrast. Photoshop CS2 was used for montage layouts.

Discussion/Results

XRD patterns (Figure 3.3) show that the amount of secondary mineral phases (goethite and/or hematite) increased with aging. Aging aqueous suspensions containing only 2lnFh resulted in the formation of hematite, which is consistent with previously reported results.[41] Spiking the same suspension with 2.3 wt% goethite prior to aging resulted in increasing both hematite and goethite with time. In the case of 6lnFh, only goethite formed, unless hematite was added before aging. In past work, aging suspensions of 6lnFh at pH 5 and 90 °C was shown to favor goethite formation,[88] while aging suspensions of 2lnFh at pH 6.5 and 90 °C was shown to favor hematite formation.[41]

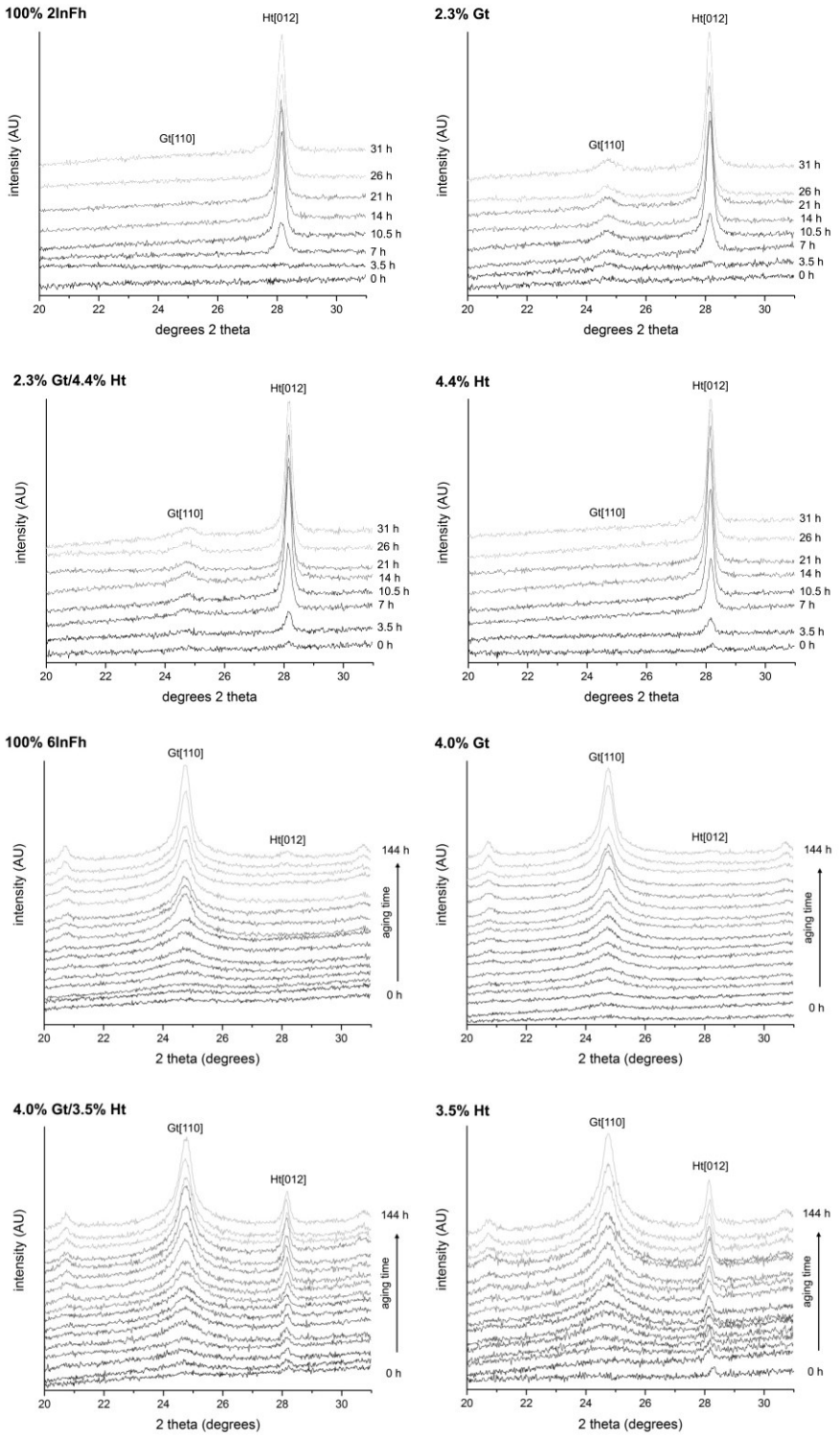

Figure 3.3: XRD patterns (collected with a Co X-ray source) show an increase in hematite and goethite content with aging time. Patterns are vertically offset for clarity. Top: 2lnFh mixed with indicated amounts of goethite (Gt) and/or hematite (Ht). Bottom: 6lnFh mixed with indicated amounts of Gt and/or Ht.

The results of spiking suspensions of 2lnFh and 6lnFh were quite different, as evidenced by the amount of each secondary phase produced (Figure 3.4). In suspensions of 2lnFh spiked with goethite, only a small increase in goethite was observed. In contrast, in suspensions of 6lnFh spiked with hematite, a comparatively large increase in hematite was observed. This suggests that 6lnFh is sensitive to the presence of the more thermodynamically stable hematite, which is not the phase readily formed upon aging in the absence of hematite. There was not a significant difference in the rate of 2lnFh transformation in the spiked samples, perhaps because of the material's overall greater instability and transformation rate. Aging goethite spiked with 3.5 wt% and 10 wt% hematite under similar conditions resulted in no detectable change in the amount of hematite over three weeks of aging, indicating that phase transformation from goethite to hematite (or vice versa) did not contribute significantly to differences in the composition of the final samples.

XRD line broadening analysis indicates that the average crystal domain length of goethite increased with time in the 6lnFh samples (Figure 3.5).[194] Goethite particles in the 6lnFh samples exhibited a bimodal size distribution along [101], consistent with an increase in the crystal domain length of the large rods used in the initial spike and the formation and further growth of new, smaller rods. The calculated length along [101] for the goethite particles used for spiking, determined with the same method, was found to be 10.6 (the width of the rod). High-resolution TEM images indicated that the large rods had multiple crystal domains prior to aging (Figure 3.S2), so this increase in crystal domain length may indicate recrystallization, further growth of the nanoparticles, or both. Fitting of the goethite [101] peaks in XRD patterns of the 2lnFh samples did not show two

distinct populations, although TEM images indicated that small goethite rods had formed.Goethite produced from 6lnFh was larger than goethite produced from 2lnFh, which is consistent with the dependence of goethite rod size on initial ferrihydrite size observed in past work.[48]

XRD line broadening analysis of the goethite [101] peak demonstrates that the goethite present in aged 6lnFh samples has a bimodal particle size distribution, with ca. 8 nm and 32 nm average domain sizes after 144 h determined using the Scherrer equation. The [101] domain length of the goethite used for spiking was 10.6 nm, in close agreement with the value calculated from TEM measurements of 10.5 nm. The [101] domain length is calculated from TEM measurements by multiplying the measured width of a rod by the crystallographic constant 0.593. [ref Stemig or other] Close examination of TEM and cryo TEM images reveals the presence of ca. 55-75×10 nm (5.9 nm along [101]) particles and 500×50 nm (29.7 nm along [101]) particles, in agreement with the values determined via line broadening analysis. Interestingly, the 500×50 nm particles are similar in size and shape to the initial goethite spiked into the sample (Fig 3.S2). Thus, one can conclude that the goethite used for spiking (or the goethite present at time zero) increased in width and that new goethite crystals formed and grew.

A bimodal size distribution was also observed in TEM images in goethite rods formed from aged 2lnFh, but was not detectable via XRD. The goethite [101] peaks were of low intensity in the XRD patterns of aged 2lnFh, and the peaks were unable to be fit with a bimodal distribution. Measurements from TEM images indicate average rod sizes in populations of ca. 150×50 nm and 400×100 nm.

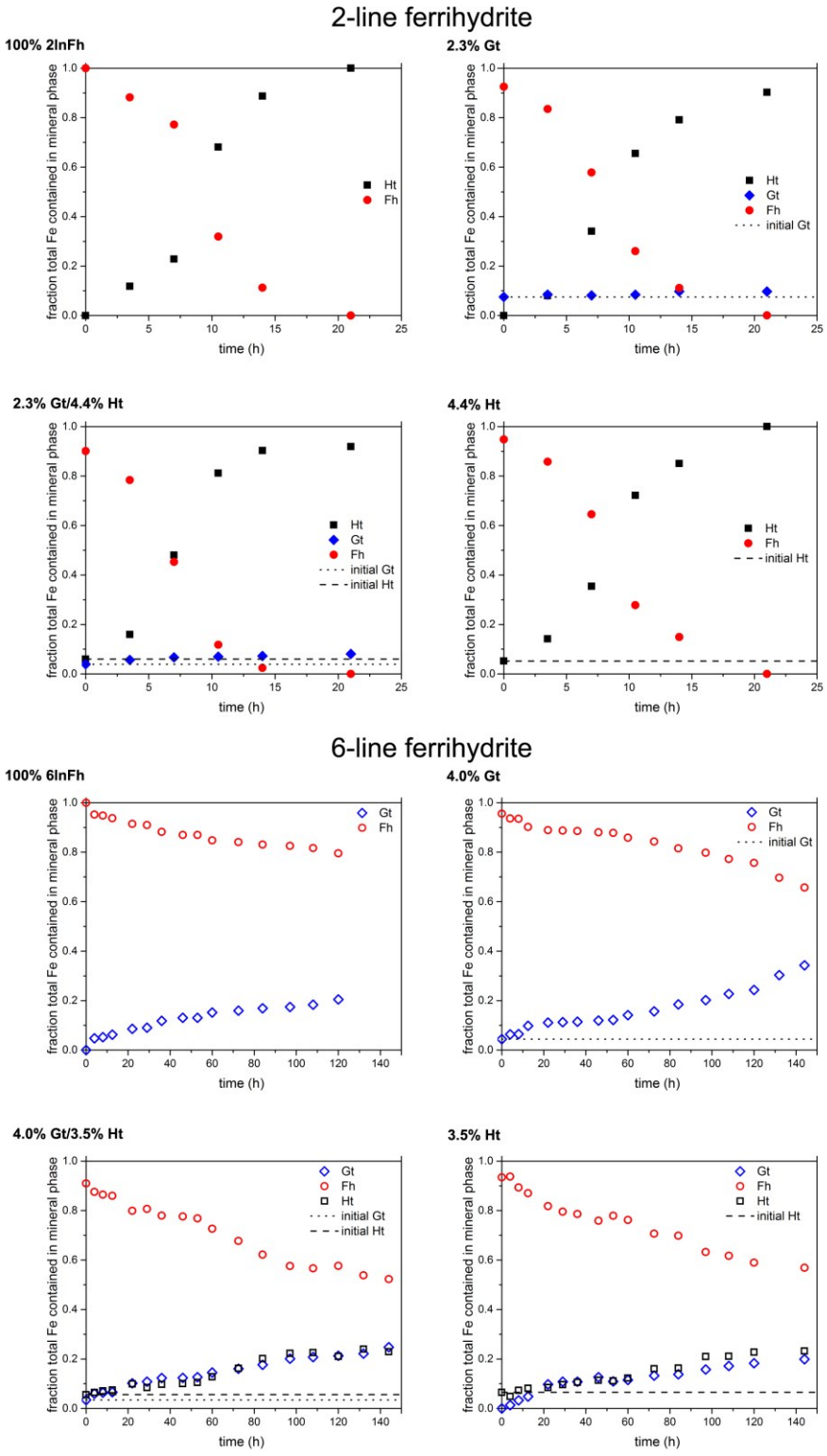

Figure 3.4: Weight fraction of secondary mineral phases produced from 2lnFh (top) and 6lnFh (bottom) as a function of time. Individual plots are labeled with the mineral phases used to spike the initial samples.

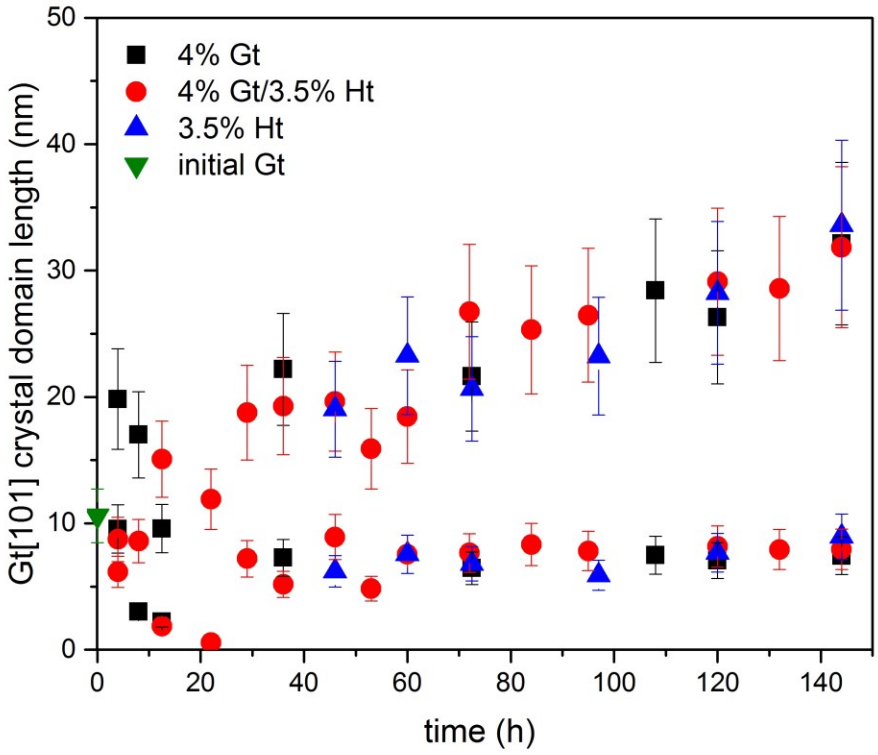

Figure 3.5: Crystal domain lengths of Gt synthesized from 6lnFh obtained by application of the Scherrer equation to XRD data and plotted as a function of time. A bimodal Gt size distribution was observed.

Cryo-TEM images (Figure 3.6) showed that aggregation played a role in phase transformation and growth. Particles consistent in shape and size with the Fh precursors were grouped in multimers consisting of as few as three particles or in extensive fractal-like assemblies of tens to hundreds of nanoparticles. These disordered assemblies may be composed of one or more of the three phases (goethite, hematite, and the applicable Fh). No conclusion can be drawn without additional information, but the range in particle contrast in the images suggests that at least some of the particles have transformed to goethite or hematite, which both have greater diffraction contrast in TEM than either type of Fh. Aggregates of primary particles were larger in 2lnFh samples than in 6lnFh.

Structural intermediates indicative of particle-mediated growth, formerly referred to as mesocrystals, were also seen.[17, 67, 74] Figure 3.7 shows cyro-TEM images both goethite

and hematite structural intermediates in 2lnFh aged with goethite and hematite (same sample as Figure 3.6c). The large structures appear to be composed of many small particles similar in size and shape to the Fh precursor particles. The hexagonal structural intermediate is consistent in morphology with the hematite produced as the end-product of this synthesis (Figure 3.S3) and the electron diffraction pattern (Figure 3.7b inset) showed that the structure is hematite. A goethite structural intermediate has formed alongside a raft of goethite particles used for spiking. The structural intermediates have gaps between the primary particles, and there is no direct mineral-mineral contact between the particles, similar to the OA structural intermediate observed in goethite by Yuwono et al.[66]

The formation of a structural intermediate along the side of a goethite raft is consistent with the observation via XRD that the width of the large rods increased with time (Figure 3.5). The goethite rods added as the spiking material averaged 18 nm wide before aging, while newly-produced goethite rods were <10 nm wide. We hypothesize that the particles that first transformed into goethite, then assembled into the structural intermediate, due to the relatively even contrast in that area of the structure both at low and high magnification. However, it cannot be ruled out that Fh particles were attracted to the thermodynamically stable large particles and then transformed to goethite via IN.

The rate of phase transformation depended on which Fh precursor and mineral spikes were used. Modeling yielded insights, despite no single model standing out as a best fit. Models for zeroth order growth, first order growth (equivalent to a dissolution precipitation model in which primary particle size does not change with time),[182, 226] and phase transformation at contracting spherical interfaces,[234-235] shown in Figure 3.8, all

had linear fits with similar adjusted R^2 values. An examination of the residuals also gave no strong indication that one model fit better than another. In all of these models, the absolute value of the slope is proportional to the phase transformation rate constant.

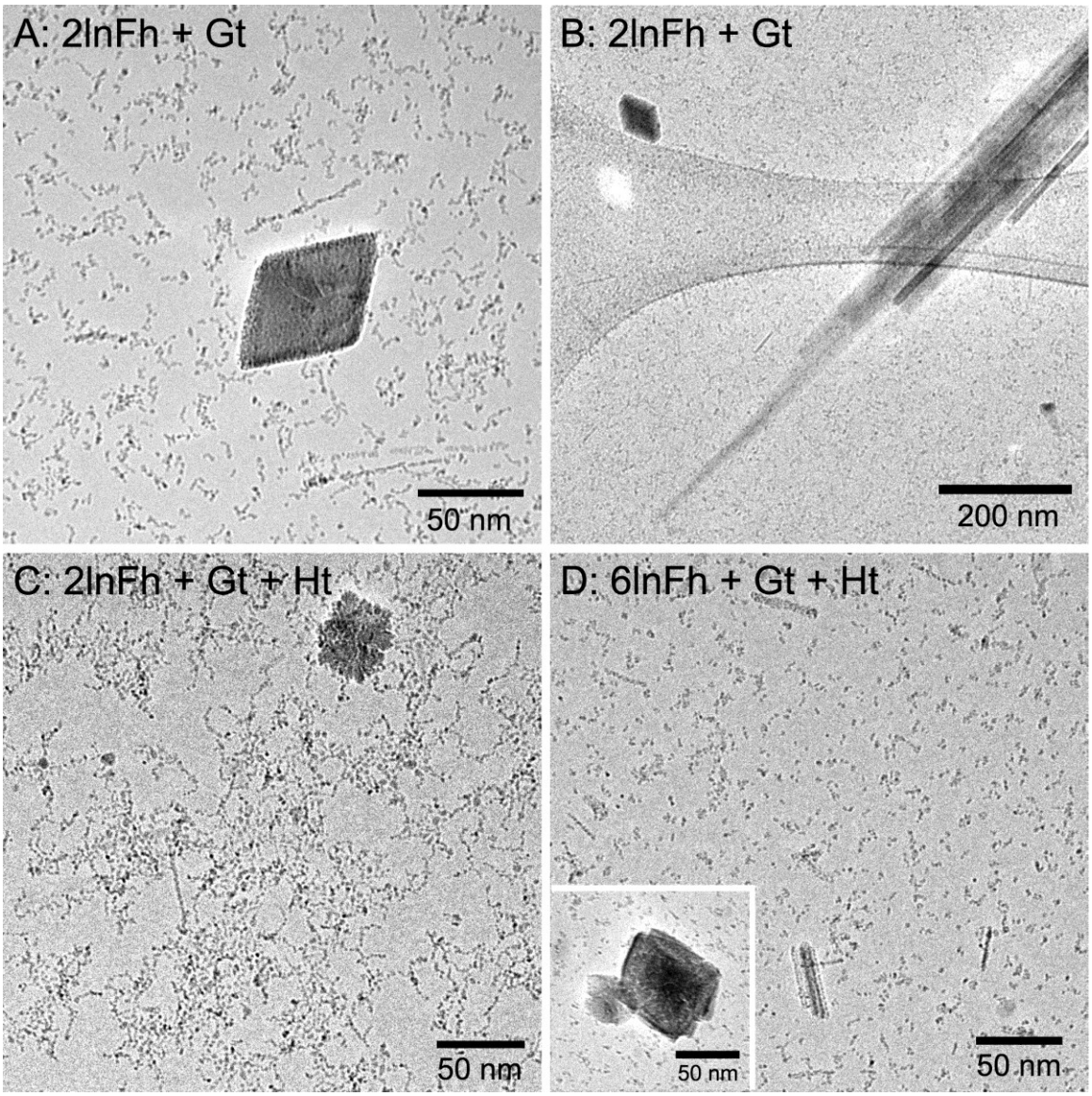

Figure 3.6: Cryo-TEM images of 2lnFh aged at pH 5 and 90 °C for 7 h in the presence of goethite (a and b) or goethite and hematite (c) and 6lnFh aged under similar conditions for 8 h in the presence of goethite and hematite (d).

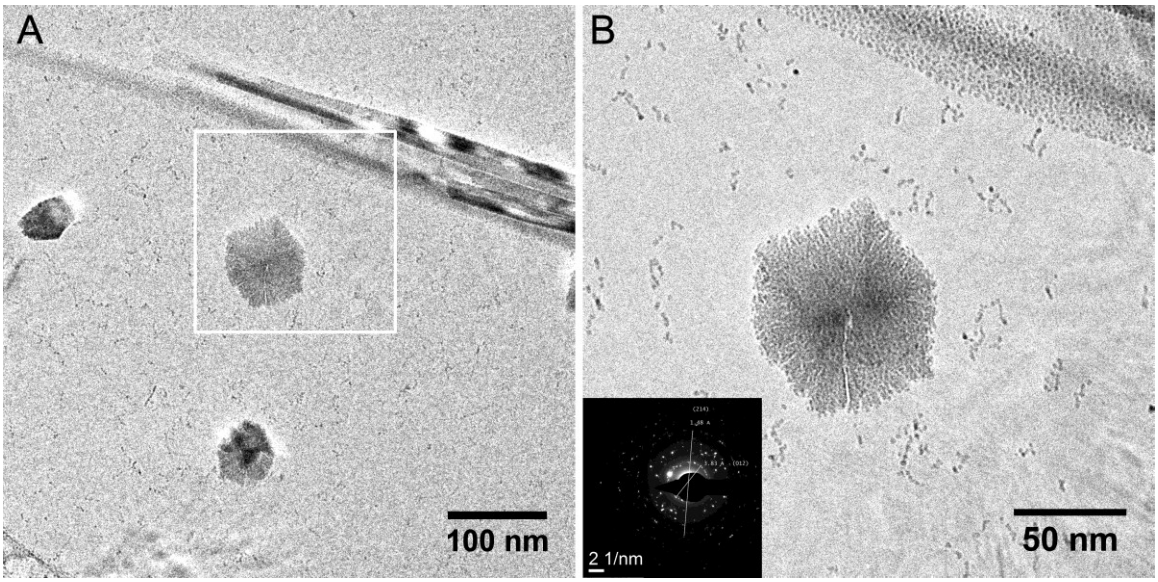

Figure 3.7: Cryo-TEM images of 2lnFh aged with goethite and hematite and vitrified after 7 h. (b) is a higher magnification image of the area outlined in (a). The electron diffraction pattern of the hexagonal structure in (b) is shown in the inset.

Some models worked for either 2lnFh or 6lnFh precursors, but not both, and are shown in Figure 3.S4. In some of these cases, the R^2 values seemed appropriately high, but analysis of the residuals showed that the fits had systematic trends in the difference between measured data and predicted value from the model. As expected from past modeling of goethite growth kinetics from 6lnFh,[49, 85-87] a second-order rate law fit the growth data well, but this did not hold true for the 2lnFh samples. Models for transformation via interface nucleation, nucleation and growth of overlapping nuclei, nucleation along a single dimension, solid-state phase transformation as proposed by Johnson, Mehl, Avrami, and Kolmogorov, and first-order growth likewise described data from one Fh precursor but not the other. These models are reviewed by Zhang and Banfield in the context of titanium dioxide transformation.[95] The differences in kinetic trends, and the fact that some models worked well for only one type of Fh, support the conclusion that there are major structural and/or thermodynamic differences in these two materials.

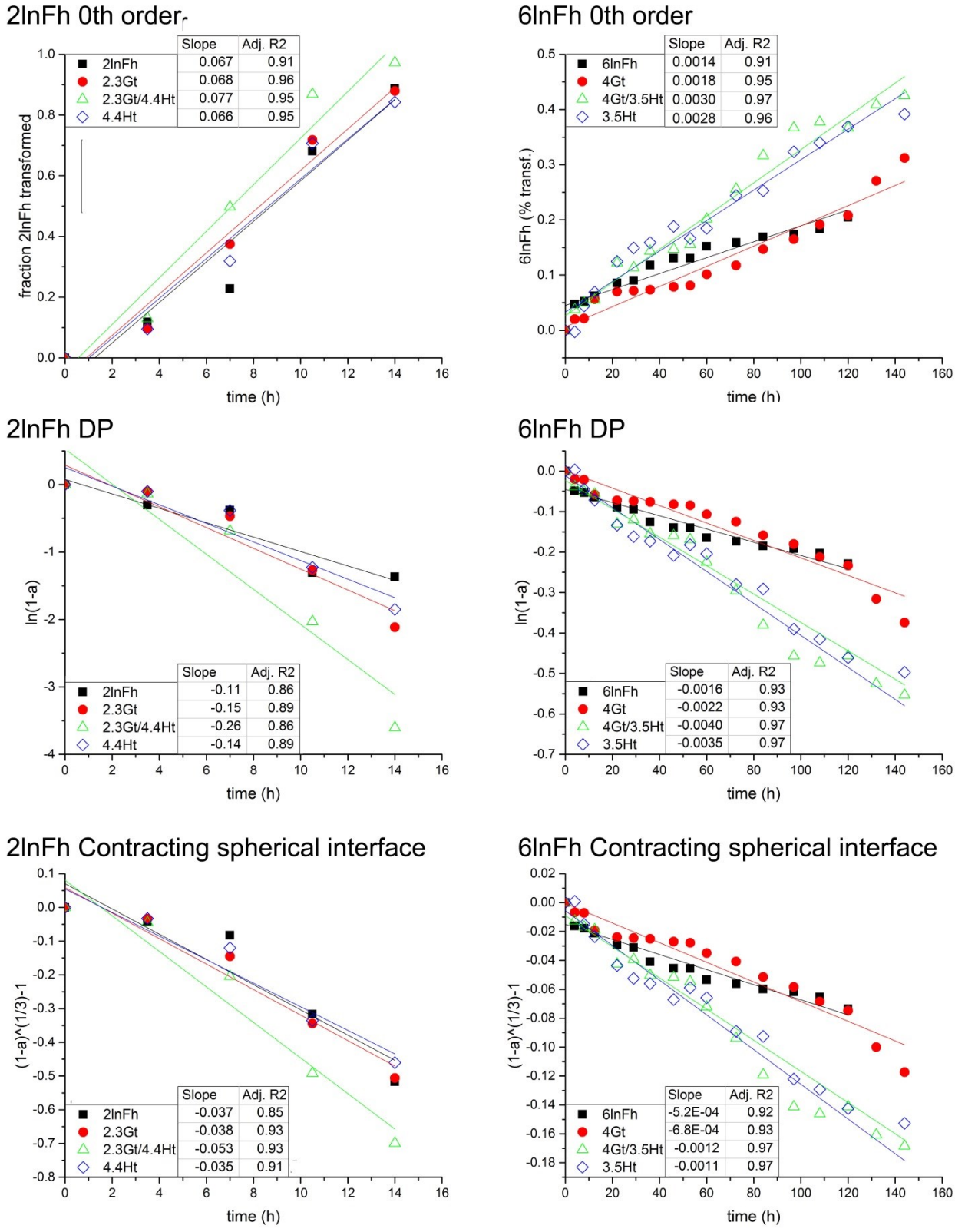

Figure 3.8: Plots of kinetic models that described phase transformation in both 2lnFh and 6lnFh samples well.

In the case of 6lnFh, a direct comparison of the starting amount of well-crystalline material is not sufficient to explain kinetic trends. The presence of hematite played a key role in increasing the rate of 6lnFh transformation and hematite formation, but the rate of goethite formation was not affected by mineral spiking. OA has been previously observed as the dominant growth mechanism for goethite under similar aging conditions,[66, 85] and the rate of OA decreases with particle size,[49] so the presence of the large goethite rods due to spiking would have minimal effect on the rate of growth of new, small rods via OA. The texture of the smaller goethite is also consistent with growth via OA, as seen in cryo TEM images (e.g., Figure 3.6d). The large difference in particle size and thermodynamic stability between 6lnFh and hematite[22, 189] makes growth of hematite via DP likely as the dominant mechanism in hematite formation. This may also be due to more structural similarity between Fh and hematite than Fh and goethite,[166, 222] making it relatively easy to produce hematite in addition to goethite.

On the other hand, the kinetics of 2lnFh phase transformation was fastest when both hematite and goethite were added, which was the sample with the greatest initial amount of well-crystalline material. We hypothesize that this is due to the greater amount of thermodynamically stable material yielding a greater free energy difference that favors growth by coarsening or phase transformation by DP. Cryo-TEM images also revealed structural intermediates consistent with growth via OA (Figure 3.6a-c and Figure 3.7).

Conclusion

The addition of goethite and hematite to 6lnFh prior to aging had a significant effect on phase transformation rates and products. Adding one of the well-crystalline minerals resulted in phase transformation to that mineral, in addition to the phase that was formed

in the un-spiked sample of the corresponding Fh. The rate of phase transformation in 2lnFh was sensitive only to the quantity of well-crystalline spiking material and not the identity of the mineral added. Phase transformation in 6lnFh was more dramatically affected by the mineral spikes, with the addition of hematite causing more rapid transformation and resulting in approximately equal amounts both the major and minor product phases. The difference in kinetics and primary mineral phase produced upon aging under identical kinetics support the conclusion that the two types of Fh have significant structural and/or thermodynamic differences. Cryo-TEM imaging showed that particle-mediated growth played an important role in the phase transformation and growth of goethite and hematite particles. The lack of a single kinetic model to describe all of the samples indicates that a comprehensive picture of phase transformation in iron oxides has yet to be fully realized.

Acknowledgements

JH was funded by the University of Minnesota (U of MN) Undergraduate Research Opportunities Program. JAS and RLP were funded by the U of MN Department of Chemistry and Nanostructural Materials and Processes Program and the National Science Foundation (NSF-0957696 and 1012193). Parts of this work were carried out in the Characterization Facility, U of MN, a member of the NSF-funded Materials Research Facilities Network (www.mrfn.org) via the MRSEC program.

Supplemental Information

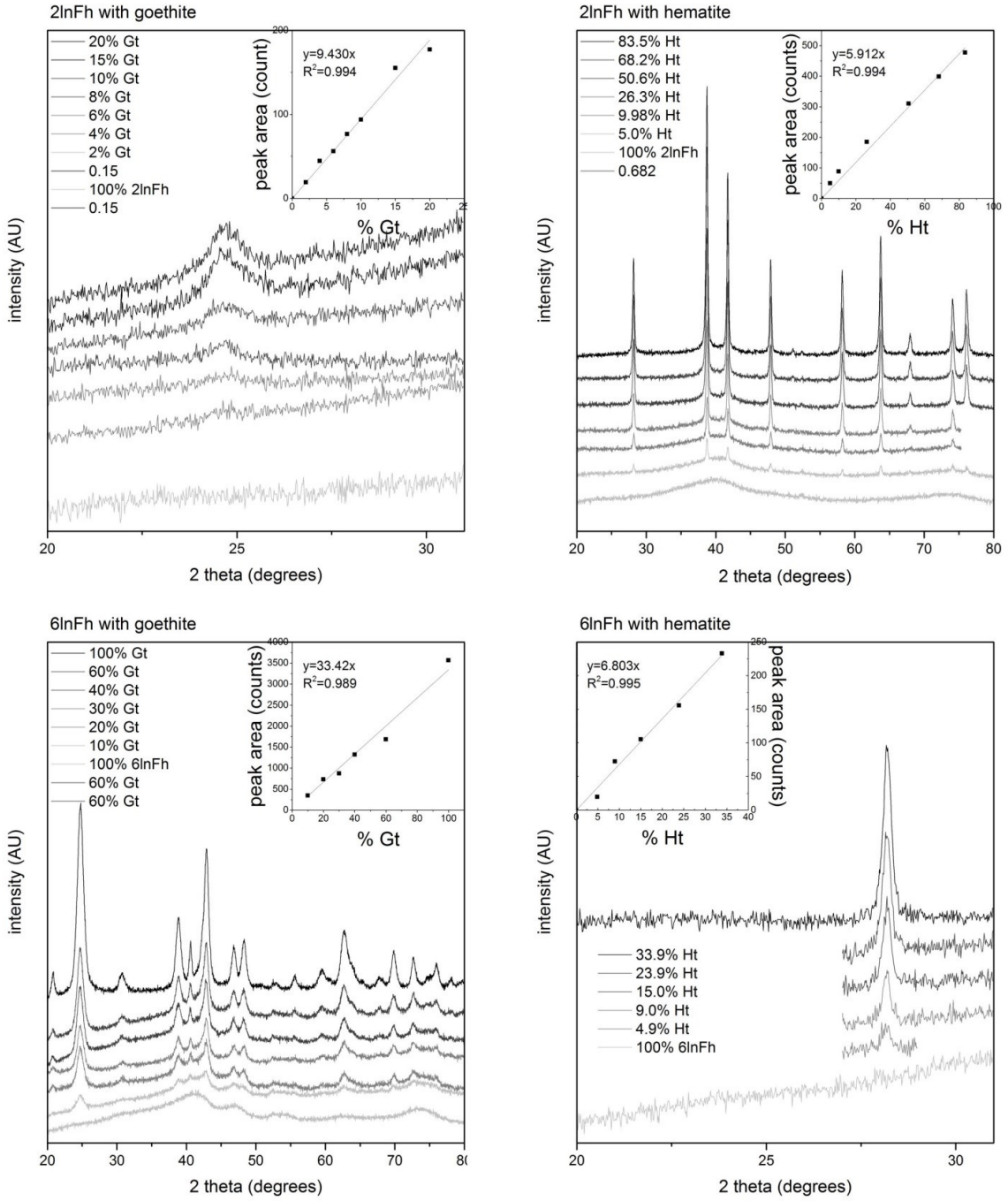

Figure 3.S1: XRD patterns of 2lnFh and 6lnFh mixed with known masses of goethite or hematite. Calibration curves of peak area for the Gt (101) and Ht (104) peaks vs. mass percent goethite or hematite are given in the insets. Patterns were collected using a Co radiation source.

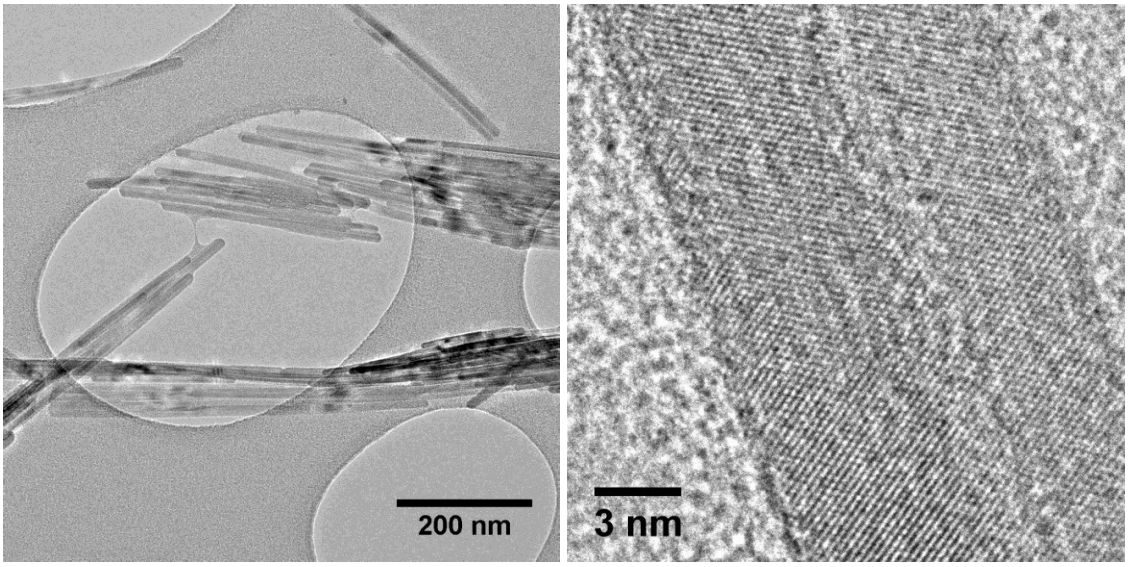

Figure 3.S2: Left: Conventional TEM image of goethite rods used for spiking Fh samples. The rods have a variation in diffraction contrast due to multiple crystal domains. Right: High resolution TEM image of a goethite rod with lattice fringes indicating multiple crystal domains.

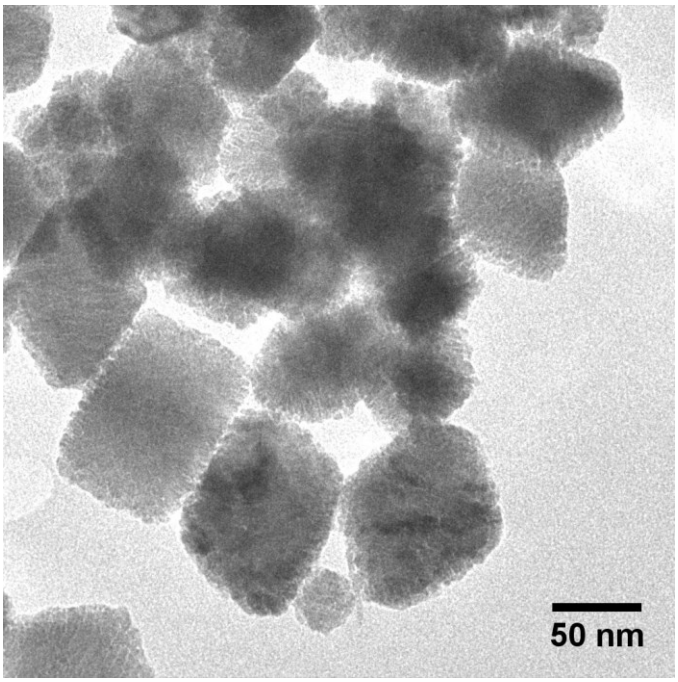

Figure 3.S3: TEM image of hematite nanoparticles produced by aging 2lnFh for 14 h at pH 5 and 90 °C.

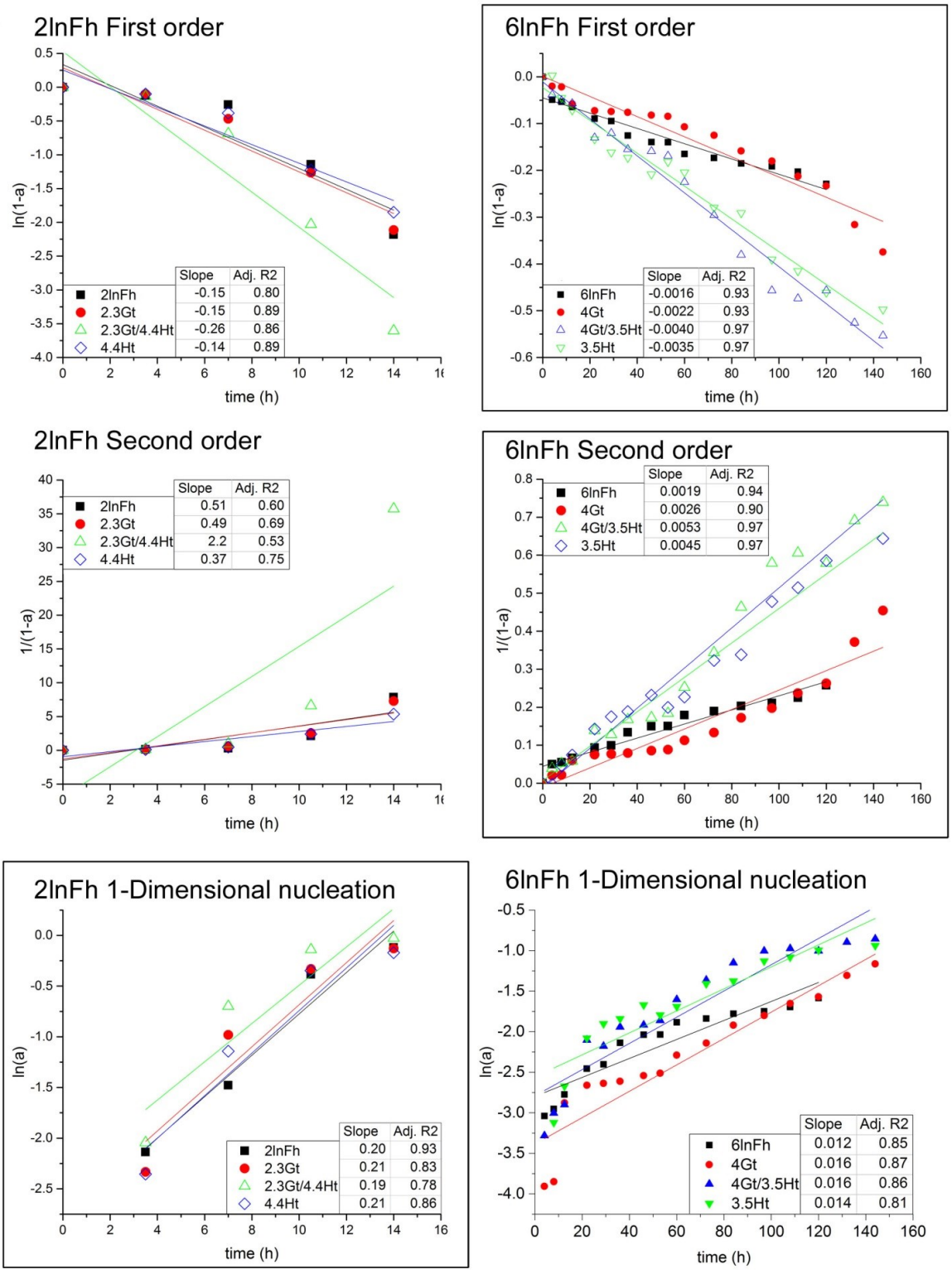

Figure 3.S4: Plots of kinetic models of phase transformation and growth that fit one or neither of the suites of samples. Plots for models that described the transformation well are outlined in black.

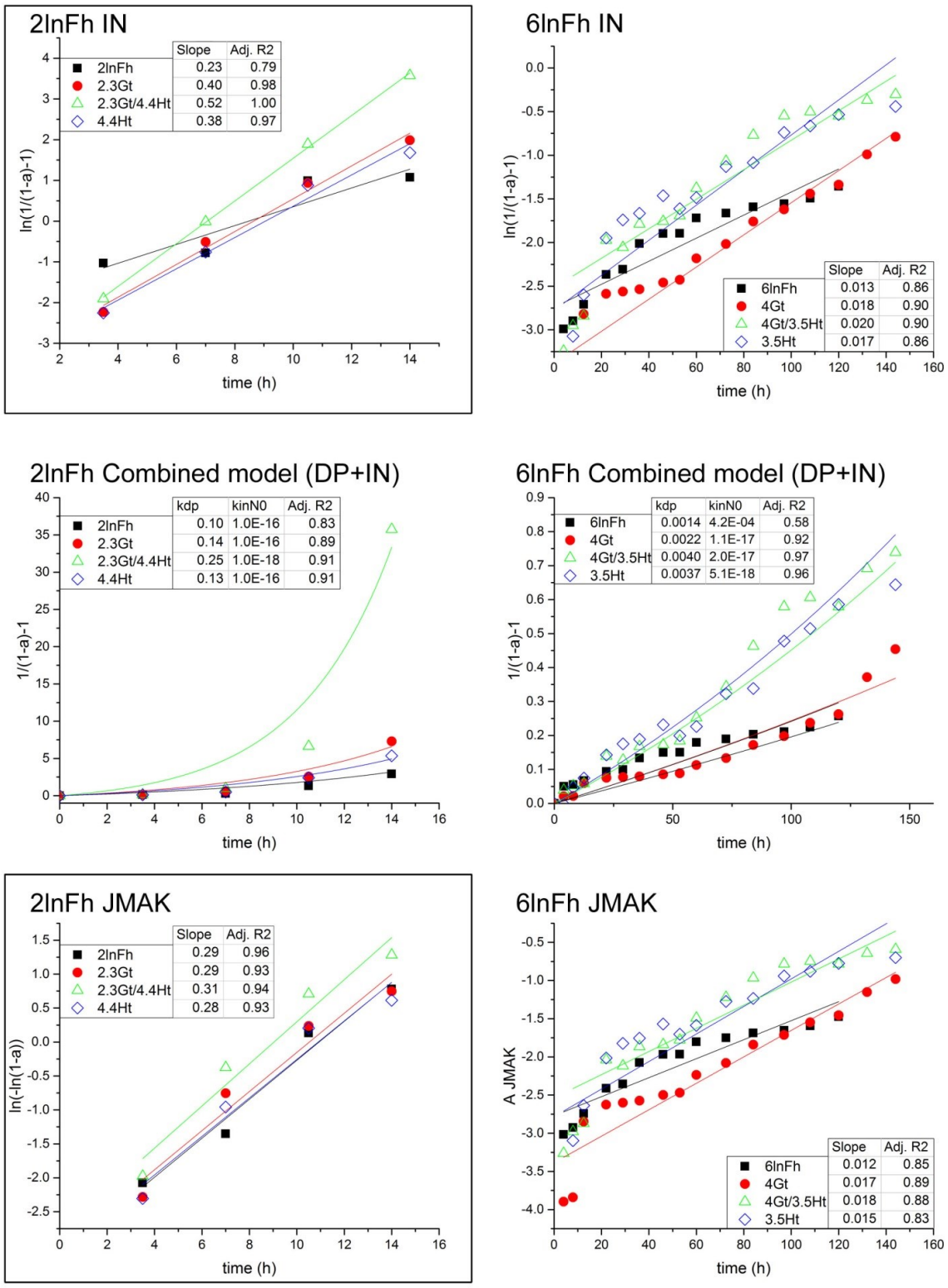

Figure 3.S4, con't: Plots of kinetic models of phase transformation and growth that fit one or neither of the suites of samples. Plots for models that described the transformation well are outlined in black.

Chapter 4 : Electron Mobility and Trapping in Ferrihydrite Nanoparticles

*Jennifer A. Soltis,[1] Adam M. Schwartzberg,[2] R. Lee Penn [1] and Benjamin Gilbert[3]**

[1]Department of Chemistry, University of Minnesota, Minneapolis, Minnesota 55455, United States
[2]Molecular Foundry, Lawrence Berkeley National Lab, 1 Cyclotron Road, Berkeley, California 94720
[3]Earth Sciences Division, Lawrence Berkeley National Laboratory, Berkeley, California 94720, United States

Introduction

Iron oxide, hydroxide and oxyhydroxide nanoparticles (hereafter referred to as iron oxides) are naturally occurring worldwide in a number of different settings, including soils, groundwater, and marine environments.[23, 161, 236-237] They play an important role in biogeochemical cycling of many elements due, in part, to their redox reactivity. For example, arsenic and heavy metals are commonly adsorbed to or incorporated into ferrihydrite, a poorly crystalline iron oxyhydroxide.[23, 161, 220, 237-243] This effectively sequesters such contaminants, removing them from the water supply. However, iron oxides readily undergo reductive dissolution under appropriate conditions, altering the bioavailability of iron and associated species and releasing sequestered contaminants into the water supply. The rate of reductive dissolution can change based on particle size, reactive surface area,[244] and inclusion of other metals.[30, 245-246] Redox reactions facilitated by iron oxides also contribute to carbon cycling through the reduction and oxidation of organic compounds.[247-250]

The factors controlling the environmental reactivity of iron oxide nanoparticles have been examined by several groups. For example, the activation energy and the rate-determining step in reductive dissolution of ferrihydrite were found not to change as a function of particle size,[29] As-doping,[30] or differences in structure or composition.[30]

However, rate and activation energy were found to be dependent on the presence of surface-bound As[30, 251-252] and the level of Al substitution in Al-doped particles.[245-246, 251] Both the interpretation of these observations and the establishment of a basis for predicting iron oxide reactivity in the environment require knowledge of the molecular mechanism for the process.

A widely accepted mechanism for the reductive dissolution of iron(III) oxide involves sorption of the electron donor; interfacial electron transfer; and release of first the oxidized donor and then the reduced iron(II) atom. However, there is now abundant evidence that electrons transferred to iron(III) oxides can be mobile within the crystal lattice. Rapid exchange of iron isotopes clearly implicate internal electron transfer in ferrihydrite and goethite nanoparticles.[160, 253-254] Yanina and Rosso demonstrated that solid-phase electron transfer could couple redox reactions occurring on two different faces of hematite.[255] Simulation and experiment confirm that electrons transferred to iron oxide nanoparticles are localized at an iron(II) site with a distorted coordination shell (termed a *small polaron*) but can hop to the next nearest neighbor on a sub-nanosecond timescale.[256] To date, the implications of internal electron mobility upon the rates of reductive dissolution reactions have not been established.

In previous work, Katz *et al*. measured the timescales for interfacial electron transfer, recombination and electron hopping in iron oxide nanoparticles that were sensitized by a fluorescein dye.[256] That work showed that while a portion of the electrons transferred from the dye molecule recombined with the dye within ~3 ns, a significant fraction resided within the nanoparticles for longer (*i.e.*, microsecond) timescales. Electron trapping over microsecond and longer timescales has also been observed in dye-

sensitized semiconductor nanoparticles such as TiO_2[257]. Simulations of charge transfer in hematite have also played an important role in understanding recombination kinetics.[258-259] In these materials, the slow recombination kinetics were attributed to electron trapping at surface or interior defect sites, although the nature of such sites was not determined.

We hypothesized that electron localization by small polaron formation provides a mechanism that could lead to long timescale trapping of electrons in iron oxide nanoparticles. We developed a kinetic Monte Carlo simulation approach to test whether such a process mode could reproduce the two-timescale recombination kinetics. The models and simulations led to the generation of testable predictions. First, if electrons were dynamically trapped within the nanoparticles there would be a dependence on particle size. The Penn group has developed a synthesis method that is proven to generate 6-line ferrihydrite nanoparticles with mean diameters that can be tuned by synthesis conditions.[85] These materials have been used in many prior studies of ferrihydrite structure and reactivity.[29-30, 66, 85-87, 200-201, 216, 245, 260] Second, the incorporation of a realistic treatment of electrostatic interactions indicated that the electron trajectories could be influenced by surface charge. Because iron oxide surfaces protonate dynamically as a function of pH, the electron trajectories should be pH dependent.

We then used optical transient absorption to quantify the lifetimes of electrons transferred to iron oxide nanoparticles as a function of particle size, solution pH and aggregation state. In this approach, a laser is used to excite dye molecule bound to the nanoparticle surface, causing injection of the electron into the nanoparticle from the excited state of the dye. Each of these electronic states of the dye, excited and oxidized, has a distinct visible light spectrum. In TA spectroscopy, the optical spectra are recorded

at a wide range of times after the laser "pump" has excited the dye, and the changes in spectral profile over time are used to monitor the electronic state of the dye.[256, 261] In this work, we used the strength of the TA signature of the oxidized dye to monitor electron recombination rates from the sub-picosecond timescale up to 400 μs.

Materials and methods

ACS grade chemicals were purchased from Sigma-Aldrich or Fisher. Two sensitizer dyes, 2',7'-dichlorofluorescein (27DCF) and 5(6)-carboxy-2',7'-dichlorofluorescein (CDCF) were purchased from Sigma-Aldrich. All solutions and suspensions were prepared with ultrapure water (18 MΩ). All experiments were carried out at ambient temperature, on suspensions under aerated conditions or purged with $N_{2(g)}$ or $He_{2(g)}$.

Nanoparticle synthesis

Ferrihydrite nanoparticles were synthesized following the procedure of Burleson and Penn, 2006. 0.48 M sodium bicarbonate was added via peristaltic pump to an equal volume of 0.40 M ferric nitrate, with stirring, for a total addition period of 8-10 minutes. Particles were synthesized at 1, 40, and 80 °C using ice or hot water baths as needed, and all solutions were allowed to come to equilibrium temperature before synthesis began. After the addition of base was complete, the nanoparticle suspensions were stirred for three additional minutes. The 40 and 80 °C suspensions were then rapidly brought to room temperature in an ice bath. A microwave anneal step was performed as detailed in Burleson and Penn, 2006. The suspensions were again brought to room temperature in an ice bath and placed in dialysis tubing (Spectra-Por #7 dialysis tubing, MWCO = 2000 g/mol). The nanoparticles were dialyzed against ultrapure water for a total of nine water changes over several days. The minimum time interval between water changes was three

hours, and all samples were stored at 10 °C during dialysis to slow transformation to other mineral phases.

Nanoparticle characterization

Mass loading. Mass loading of nanoparticles was determined by drying 1.000, 2.000, 5.00, and 10.00 mL of each suspension and massing the dried samples. The mass of the dry nanoparticles was plotted as a function of suspension volume and fit with a linear trendline with a forced y-intercept of zero. Mass loading in mg/mL was taken from the slope of this line.

X-ray diffraction (XRD). Dried nanoparticles were ground with an agate mortar and pestle in preparation for XRD characterization. Samples were front-packed into a zero-background quartz holder. XRD patterns were collected using a PANalytical X'Pert Pro MPD theta-theta diffractometer with a cobalt K-α source and an X'Celerator detector over the range of 20-80° 2θ and compared to the International Centre for Diffraction Data reference powder diffraction file for 6-line ferrihydrite (#29-712).

Particle sizing. One drop of diluted FHyd suspension was placed onto a 200 mesh Cu holey carbon grid (Structure Probe, Inc.) and allowed to dry. Nanoparticle lengths were measured from calibrated transmission electron microscopy (TEM) images collected on an FEI Tecnai T12 with a LaB_6 source operating at 120 kV using a Gatan charge-coupled device (CCD) camera. Images were processed with Gatan Digital Micrograph v3.8.2. ImageJ was used to measure the lengths of 200 to 275 nanoparticles for each synthesis temperature. ImageJ is a public domain image processing and analysis program written by Wayne S. Rasband at the National Institutes of Health (USA).[199] An aspect ratio of 1.3

was assumed for all FHyd particles based on measurements of both length and width taken in previous work.[48]

Cryogenic TEM

Cryogenic (cryo) TEM specimens were prepared on a Vitrobot (FEI Mark IV). 200 mesh Cu lacy carbon grids (Structure Probe, Inc.) were charged in a Pelco glow discharger for sixty seconds. Three microliters of suspension were placed onto an individual grid and blotted with filter paper for 1 second. The grid was then plunged into liquid ethane (-183 °C) and transferred to a storage box under liquid nitrogen (-178 °C). All subsequent handling of the prepared grids occurred under liquid nitrogen to maintain cryogenic conditions. Samples were imaged on a FEI Tecnai G^2 Spirit BioTWIN TEM with a LaB_6 source, equipped with a cryo stage and Eagle 2k CCD camera and operated at 120 keV.

Ultraviolet-visible spectroscopy

Ultraviolet-visible (UV-vis) spectroscopy was performed on an Ocean Optics USB4000 spectrometer. Data were collected using SpectraSuite (Ocean Optics). Ferrihydrite nanoparticle concentrations for all UV-vis and transient absorption spectroscopy were chosen to maintain an optical density (OD) of 0.7 absorption units at 430 nm in 2 mm path length quartz cuvettes for un-sensitized (dye-free) particles and ranged from 0.700 to 0.944 mg/mL, depending on particle size.

Dye sensitization

The ferrihydrite nanoparticles were sensitized by quickly adding a 1-mL suspension of nanoparticles at a concentration of 0.700 to 0.944 mg/mL (depending on particle size) and pH 4 to a 1.7-mL vial containing a small volume (5 – 100 μL) of a 2.5-mM stock solution of sensitizer dye at pH 9. This method generated a suspension of sensitized

nanoparticles with a final pH between 3.75 – 4.1, depending on the amount of dye added. In order to achieve a different final pH, a small amount of either 4M NaOH (1 – 5 μL) or 2M HCl (1 – 4 μL) was added either to the dye or nanoparticle suspensions prior to mixing. Representative UV-vis absorption spectra for 4 nm Fhyd nanoparticles sensitized by 27DCF and CDCF are given in Figure 4.1.

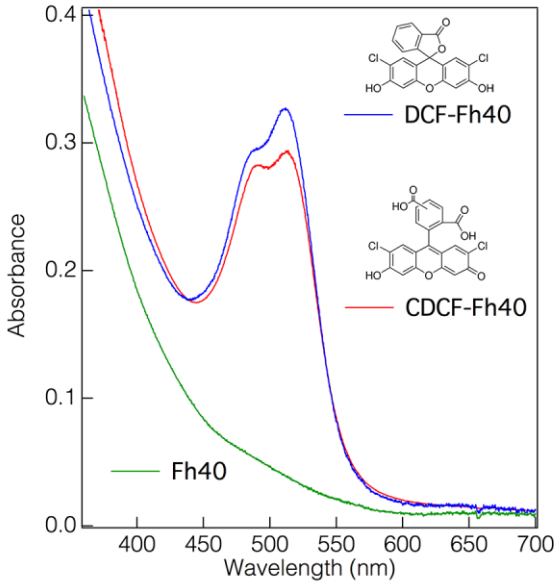

Figure 4.1: UV-vis absorption spectra of 2′,7′-dichlorofluorescein (27DCF; blue) and 5(6)-carboxy-2′,7′-dichlorofluorescein (CDCF; red) bound to 4 nm Fhyd nanoparticles and measured at pH 4. The UV-vis spectrum of uncoated Fh40 is also shown (green).

Optical transient absorption spectroscopy

Optical transient absorption (TA) experiments were carried out on a HELIOS femtosecond transient absorption spectrometer and on an EOS sub-nanosecond transient absorption spectrometer from Ultrafast systems installed at the Molecular Foundry, Lawrence Berkeley National Laboratory, Berkeley, USA. The laser source for both instruments was a Coherent Libra amplified femtosecond laser system operating at 1 kHz with 45 fs pulse duration. The laser output was split, one arm passing through a Coherent OPerA optical parametric amplifier (OPA) to produce tunable pump pulses, the other arm delivered to the transient absorption system where a white-light probe pulse was

generated in a sapphire plate or by a fiber white light source (Leukos-STM) for the HELIOS and EOS spectrometers, respectively. The pump pulse used in our measurements was tuned at 520 nm. The intensity of the pump beam was measured to be 7.5 μJ except when otherwise stated. Time delay was provided by a mechanical delay stage for the HELIOS setup and by instrument electronics on the EOS setup. Spectra were collected in the UV-Vis range between 300 and 900 nm.

All samples were kept in their original aqueous suspension. The samples were measured in 2-mm pathlength quartz cuvettes and stirred with a magnetic stir bar or recirculated in a flow-through cuvette. The anaerobic samples were not exposed to air until transfer to the cuvettes, but were measured and stored as aerobic samples during and after spectroscopic experiments.

The spectra were collected from -10 ps to 8 ns on the HELIOS system and from 1 ns to 50 or 400 μs on the EOS system. Custom user routines developed in the IgorPro software (WaveMetrics Inc., Lake Oswego, OR, USA) were used to process the data, including correction of the time dependent frequency modulation of the laser (chirp) on the signal to within ~150 fs and to extract transient kinetic data at 418 nm and 447 nm from 2D plots of spectra versus time.

The nano-to-microsecond TA kinetics were fit by a sum of exponential and/or powerlaw functions using routines written in IgorPro.

Results

Electron injection and recombination in ferrihydrite

Figure 4.2 compares optical TA spectroscopy and kinetics from dissolved (unbound) 27DCF and 27DCF-sensitized ferrihydrite nanoparticles, and demonstrates that TA experiments can follow the photoexcitation, interfacial electron transfer and

recombination processes. At ~0.2 ps after photoexcitation, both bound and free 27DCF exhibit a new excited-state absorption with a maximum at ~418 nm. The lifetime of this feature is on the nanosecond timescale for free 27DCF but is lost within 0.5 ps for 27DCF-sensitized FHyd due to electron injection. A distinct absorption feature peaked at 447 nm is evident from this time point, which is attributed to the oxidized dye that remains bound following electron transfer. As shown in Figure 4.2b and c, the 447-nm signal is lost as electrons return to the oxidized dye molecules, but a fraction of this signal remains beyond 7 ns.

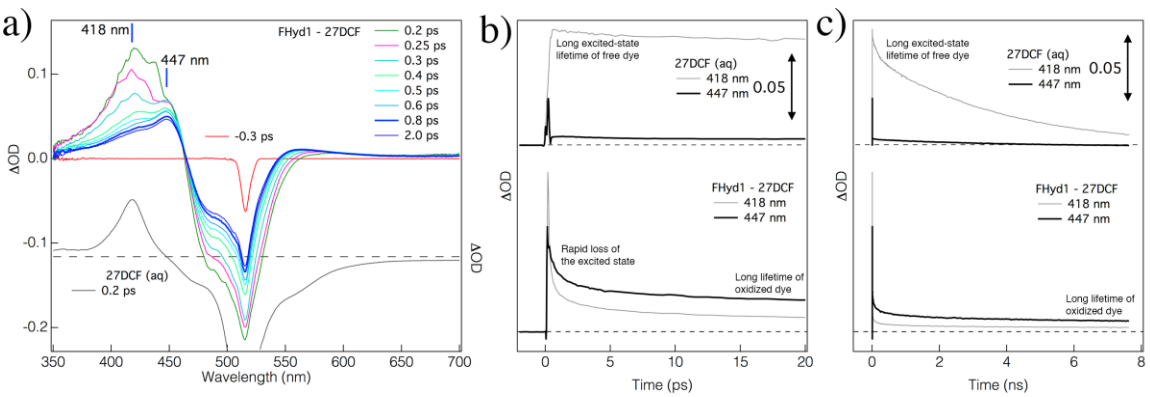

Figure 4.2: Optical transient absorption (TA) analysis of electron injection into ferrihydrite from surface adsorbed 2′,7′-dichlorofluorescein (27DCF). a) TA spectra taken before (-0.3 ps) and after 520-nm laser excitation of 27DCF bound to FHyd1, compared with the TA spectrum of aqueous 27DCF 0.2 ps after excitation. The TA spectra are displayed as the mathematical subtraction of the ground-state spectrum from the time-dependent spectrum. b) Comparison of the TA kinetics at 417 and 447 nm for dissolved (top) and bound (bottom) dye on the picosecond timescale. c) Comparison of the TA kinetics on the nanosecond timescale.

The negative-going contribution from 450 – 550 nm represents the loss in the ground-state absorption of the bound dye (called the bleach). Free electrons in iron oxide nanoparticles do not exhibit a detectable UV-vis signature, and thus here we use the strength of the oxidized dye absorption as a measure of the number of electrons residing within the nanoparticles. We found no detectable differences in the electron injection and recombination kinetics for the two fluorescein derivatives used in this work. Prior work

indicated that the vast majority of photoinjected electrons returned to the donor dye, and only *ca*. 1/300 were lost via Fe^{2+} release into solution.

Lattice Monte Carlo simulations of electron propagation and recombination

We implemented a lattice Monte Carlo (MC) model to investigate plausible mechanisms that caused long timescale trapping of electrons transferred to a nanoparticle. An iron oxide nanoparticle was represented in the MC model as a 3.4-nm sphere containing a cubic lattice of iron sites. The lattice was populated with electrons according to one of two different random initial distributions: at any site or at near-surface sites. Electron self-diffusion was treated as a thermally-activated electron exchange reaction between one occupied and one neighboring unoccupied iron site. Simulations were run either with no surface charge or with a positive surface charge appropriate for the experimental conditions ($pH < pH_{pzc}$). A Metropolis acceptance rule determined the probability of exchange between sites for which the electron affinity was calculated using one of three models for the interior electrostatic potential.[262] Loss of electrons occurred with a fixed probability at randomly distributed surface sites: these "exit channels" were closed following electron loss, representing recombination with a surface-bound dye. The results of 100 MC simulations were averaged.[263]

Our MC simulations qualitatively reproduced the experimentally observed kinetics data, supporting our model of electron injection, interior hopping, and recombination. All MC simulations predicted two distinct rates of electron loss that differed by up to two orders of magnitude (with respect to MC timesteps). Two physical aspects of the MC simulations especially affected the rates of electron loss from the nanoparticles. First, as expected, at early times a single exponential decay of the iron(II) signal was obtained only when electrons were placed at surface sites, indicating that the electrons donated by

the dye molecules do not travel far into the particle during injection and thermalization. Second, the longest retention times (and better agreement with data) were obtained for MC simulations that incorporated a positive surface charge and that recalculated at every time step the internal electrostatic potential based on the instantaneous electron distribution. Inspection of the trajectories of electrons in such simulations revealed a striking aspect: while recreating fast Fe-to-Fe electron hopping, the electrons accumulated near the surface. Thus, the simulations predicted that the trajectories of electrons can be biased by the presence of positively charged surface species,[264] which is expected for many such phases under typical environmental conditions. This phenomenon of near-surface electron accumulation could significantly extend the retention time without invoking the presence of localized structural defect sites at which electrons are trapped for long time scales.

Optical transient absorption studies of electron mobility and recombination

Changes in the optical spectra over time reveal the general mechanism of excitation and electron transfer. Figure 4.2a shows the evolution of UV-vis spectra of 27DCF bound to ferrihydrite over 0.3 ps before excitation through 2.0 ps after. The shape of each spectrum results from the combination of the population of dye molecules in the excited, oxidized, and ground states. Before excitation, the change in optical density (ΔOD) was zero at all wavelengths except the valley in the region of 520 nm, corresponding to the bleach caused by the pump laser. Shortly after excitation, the bound excited-state dye has a maximum at 418 nm (green line, indicated in figure), which is close in peak position to the spectrum of the excited-state, unbound dye (Figure 4.2a, lower half). The amplitude of this peak decreases with time since laser excitation, indicating that the number of molecules in the excited state has decreased. Electrons that have left the excited state may

return to the ground state (ΔOD = 0) or be injected into the nanoparticle, causing the dye to become oxidized. After 2.0 ps, all dye molecules are either in their "normal" or oxidized ground state, and the peak position has shifted to 447 nm. Monitoring ΔOD at this position over time can then give information about the rate at which electrons return from the nanoparticle to the oxidized dye. A rapid decrease in ΔOD indicates a rapid rate of electron transport from the particle back to the dye. A trace of ΔOD at 447 nm can then be plotted as a function of time to better extract information about the kinetics of electron transfer (Figure 4.3). The recombination kinetics spans many orders of magnitude, both in time and change in optical density.

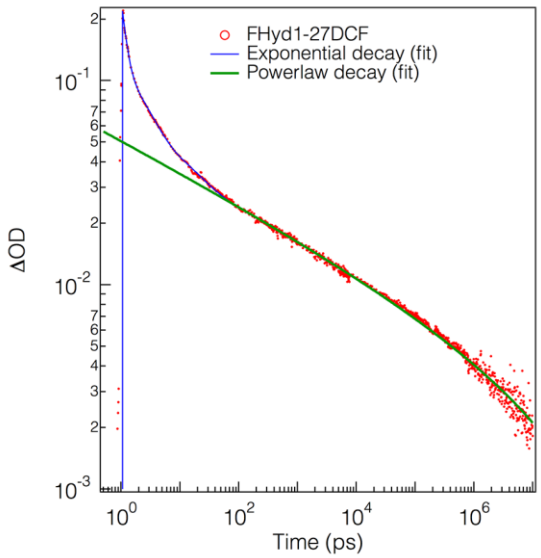

Figure 4.3: Optical transient absorption signal at 447 nm for 27DCF-sensitized FHyd1 nanoparticles. The plot displays data from equivalent samples acquired on two instruments with different time resolutions. The time axis was shifted to place time zero at 1 ps and enable plotting on a logarithmic axis.

Both long-scale and short-scale recombination rates were observed. On the ns-scale, the unbound, excited-state dye has a long, high-magnitude decay at 418 nm, and very low ΔOD at 447 nm (Figure 4.2c, top). This is consistent with the long excited-state lifetime typical of fluorophores. The FHyd-bound dye (Figure 4.2c, bottom) has a rapid loss of

excited-state dye molecules (blue line), but electron recombination with the electron-deficient bound dye molecules (red line) occurs less rapidly. Neither signal returns to zero ΔOD over a period of at least 7 ns, indicating that excited-state relaxation and electron-dye recombination are not complete. When comparing FHyd-dye and dye-only samples, the stark differences between the spectra at 418 nm confirm that dye in the FHyd-dye system is bound to the nanoparticles. The traces over the first 20 ps are enlarged in Figure 4.2b.

The kinetics of electron recombination did not change as a function of suspension pH. Kinetic traces of UV-vis spectra for a range of over 2.5 pH units (2.9-5.5) are plotted in Figure 4.4. The data are fit with a power law distribution over 0.1 to 14 μs after excitation; no model was found that adequately described both the longterm recombination rates and the first 0.1 μs after excitation. The best fits were obtained using a fixed rate constant ($1/\tau$) and variable stretching parameter (β). Though there was no change in recombination rate with time, β did increase with pH (Figure 4.4, inset). β is inversely related to the distribution of recombination rates, so although the average rate was the same for all suspension pH values, the distribution of electron recombination rates narrowed as pH increased.

Recombination kinetics were also insensitive to nanoparticle size and aggregation state. Figure 4.5 shows ΔOD over time for dye bound to 3, 4, and 5 nm FHyd. Though $1/\tau$ did not change, β increased as a function of particle size (Figure 4.5, inset), indicating that smaller nanoparticles exhibited a wider distribution of electron recombination rates. Experiments with different dye loadings caused a change in aggregation state, evidenced both by visible flocculation in suspensions with the most concentrated dye and by the

differences in aggregation seen via cryo-TEM. Cryo-TEM images of FHyd sensitized with 0-40 27DCF molecules per nanoparticle are shown in Figure 4.6.

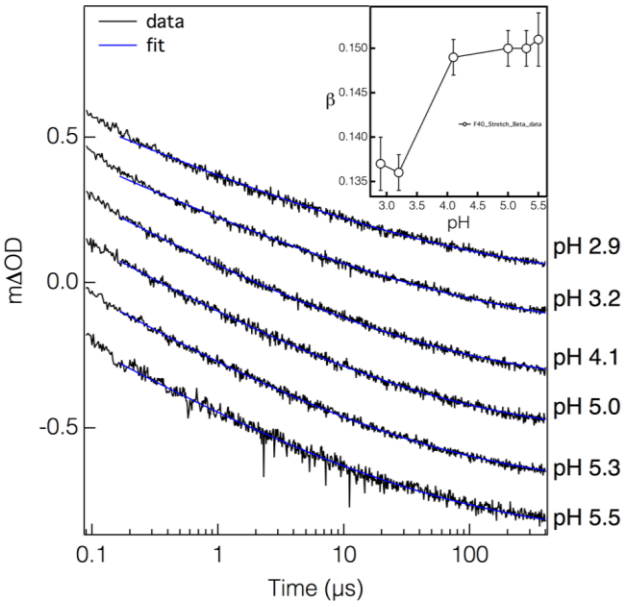

Figure 4.4: Kinetic traces at 447 nm for CDCF bound to 4 nm Fhyd nanoparticles at varying pH levels. Data (black lines) were collected via transient absorption spectroscopy and fit with a power law distribution (blue lines) using fixed rate constants (1/tau) and variable stretching parameters (beta). Inset: Beta increases with increasing pH.

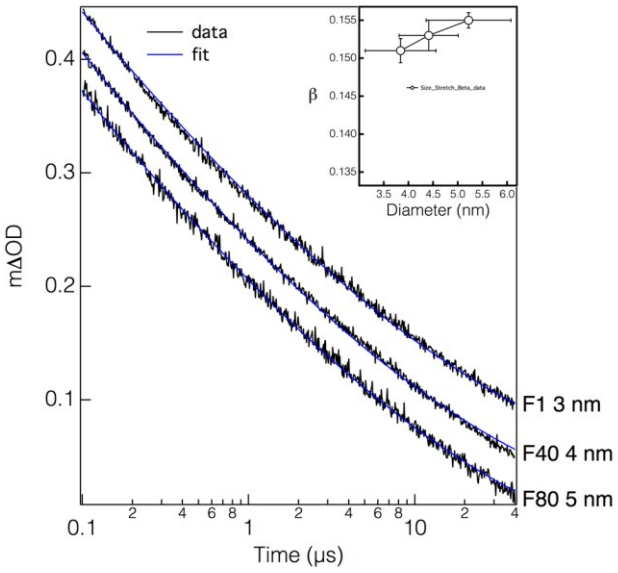

Figure 4.5: Change in absorption/kinetic traces at 447 nm for 27DCF bound to three sizes of FHyd nanoparticles as a function of time. Data (black lines) were collected via transient absorption spectroscopy and fit with a power law distribution (blue lines) using fixed rate constants (1/tau) and variable stretching parameters (beta). Inset: Beta increases with increased particle size.

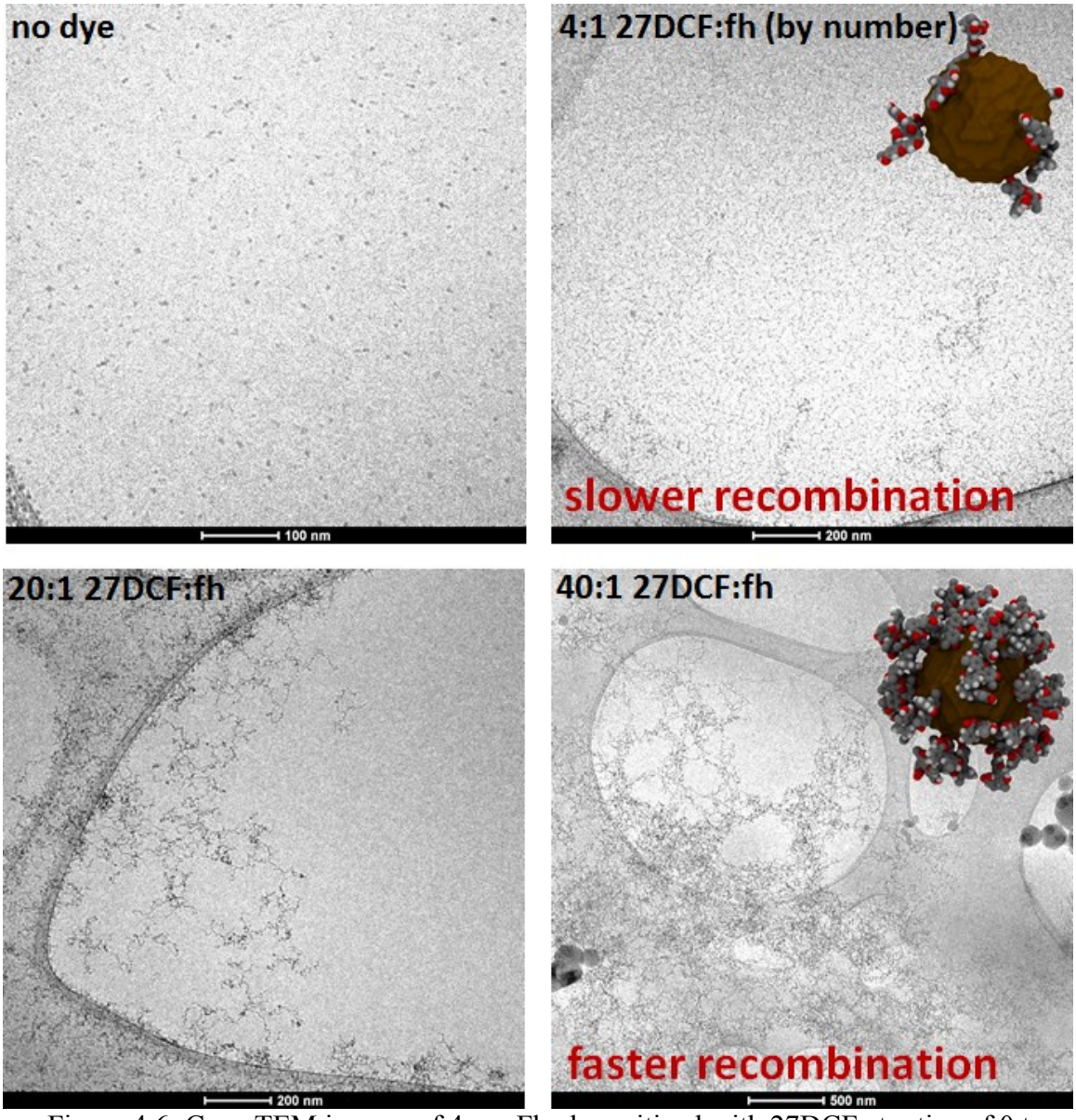

Figure 4.6: Cryo-TEM images of 4 nm Fhyd sensitized with 27DCF at ratios of 0 to 40 dye molecules per nanoparticle.

Finally, recombination kinetics was also insensitive to the number of electrons injected into the particles. Figure 4.7, top, shows the absorption of bound dye when laser pulse energy was varied from 2 to 14 μJ at pH 4 and 0.1 μs after excitation for all samples. The number of injected electrons ranged from ca. 1 to 11 electrons per nanoparticle (Figure 4.7, rightmost axis). The kinetic traces (bottom) indicate that

recombination does not vary as a function of laser power, and beta does not vary as a function of laser pulse energy (fluence).

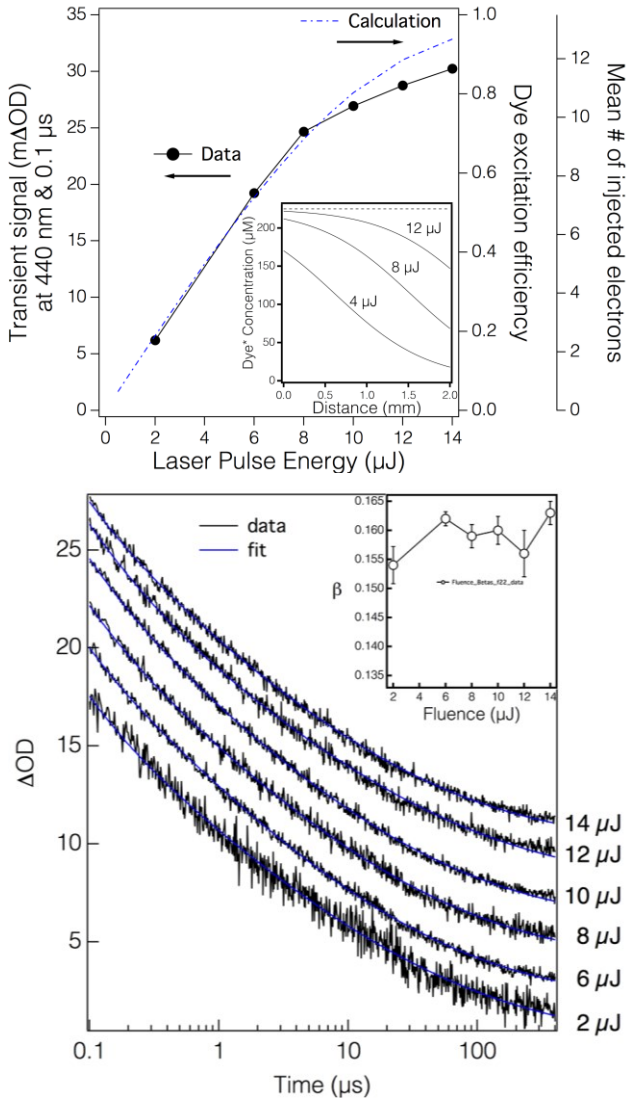

Figure 4.7: Top, left axis: Absorption at 440 nm of 27DCF bound to 4 nm Fhyd nanoparticles at pH 4, 0.1 μs after excitation. Black circles represent experimentally collected data from transient absorption spectroscopic measurements. Right axes: Calculated values of dye excitation efficiency (dashed blue line) as a function of laser fluence. The rightmost axis shows the equivalent mean number of injected electrons for these excitation efficiencies. Inset: Excited dye concentration as a function of distance at three laser pulse energies. Bottom: Kinetic traces at 418 nm for 27DCF bound to 4 nm Fhyd nanoparticles at pH 4 and varying laser pulse energy. Data (black lines) were collected via transient absorption spectroscopy and fit with a power law distribution (blue lines) using fixed rate constants (1/tau) and variable stretching parameters (beta). Inset: Beta does not vary as a function of laser fluence.

Discussion

Of the many factors tested here, none were found to have a detectable effect on electron transport rates and dye-electron recombination rates in 27DCF- and CDCF-sensitized FHyd nanoparticles. Based on modeling results that indicated electrons may be attracted to the positively charge surface of the nanoparticles, we expected that changing pH would change recombination rates, which was not the case. We then hypothesized that increasing particle size would provide a larger volumes in which the electron could travel and increase the time required for recombination, but recombination rates were similar for all nanoparticle sizes tested. Finally, we tested changes in aggregation state to probe the possibility of particle-to-particle electron transfer and rule out the possibility that electrons could travel through a volume much larger than a single particle. Aggregation state was also found to have no detectable effect on recombination rate.

The pH- and size-dependence experiments all used the same dye loading and laser pump power, resulting in the same average number of injected electrons per particle. Multiple electrons were injected in some of the aggregation studies due to higher dye loading, even though the same laser power was used. A further examination of the effects of laser fluence was warranted to rule out effects on the experiment due to high intensities.[10] This allowed us to inject multiple electrons into a single nanoparticle while maintaining a constant dye loading. The lack of change in recombination rate indicated that, in the event of multiple electron injection into a single particle, electron-electron repulsion was not rapidly forcing one or more of the injected electrons back into the oxidized dye molecules.

Having ruled out surface charge effects, nanoparticle size, particle-to-particle electron transfer, and electron-electron repulsion as possible factors affecting the average rate of

electron transport in ferrihydrite nanoparticles, we pose several possible explanations. The first two possibilities are that the injected electrons stay bound or attracted to positively-charged surface sites or positively charged dye molecules. The third, which we will expand on further, is that the injected electrons are so tightly bound to an iron atom in the interior *or* at the surface of the nanoparticles that they cannot effectively explore the entire nanoparticle volume and require longer timescales for transport and recombination.

We hypothesize that electron mobility in ferrihydrite nanoparticles is dominated by electrons caught in a deep trap state at ferrihydrite defect sites. The power law model is expected to fit when the rate of electron detrapping is much slower than the rate of intertrap diffusion[265-266] (e.g., movement between two iron atoms) and the energy barrier heights have an exponential distribution.[10] With its lack of a definitive structural model,[165-166, 169, 215-216, 218-222, 267] small size, and high surface area to volume ratio, ferrihydrite is likely to have a large number of defect sites. Small particle size and high surface curvature also contribute to under-coordination of surface atoms[268] and strained, high-energy surface structures.[96] Defect sites, such as localized charge defects in TiO_2 films[10] and oxygen-deficient iron sites in hematite nanoparticles,[224, 269] have been observed to function as deep trap states in which a larger energy barrier makes it more difficult for electrons to move from atom to atom.[269] Work in hematite demonstrated that the reduction of structural Fe(III) to Fe(II) by injected electrons was able to occur both on the surface and deep within the nanoparticles, indicating that trap states exist in both locations.[270]

It is reasonable to expect that not all trap states will have the same energy barrier, due to differences in local coordination affecting the precise properties of the defect site and the electron affinity of the trap site. "Low" and "deep" trap states are commonly described in the literature to indicate trapping sites with different energy barriers. Figure 4.8 shows a schematic of iron-to-iron electron movement in an iron oxide nanoparticle in which the three iron atoms are assigned different "levels" of electron affinity and energy barrier heights. The variety of trap state depths would explain the range of recombination times observed, perhaps due to electrons in deeper trap states requiring many escape attempts before successfully moving to a different atom. We hypothesize that the distribution of recombination times increases with particle size (β decreases) because the smallest particles have the greatest overall level of disorder and the greatest variety in the type of disorder throughout a particle. The increase in trapping site density and number of deep trap states then results in longer recombination times. Strong coupling between low and deep trap states may also increase trapping efficiency, particularly in particles with high trap density.[224] Finally, the presence of many deep trap locations would also mitigate the influence of electron-electron repulsion when multiple electrons were injected into the same nanoparticle by trapping the electrons at different sites from which they would not feel the effects of the each other.

Conclusions

We observed no dramatic pH- or size-dependent process in electron transport rates in ferrihydrite nanoparticles, nor any effect due to nanoparticle aggregation state or the injection of multiple electrons into the same nanoparticle. Indeed, redox reactions in ferrihydrite appear to be driven by electron mobility between deep trap sites, rather than electrons drawn rapidly to the positively-charged nanoparticle surface. Extrapolating

from the work with hematite by Cherepy et al., transport rates in ferrihydrite are likely to also be insensitive to adsorbed organic ligands and metal doping.[224]

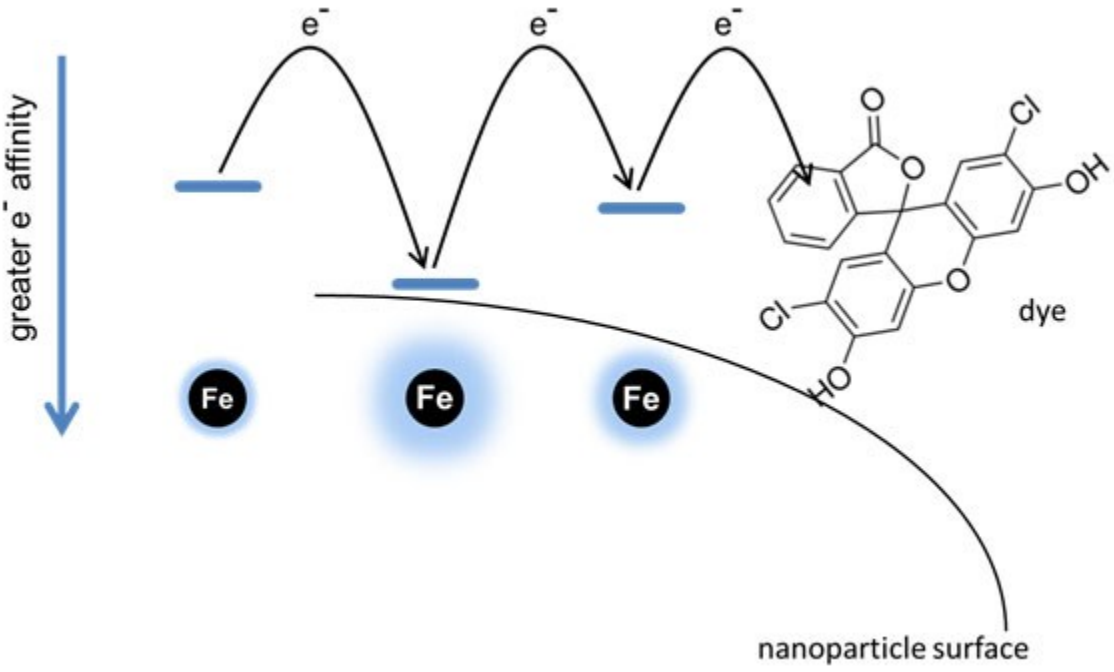

Figure 4.8: Schematic of electron movement between iron atoms of different electron affinities. Relative electron affinity is indicated by the size of the halo surrounding each atom and the depth of the trap state. The variation in electron affinity among atoms results in a variation in electron transport rates and, therefore, recombination kinetics.

Acknowledgements

B.G. was supported by the Director, Office of Science, Office of Basic Energy Sciences, of the U.S. Department of Energy (BES-DOE) under Contract No. DE-AC02-05CH11231. J.A.S. was supported by the University of Minnesota through the Nanostructural Materials and Processes Program, the Department of Chemistry Newman and Lillian Bortnick Fellowship, and the Council of Graduate Students Thesis Research Travel Grant. J.A.S. and R.L.P. were also supported by the National Science Foundation (#0957696). Parts of this work were carried out in the Characterization Facility, University of Minnesota, a member of the NSF-funded Materials Research Facilities Network (www.mrfn.org) via the MRSEC program. Research at the Molecular Foundry was supported by BES-DOE under Contract No. DE-AC02-05CH11231.

Chapter 5 : Cation-dependent hierarchical assembly of U60 nanoclusters into blackberries imaged via cryogenic transmission electron microscopy

Jennifer A. Soltis,[1] Christine M. Wallace,[2] R. Lee Penn,[1] and Peter C. Burns[2,3]

[1]Department of Chemistry, University of Minnesota, Minneapolis, Minnesota 55455, United States
[2]Department of Civil & Environmental Engineering & Earth Sciences, University of Notre Dame, Notre Dame, Indiana 46556, United States
[3]Department of Chemistry and Biochemistry, University of Notre Dame, Notre Dame, Indiana 46556, United States

Introduction

Nuclear power plants produce approximately 12% of electricity worldwide, and there is a pressing need for safe storage and re-processing of spent nuclear fuel.[271] Nuclear fuel rods have a usable lifetime of approximately 18 months, after which they must be stored in cooling pools for several years until the heat-producing nuclear reactions have decreased to a level appropriate for long-term storage.[271] The cladding on nuclear fuel rods is intended to prevent direct contact of uranium and its fission byproducts with the water of cooling pools. However, cladding failure has resulted in the deposition of uranium oxide minerals, such as studtite.[272] Uranium minerals can also precipitate when fuel and fuel waste interact with ion-rich groundwater (e.g., leakage from Hanford's waste storage tanks)[32, 273-276] and seawater (e.g., at Fukushima).[277-278]

Over the past decade, a family of uranyl peroxide clusters has been synthesized and characterized.[34, 36, 279] In each of these the exterior surface is truncated by the relatively unreactive oxygen atoms of the uranyl ions, which is consistent with their designation as polyoxometalates (POMs).[36] Most of these U-POMs are cage clusters, and many have fullerene topologies. The family includes rings, bowls, and core-shell topologies. Peroxide in these clusters bridges uranyl ions, with the peroxide bidentate to uranyl. A variety of other bridges are also incorporated into such clusters, including pyrophosphate,

oxalate, nitrate, phosphate, and hydroxyl. Actinide POMs and peroxide clusters are not limited to U, with one neptunyl peroxide cluster and a variety of Th, U, Np and Pu oxide-bearing clusters that do not contain peroxide reported.[36] Though these clusters were all synthesized in laboratory settings, and non-laboratory actinide POMs have not yet been observed, it may be possible for actinide POMs to form where water interacts with nuclear materials, especially where radiation fields are high enough to produce substantial peroxide by the radiolysis of water.[35, 279] Many POMs behave as dissolved aqueous complexes,[280] so the possibility of uranium POMs entering the groundwater or drinking water supply is particularly concerning to public and environmental health.

POMs have an array of physical properties that make them attractive as building blocks for functional nanomaterials in wide-ranging fields, including sensing, catalysis, magnetism, and biomedicine.[281-282] They are significant in part because they permit study of well-structured clusters and size-property relations, and transition metal POMs (TM-POMs) have been studied for over one hundred years.[283] POMs are sometimes referred to as macroanions due to their overall negative charge and large size as compared to other polyatomic anions.[280] They can undergo several levels of hierarchical self-assembly, and increased control over self-assembly in POMs could enable the development of new materials, including nano-structured nuclear fuels.[279, 282, 284]

POMs provide a unique opportunity to study aggregation of nanometer scale clusters in aqueous solutions. For U-POMs in particular, the high electron count of uranium provides excellent contrast with water in electron and X-ray scattering experiments. Large (1-5 nm) macroanions in solution can spontaneously self-assemble into larger, but still nanoscale, objects, and such assemblies remain stable in solution over time. Some

macroanions assemble spontaneously while others require the addition of cations or a change in the solvent composition. One type of assembly often observed is a hollow-shell spherical structure that is referred to as a blackberry.[285] Examples of POM blackberries include $[Mo_{72}Fe_{30}]$,[286-288] $[Mo_{132}]$,[38] $[Cu_{20}P_8W_{48}]$,[39] $[Mo_{154}]$,[289] and $[U_{60}]$.[40] They have been observed in both aqueous[39-40, 286, 289] and mixed solvent systems.[38]

U60 ($([UO_2(O_2)OH]_{60})^{60-}$), shown in Figure 5.1, is a U-POM nanocluster consisting of 60 uranyl peroxide hydroxide hexagonal bipyramids assembled into a fullerene topology with a diameter of 2.43 nm (as measured between the centers of bounding oxygen atoms).[34] K^+ and Li^+ counterions are also associated with the nanocluster, with specific stoichiometries dependent on solution pH and concentration. Each U^{6+} is present as typical approximately linear $(UO_2)^{2+}$ uranyl ions, and each of these linear ions is coordinated by two bidentate peroxide groups and two hydroxyl groups, which together define the equatorial vertices of a hexagonal bipyramid capped by the uranyl oxygen atoms.[34, 279] U60 was selected because it can be produced in high purity and because it is the most symmetrical of the family of uranyl peroxide clusters.[34] U60 blackberry assembly can be induced by adding cations,.[40] and the size and rate of assembly are cation-dependent, although trends are difficult to predict.[40] Recent work suggests that U60 blackberry size is inversely related to the hydrated ionic radius of added group I cations, with the exception of Li^+ and Na^+, for which no formation of blackberries was observed at the salt concentrations studied.

Blackberry POMs have been detected in solution but have not been directly imaged in situ. Small angle X-ray scattering (SAXS) and dynamic and static light scattering (DLS/SLS) have been used to characterize the average size of blackberries in situ in

solution. However, direct imaging of both TM- and U-POM blackberries is particularly difficult. Imaging techniques with the appropriate resolution, such as electron microscopy, generally require high vacuum and are incompatible with liquid specimens. In fact, it was an early attempt to image molybdenum blue assemblies in a scanning electron microscope provided evidence that they are hollow. Spheres were observed when imaging in low-vacuum environmental mode, which then burst upon exposure to high vacuum, thwarting higher-resolution imaging.[284] Drying can cause blackberries to collapse, disassemble, or aggregate in ways not representative of their in aqua state, which means that TEM images of dried specimens cannot show the structural details of nanocluster assemblies.[40, 290-291]

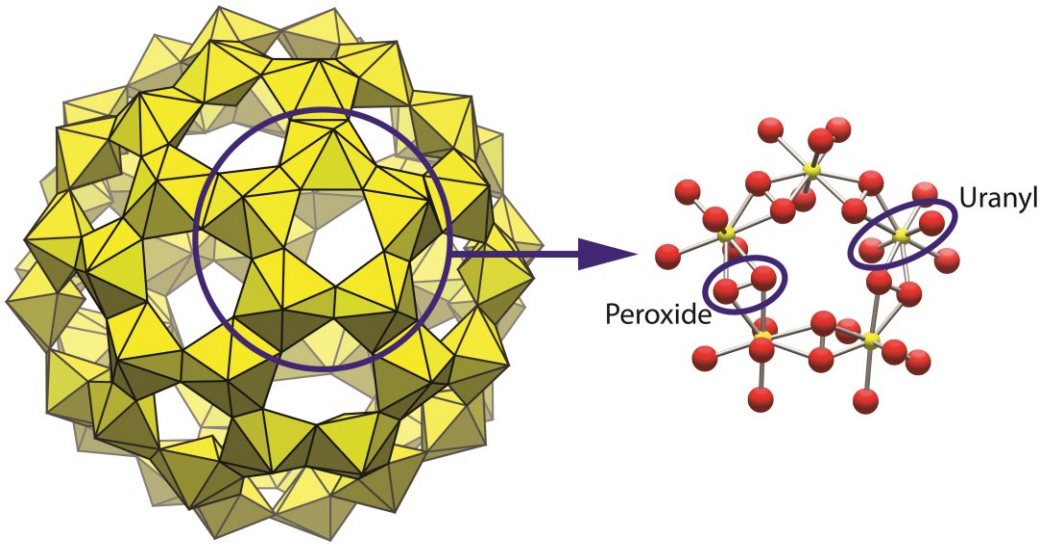

Figure 5.1. Left: Polyhedral representation of a U60 nanocluster. Hexagonal bipyramids have U(VI) at their centers and O at all vertices. Right: Ball-and-stick of a pentagonal ring composed of five bipyramidal subunits. Peroxide oxygens form bridges between subunits. Uranyl oxygens point toward the interior and exterior of the cluster. Oxygen atoms are red; uranium atoms are yellow.[34, 279]

An alternate approach is to use cryogenic (cryo) TEM. Vitrified cryo-TEM specimens preserve the *in situ* sample conformation and prevent artifacts induced by drying. The

technique has been successfully used to study the dynamics of nanoparticle aggregation, disaggregation, and growth[66, 260, 292-294] as well as aggregation state in reactive conditions.[18, 295] In this study, we use cryo-TEM to probe cation-dependent assembly of U60 nanoclusters in the presence of group I and group II cations. We present the first direct observation of *in situ* U-POM primary, secondary (blackberries), and tertiary structures, and show that structure size and morphology is cation-dependent.

Materials and Methods

Synthesis

All solutions were prepared with ultrapure water (Millipore, 18.2 MΩ·cm resistivity). U60 nanoclusters were synthesized under ambient conditions by mixing 1 mL of 0.5 M aqueous uranyl nitrate (International Bio-analytical Industries, Inc.), 0.25 mL of 0.4 M potassium chloride, and 1 mL of 30% hydrogen peroxide in a 20 mL glass vial. The pH was adjusted to approximately 9 by the repeated addition of 2.38 M lithium hydroxide in 50 μL aliquots to a total of 0.750 mL. The gradual addition of base, with swirling and shaking between additions, is critical for proper U60 cluster formation. The vials were allowed to sit open in air for 7-10 days or more until crystals of U60 clusters formed.[34] The cubic yellow crystals were recovered from the mother liquor and re-dissolved into ultrapure water to obtain monodisperse solutions.

Ultra-Small and Small Angle X-ray Scattering

Ultra small angle X-ray scattering (USAXS) and pinhole SAXS data were collected at beamline 15-ID at the Advanced Photon Source, Argonne National Laboratory. The q range of the USAXS + pinhole SAXS system is 0.001-1.2 $Å^{-1}$; therefore, sizes from ~1

nm to over 1 μm can be resolved.[296] USAXS and pinhole SAXS data were collected sequentially and merged into a single dataset with an overall *q* range of 0.001-1.2 $Å^{-1}$. Merged data were plotted as the log of intensity vs. log(q) and fitted using the Irena SAS package.[296-297]

Samples were doubly encapsulated in two Kapton capillaries, the ends of which were sealed with epoxy. Water loaded into identical capillaries was used for background measurements. Each sample type was prepared in triplicate. U60-bearing aqueous solutions were prepared by adding harvested crystals to water to achieve a concentration of 85 mg/mL. The nitrate of each target cation was added to 0.75 mL aliquots of the U60-bearing solution. Target salt concentrations were optimized to produce aggregates that persisted in solution for at least one week, and aggregate sizes were monitored by DLS during this process (details in SI, Table S1). Samples were prepared at the University of Notre Dame and loaded into Kapton capillaries before shipment to the Advanced Photon Source. SAXS data were collected six days after preparation of the samples.

Imaging

Cryo-TEM specimens of U60 solutions were prepared using 200 mesh copper grids coated with lacy carbon film (SPI Supplies) that had been glow discharged for sixty seconds in a Pelco glow discharger. Salts used in imaging experiments were sodium nitrate (J. T. Baker), magnesium nitrate (Fisher), potassium nitrate (Fisher), and calcium nitrate (Macron). Small volumes of each cation solution were added to separate 0.75 mL aliquots of 1.0 mg/mL (crystals/water) U60 with shaking. Time zero was designated as the time of cation addition. The relative differences in concentration among the cations were the same as for SAXS experiments (e.g., $[Na^+]$:$[Mg^{2+}]$). Final salt concentrations

are listed in Table 5.S1. No more than 20 μL of any cation solution was added to a U60 aliquot so that the concentration of U60 would be minimally affected.

A lower concentration of U60 was used for cryo-TEM than for SAXS so that nanocluster concentration would not be too dense for imaging. At specified times, 3 μL aliquots were removed and applied to the carbon side of a TEM grid that had been loaded into a Vitrobot automated plunge freezer (FEI Mark IV). The grid was then blotted with filter paper for 2 seconds (-2 mm offset), allowed to relax for 1 second, and plunged into liquid ethane. The typical thickness of a vitrified film is several hundred nm. The vitrified specimen was then transferred to a storage box under liquid nitrogen. The time recorded was the time between cation addition and vitrification, as determined by the instant the grid plunged into the ethane. All further handling was performed under liquid nitrogen to maintain cryogenic conditions.

Specimens with no added cations were also prepared by vitrifying aliquots of both fresh and aged U60 solutions (1.0 mg/mL crystals/water). The aged solution had been stored at high concentration (59 mg/mL crystals/water) at room temperature for seven months prior to dilution to 1 mg/mL several hours before to vitrification.

Imaging was performed using an FEI Tecnai G^2 F30 field-emission gun TEM equipped with a cryo stage and a Gatan UltraScan camera and operated at 300 keV under low-dose conditions. Images were collected with Digital Micrograph v3 and processed with ImageJ v1.48q (a public domain image processing and analysis program from the National Institutes of Health[199]). Photoshop CS2 was used for montage layouts. Images were altered by cropping and/or linear adjustments of brightness and contrast only.

Image analysis

TEM images are, by nature, two-dimensional representations of three-dimensional objects, which means that clusters may appear to overlap or be entirely hidden by others in the projected image. Because of this, the quantity of U60 clusters per blackberry is calculated from structure size and not by counting individually discernable clusters in the TEM images.

Major and minor axis lengths of blackberries were measured by assigning corresponding ellipses in ImageJ. Non-elliptical structures, referred to below as "tertiary structures," were measured by assigning individual ellipses to each elliptical area of the structure. All reported lengths refer to the average major axis length with one standard deviation. The differences in average major axis length were compared using a one-tailed, homoscedastic (two-sample, equal variance) T-test to determine statistical significance.

Surface area (S) was calculated assuming a prolate ellipsoid (two minor axes of equal length) using the approximation

$$S \approx 4\pi \left(\frac{2(ab)^{1.6} + (bb)^{1.6}}{3} \right)^{\frac{1}{1.6}}$$

where a and b are the lengths of the major and minor semiaxes, respectively.

The diameters of 30 individual U_{60} clusters were measured with the line tool and the average diameter of 2.5 ± 0.3 nm is in close agreement with the exterior diameter measurement of 2.43 nm from single crystal X-ray diffraction.[34]

The spacing between assembled clusters within a blackberry was taken from the average center-to-center distance between clusters within a blackberry as calculated from SAXS measurements. Corresponding values for each of the four cations were used; these

measurements ranged from 2.7 to 3.0 nm (Table 5.S2). The cross-sectional area of an individual nanocluster was modeled as a circle, using the center-to-center distance as the cluster diameter. An approximate number of U60 nanoclusters per blackberry was calculated by dividing the total surface area of a blackberry by this cross section and multiplying by ρ, the packing density of identical circles on a spherical surface. Packing density depends on the size of the circles and sphere, and exact solutions are often non-trivial, so ρ = 0.90690 for packing on the surface of an infinite sphere was used to provide an upper limit to the number of nanoclusters in secondary and tertiary structures.[298] Adjustments to account for the elimination of surface area at the interface between adjacent blackberries in a tertiary structure were omitted from calculations, again providing an upper limit on the number of nanoclusters per structure.

Nomenclature

Samples are labeled with the cation used to induce blackberry formation. For example, a Mg-U60 blackberry is composed of U60 nanoclusters that formed after addition of $Mg(NO_3)_2$ (aq).

Results

Small-Angle X-ray Scattering

Data from SAXS measurements demonstrate the formation of secondary structures and the presence of isolated U60 clusters in U60 solutions after addition of solutions of group I and group II nitrates (Figure 5.2). The final concentration of the added nitrates was tuned to achieve assembly in the timeframe of our studies (Table 5.S1), and no

assembly was observed with added Li; as such, comparison of the sizes of the resulting secondary structures derived from the scattering data is of limited value.

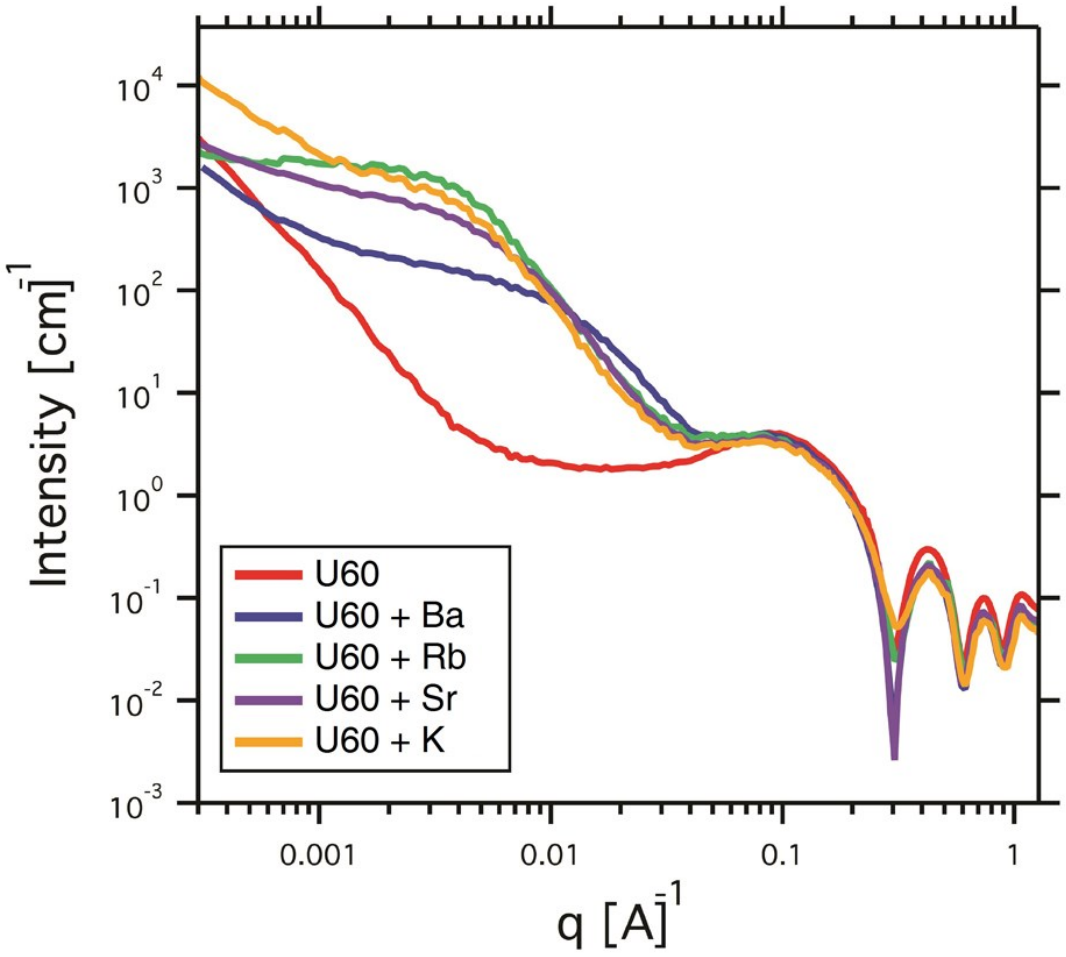

Figure 5.2. USAXS and pinhole-SAXS data for aqueous solutions containing 85 mg/mL of dissolved U60 crystals and additional group I (A) and group II (B) cations. Details of solution compositions are provided in the SI.

The scattering data confirm that U60 clusters persist after onset of blackberry formation. These data were also used to determine the interaction distances between U60 clusters within the blackberries. U60 nanoclusters in crystals containing K^+ and Li^+ counterions have hard sphere radii of 2.68 nm. The corresponding values for U60 solutions with added cations range from 2.47 to 3.15 nm (Table 5.S2). Thus, the scattering data indicate that the center-to-center distances of U60 clusters in blackberries

are very similar to those in solid U60 crystals, which supports the hypothesis that the linkages of POMs in blackberries are cation mediated.

The SAXS data in the low and mid-*q* region (<0.01 $Å^{-1}$) contain information about the sizes and shapes of blackberries in solution. However, identical scattering patterns may arise from blackberries with different size and shape distributions. The observed data show dramatic variations across the range of added cations (Figure 5.2). The observed variability, and difficulty in modeling and interpreting that variability, prompted our efforts to image these systems using cryo-TEM.

Cryogenic Transmission Electron Microscopy

Isolated U60 clusters can be discerned in cryo-TEM images collected prior to significant assembly of blackberries (

Figure 5.3). The sensitivity of the vitrified solution to electron beam damage prevents collection of higher resolution images, but the images are sufficient to identify individual clusters. Specifically, the image shows 2.5 nm U60 clusters spatially isolated from each other. The cluster size is consistent with the center-to-center distances obtained using SAXS.

Cryo-TEM images of U60 solutions vitrified at specified times after cation addition demonstrate that added nitrates of Na^+, K^+, Mg^{2+}, and Ca^{2+} quickly induced a change from isolated clusters (monomers) to secondary structures comprised of tens to hundreds of individual clusters. The addition of divalent cations induced the formation of blackberries, while the addition of monovalent cations induced the formation of even larger, sometimes tertiary, structures.

In the case of the divalent cations, blackberries grow larger as time progresses, which is inconsistent with the "direct jump" to equilibrium size hypothesized by Liu.[285] Figure 4 shows cryo-TEM images of samples vitrified at specified times after Mg^{2+} or Ca^{2+} addition. Each image is labeled with the added cation and time, in minutes, between cation addition and vitrification. In the image of Ca24, several blackberries appear to be touching. However, this image cannot discern the relative positions of the blackberries along the direction of the electron beam, so it is uncertain if the blackberries are in contact with each other or at different heights with respect to the thickness of the film of vitrified water.

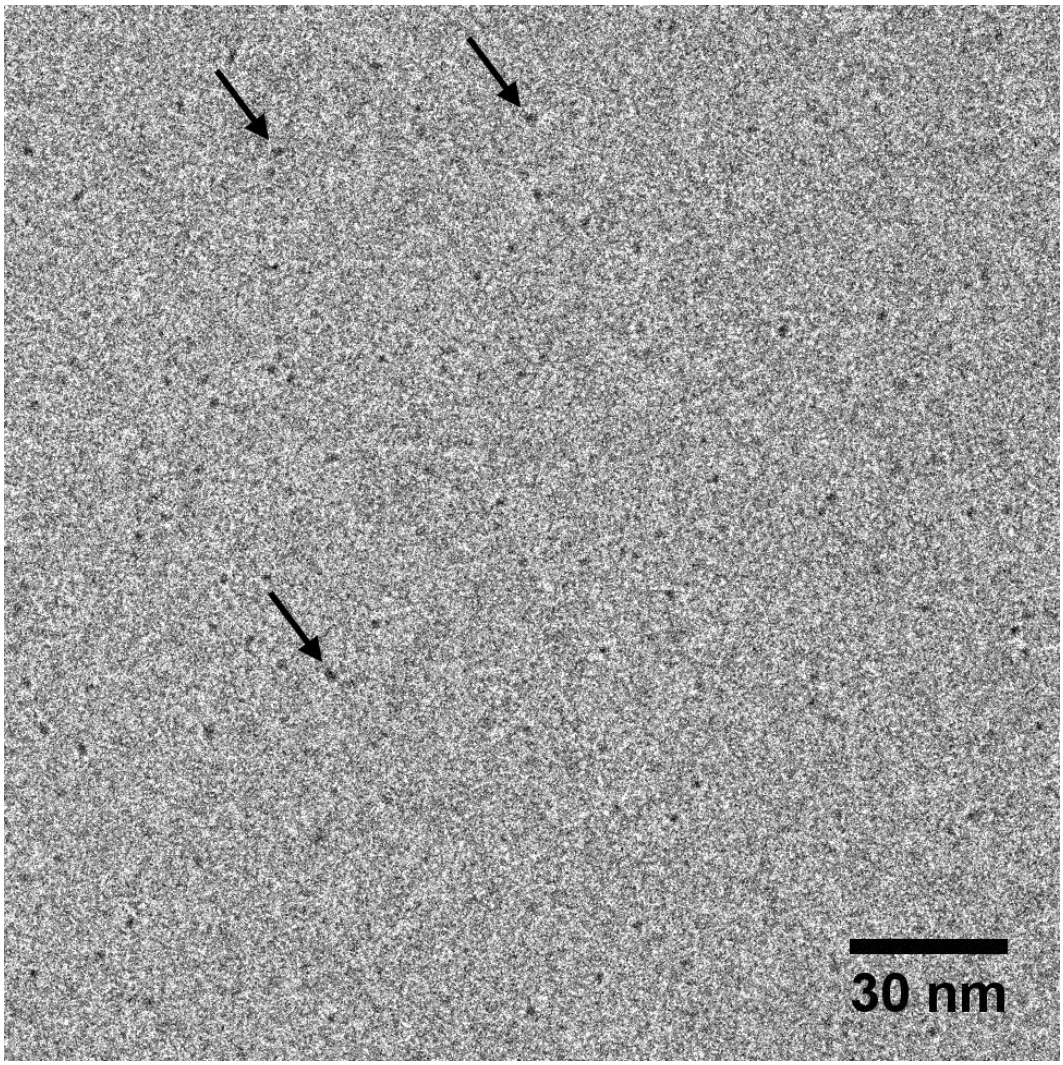

Figure 5.3: Cryo-TEM image of U60 nanoclusters vitrified before the addition of cations. Several nanoclusters are indicated by arrows to guide the eye.

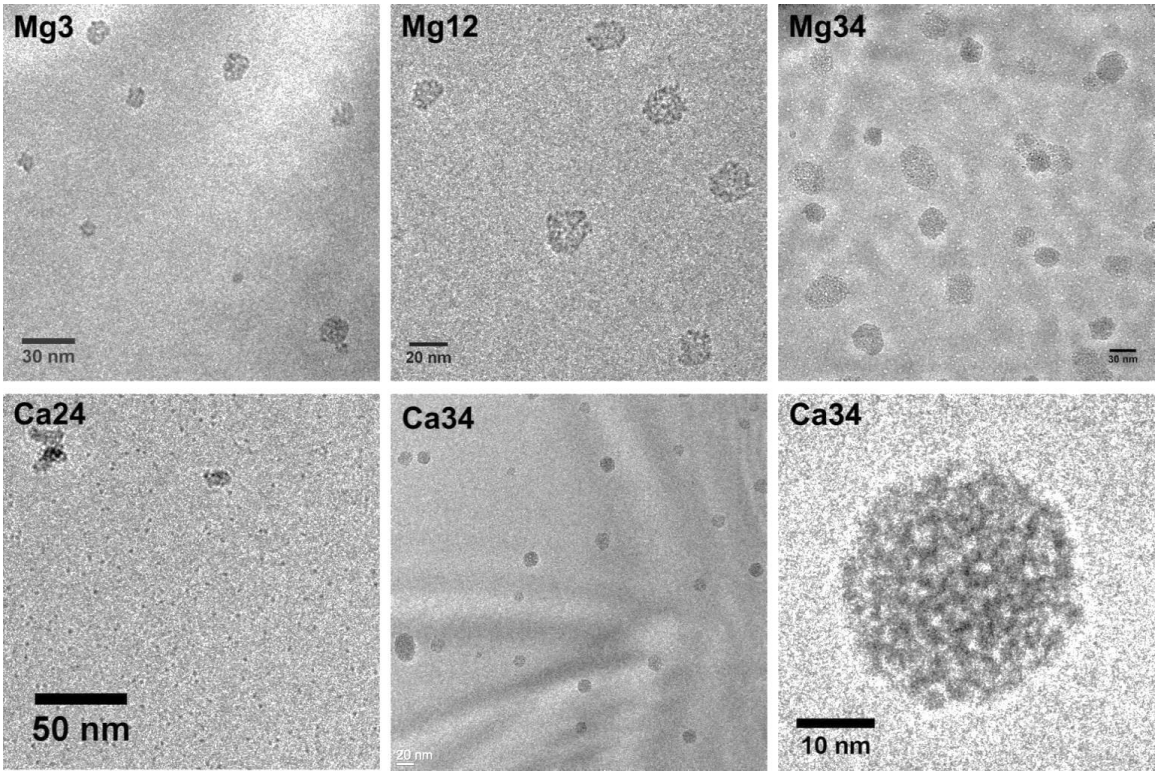

Figure 5.4: Cryo-TEM images of blackberries formed from U60 solutions vitrified after the addition of $Mg(NO_3)_2$ or $Ca(NO_3)_2$. Images are labeled with the cation added and the time, in minutes, between cation addition and vitrification.

The relatively even contrast at the edge and center of each blackberry (Figure 5.4) is consistent with the hypothesis that these structures are hollow. Solid spheres would be expected to have greater contrast at their center due to increased mass/thickness contrast, whereas hollow spheres with dense walls would appear to have a "rind" in TEM images.[299] A TEM image of a circle with even contrast is consistent with round plates ("pancakes") or hollow spheres with less-dense walls. Tilting experiments demonstrated that the blackberries are roughly spherical, therefore we conclude that they are hollow, which is in good agreement with models of POM blackberries previously reported.[38, 40, 286, 289]

The lower right image of Figure 5.4 is representative of the secondary structures observed when divalent cations were added. This blackberry is about 32 × 32 nm and

consists an estimated 390 U60 clusters. Some individual U60 clusters can be discerned within the blackberry structures, particularly in smaller blackberries or near the edges of larger ones. Lighter gaps can be discerned between dark areas that correspond to individual clusters in the cryo-TEM images, as in

Figure 5.3 and Figure 5.4. These gaps presumably contain water and counter-cations that stabilize the assembly of clusters into larger structures, as discussed below.[40]

Though both of the divalent cations used induced the formation of blackberries, blackberry size and rate of assembly were cation-dependent. Figure 5.5 shows the average major axis length of the blackberries as a function of time. Mg-U60 blackberries formed more rapidly, and were larger overall, than Ca-U60 blackberries, and the difference in size after 34 minutes was statistically significant (p-value $< 1 \times 10^{-7}$). Average blackberry aspect ratios ranged from 1.1 to 1.3 for both Mg-U60 and Ca-U60 and were independent of blackberry size. The dashed line at 2.5 nm corresponds to the diameter of individual U60 clusters; open symbols on this line indicate times at which images were collected but only U60 monomers were observed.

Interestingly, only monomers were seen in Mg-U60 samples vitrified one and 24 hours after Mg^{2+} addition. We attribute this to settling of larger structures or precipitation of U60 onto the walls and bottom of the container, which was observed while preparing samples for SAXS measurements and is known to occur at the cation concentrations used here (above the critical salt concentration).[40]

In contrast to the quite spherical blackberries observed with addition of the divalent cations, sodium and potassium cations induced the formation of large, fractal-like tertiary structures. These results are at odds with previous reports describing the formation of

spherical blackberries.[38, 285, 289] Here, "tertiary structures" are defined as any large structure that can be outlined in a cryo-TEM image by two or more ellipses. We show later that these structures may be tertiary structures assembled from blackberry building blocks.

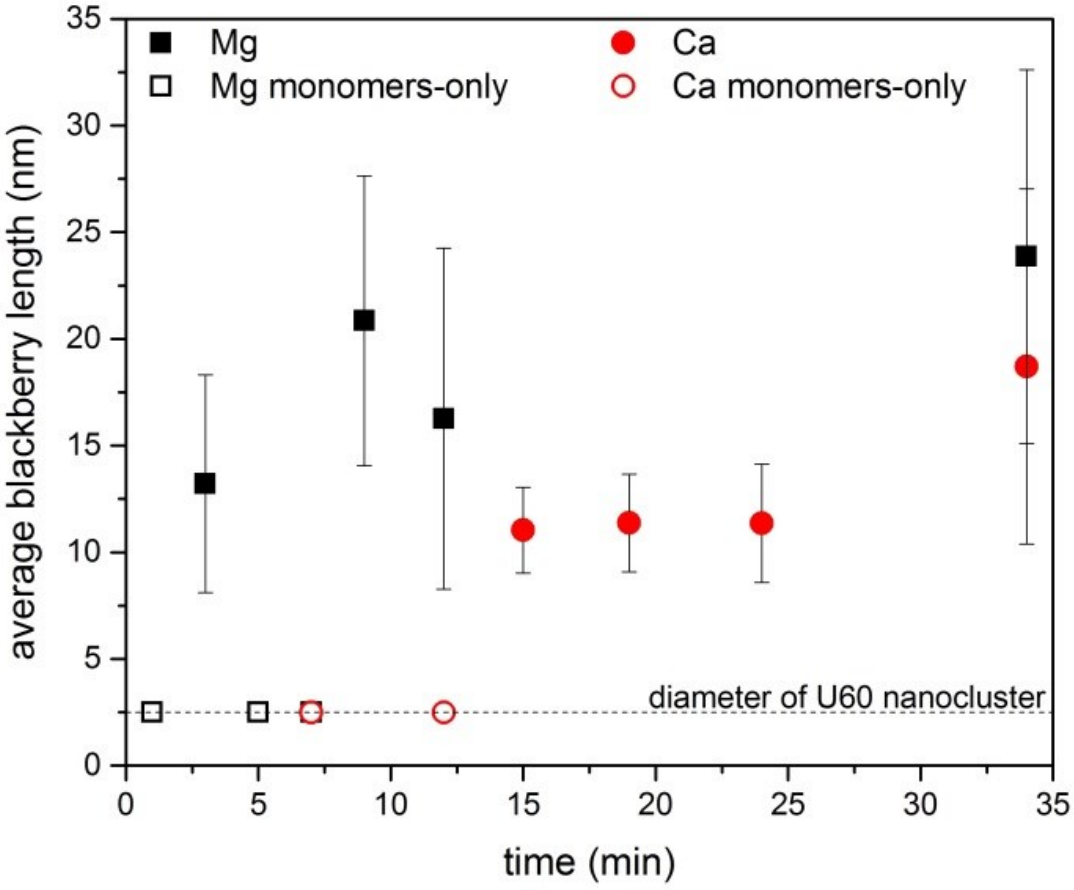

Figure 5.5: The average length of blackberries increases with time when Mg^{2+} or Ca^{2+} are added to a U60 solution. Blackberry length was measured from calibrated cryo-TEM images and error bars represent the first standard deviation.

Figure 5.6 shows cryo-TEM images in which primary, secondary, and tertiary structures can be discerned. At earlier stages of assembly, monomers and blackberries are observed (top row, images Na12 and K10). Some structures may have already reached a tertiary level of assembly, particularly those in the image labeled "K10" that appear to be composed of two or three blackberries. At later stages, the tertiary structures have

increased in size and taken on a fractal-like appearance (Figure 6, bottom row, images Na28 and K15).

The formation of secondary and tertiary structures when monovalent cations were added was also cation-dependent. The average number of U60 clusters per tertiary structure is plotted as black squares in Figure 5.7. Error bars represent the smallest and largest clusters observed for each sample. Large tertiary structures, up to thousands of nanoclusters in size, were rapidly formed in solutions containing K^+. Tertiary structures in Na-U60 solutions formed more slowly, and were smaller, than those with K^+.
The fraction of nanoclusters residing in tertiary structures was determined by comparing the number of U60 nanoclusters residing in tertiary structures to the number of U60 clusters in secondary (blackberry) and tertiary structures combined (i.e., all non-monomer clusters). These values are represented by grey bars in Figure 5.7. Average tertiary structure size did not directly correspond to the fraction of nanoclusters residing in tertiary structures. For example, average structure size decreased in Na-U60 between 15 and 28 minutes, but the fraction of nanoclusters in tertiary structures increased over the same time period. This may indicate that the sedimentation of larger structures had begun as the remaining monomers were incorporated into smaller tertiary structures. Sedimentation is also likely in the 32 minute sample, in which less than 20% of nanoclusters residing in tertiary structures was observed. Notably, 100% of U60 clusters resided in tertiary structures only 15 minutes after addition of K^+. Small tertiary structures were also observed at a few sampling times for Mg-U60 and Ca-U60, but these structures did not persist and included less than 40% of the non-monomer nanoclusters.

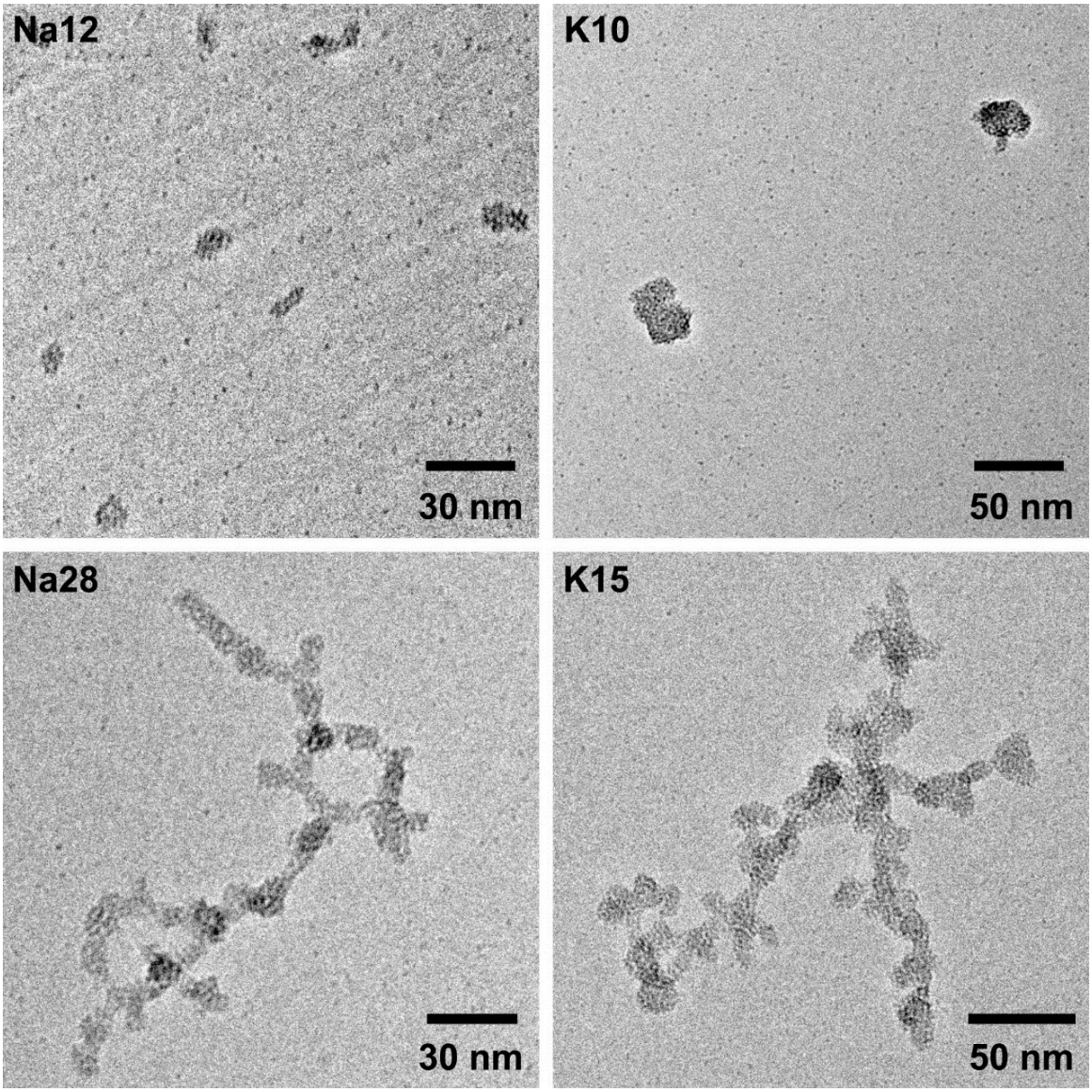

Figure 5.6: Cryo-TEM images of Na-U60 after 12 and 28 min and K-U60 after 10 and 15 min. Both cations induced the formation of small blackberries at early times that eventually grew into fractal-like structures. This is proposed to be a tertiary level of self-assembly.

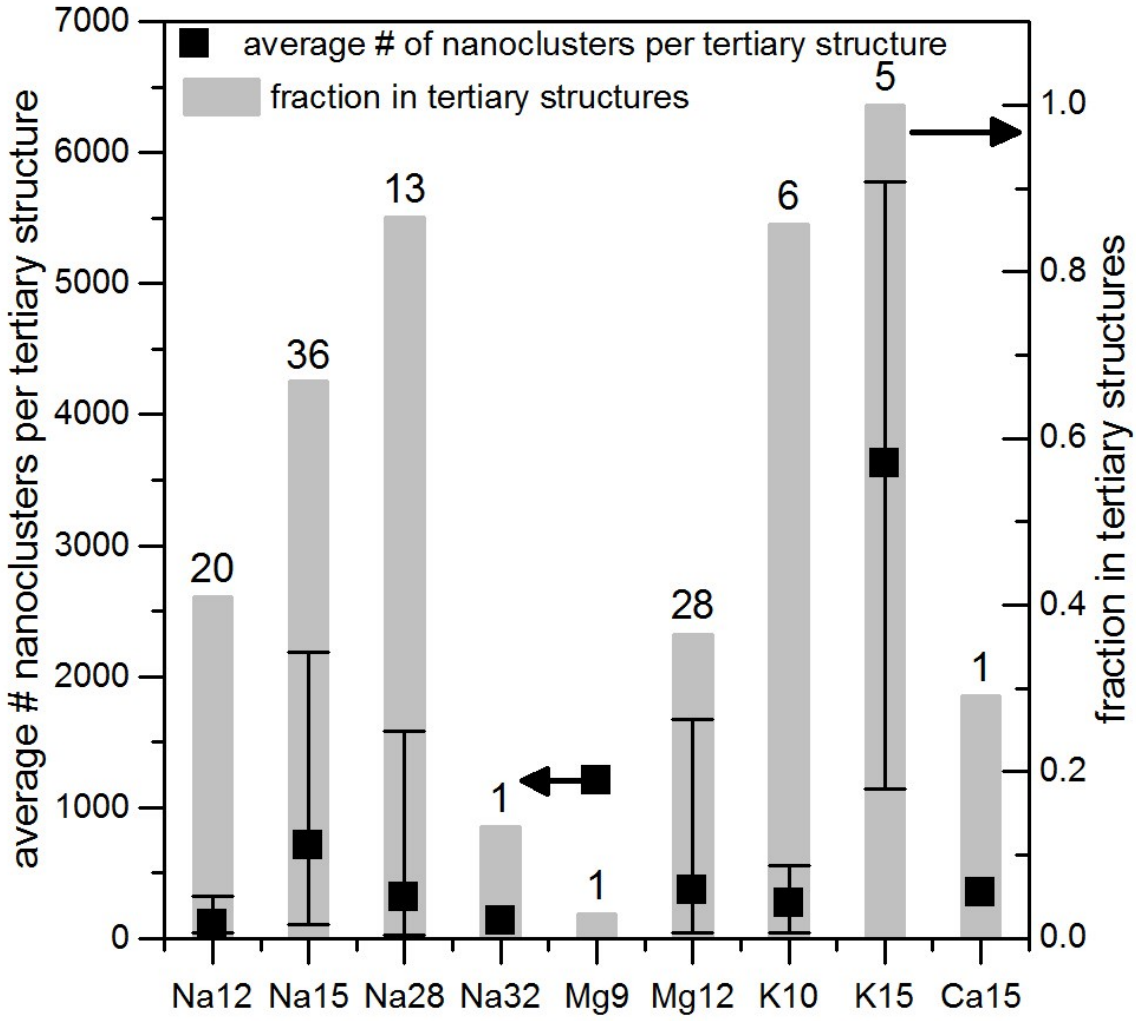

Figure 5.7: Left axis, black squares: The number of U60 nanoclusters per tertiary structure. Error bars show the smallest and largest tertiary structure observed in each sample and are omitted for samples in which only one tertiary structure was observed. The number of tertiary structures observed in each sample is indicated by the numbers above the grey bars. Right axis, grey bars: The fraction of U60 nanoclusters residing in tertiary structures compared to U60 nanoclusters residing in blackberries and tertiary structures combined. The number of nanoclusters in tertiary structures increases with time when group I cations are added. Tertiary structures are occasionally present in group II cation samples. In both plots, missing bars indicate samples with blackberries but no tertiary structures.

These data do not enable us to discern whether the tertiary structures are assembled from secondary blackberries or by monomer-by-monomer addition. Blackberry and tertiary structure assembly are dynamic processes, and cryo-TEM is only able to provide

snapshots. Use of a real-time imaging technique such as fluid cell TEM would provide valuable insight into this problem. Nevertheless, available data support the hypothesis that the large structures observed in Na-U60 and K-U60 are tertiary assemblies based on blackberry secondary building blocks. A comparison of the average major axis length for isolated blackberries and those incorporated as secondary structural building blocks of the tertiary structures, plotted in Figure 5.8, shows that both categories of blackberries are of similar size. The differences in average blackberry lengths between the two categories for each sample are statistically indistinguishable (all p-values > 1), and the blackberries also have similar aspect ratios.

Finally, isolated U60 clusters were visible in all samples after the addition of Ca^{2+}, K^{+}, and Na^{+}, even in the presence of blackberries or tertiary structures. This indicates that either there was insufficient cation present to cause aggregation of all U60 clusters, that insufficient time transpired for complete aggregation, or perhaps that a steady state had been achieved between aggregation and disaggregation. With the exception of the sample vitrified after 3 minutes, which had both small blackberries and monomers, no isolated U60 clusters were observed in the presence of Mg-U60 blackberries.

Mechanisms of Secondary and Tertiary Structure Formation

Assembly of transition metal (TM) POMs into blackberries occurs predominantly in systems of large POMs with low charge density,[283] criteria that are also met by U-POMs. The addition of cations to U60 solutions facilitates assembly into blackberries and tertiary structures, presumably through a cation-mediated mechanism.[38, 40, 300]

Lower net surface charge when divalent cations are added could explain why blackberries observed in the Mg-U60 and Ca-U60 solutions are larger than those formed

with monovalent cations. However, Mg-U60 blackberries were larger than Ca-U60 blackberries, which is inconsistent with the observation by Gao et al. that cations with smaller hydrated sizes form larger blackberries (Mg^{2+} has a larger hydrated size than Ca^{2+}). While their study was also performed at 1 mg/mL U60 crystals in water, the concentrations of monovalent cations used were all below the critical salt concentration, so this may not be directly comparable to our work with divalent cations at concentrations above the critical salt concentration.[40]

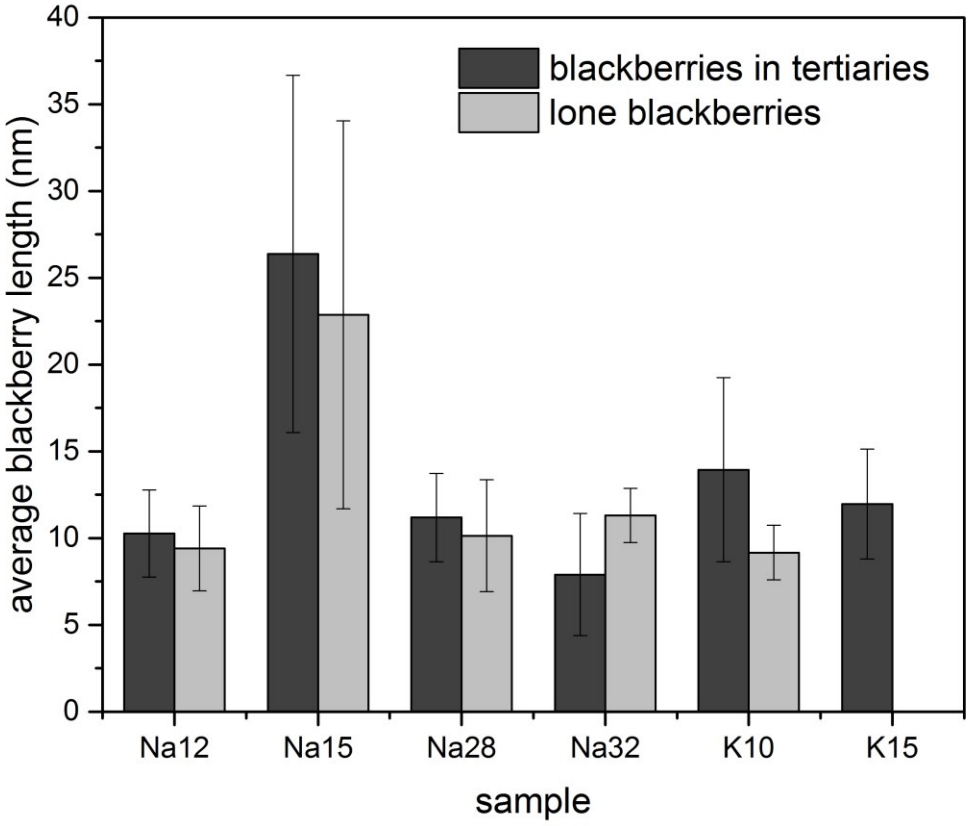

Figure 5.8: A comparison of major axis length in blackberries used as building blocks of tertiary structures (dark grey) and isolated blackberries not incorporated into tertiary structures (light grey). Samples are labeled with the cation added and the time (in min) between cation addition and vitrification. Within each pair of bars, the average sizes for the two types of blackberries were statistically indistinguishable. Error bars represent the first standard deviation. There were no isolated blackberries observed in sample K15.

In the presence of monovalent cations, trends in blackberry and tertiary structure size are consistent with the dependence on hydrated cation size observed by Gao *et al*., who proposed that ions with smaller hydrated radii are preferred because they fit more easily into the available bonding sites on the nanoclusters.[40] K^+, which has a smaller hydrated radius than Na^+, generally led to larger tertiary structures and larger blackberries (all p-values statistically significant). Unlike in the work of Gao *et al.,* blackberry and tertiary structure formation was observed after Na^+ was added to a U60 solution, which can be attributed to the much higher concentration of added cation.

Blackberry formation without added cations

Figure 5.9 shows a cryo-TEM image of blackberries in a U60 solution that was not treated with additional cations, but had simply been aged. This is the first observation of U60 blackberries formed without adding cations.[40] Imaging of the aged U60 solution revealed blackberries averaging 17.7 ± 10.4 nm in major axis length. One possible explanation for the presence of these blackberries is a decrease in interaction distance between U60 nanoclusters as cluster concentration increases, which forces the nanoclusters closer together. Calculated effective charge drops as U60 concentration increases,[40] which may facilitate assembly of nanoclusters into blackberries, just as when cations are added to decrease nanocluster charge density. We hypothesize that, once formed, the blackberries are stable and do not disassemble upon dilution due to side-on bonding of cations between neighboring nanoclusters. Although extra cations were not added, Li and K present from the original synthesis may be available for cluster-to-cluster bonding.

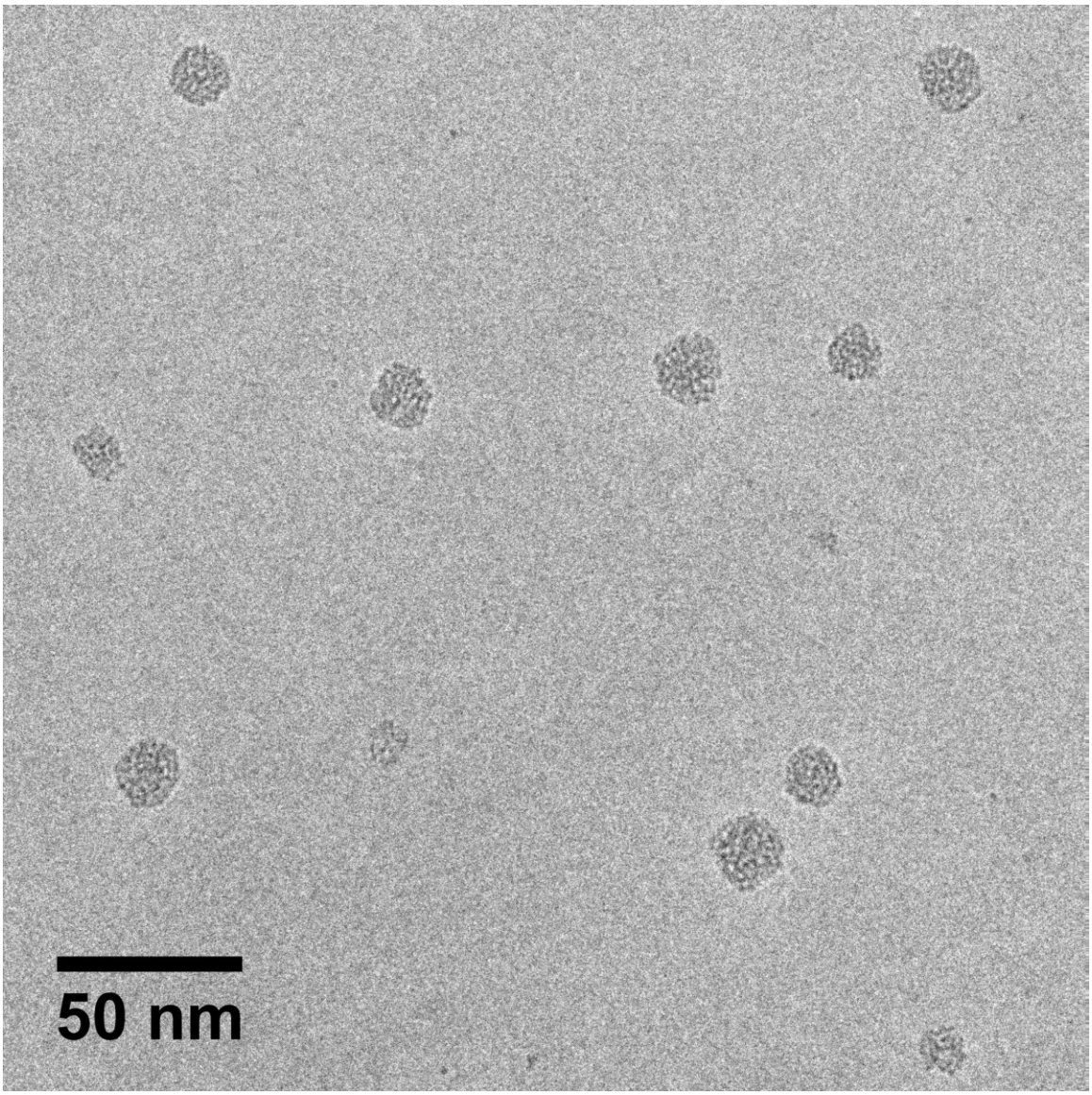

Figure 5.9: Cryo-TEM image of blackberries formed from a U60 solution (59 mg/mL) with no added cation aged at room temperature for seven months and diluted to 1 mg/mL prior to vitrification.

Commentary on representative measurements

One of the major limitations of TEM is the vanishingly small amount of sample that can be imaged. A single high-resolution TEM image may contain only attograms of material, [74] and the average blackberry and fractal structure sizes are reported from the measurement of as few as 11 or as many as 355 blackberries and as few as one or as

many as 36 tertiary structures. Conclusions about large populations based on such small sample sizes must be done with caution, and the use of complementary techniques such as SAXS and DLS can lend important insight into characteristics that are representative of a larger amount of sample.

Conclusion

Cryo-TEM has been used for the first time to image blackberries assembled from POMs *in situ* and to provide time-resolved insights into their formation. U60 nanoclusters are ideal for this type of study because they are stable, high symmetry clusters with very high electron density, which provides for excellent contrast relative to the vitrified solvent. Images collected for aqueous solutions of U60 with various added cations indicate that U60 can be induced to self-assemble into secondary and tertiary structures. The addition of divalent cations produced hollow, near-spherical blackberry structures. The addition of monovalent cations yielded both blackberries and tertiary structures, with rates of inclusion of nanoclusters into tertiary structures as high as 100%. Both kinetics of assembly and the size and morphology of the assembled structures depend on cation identity. The images collected here have provided the size and shape of structures that have previously been analyzed only as averages of bulk samples.

Cryo-TEM is a promising technique for further studies of U-POM superstructures and any sample that significantly altered by drying. Further work with techniques such as fluid cell TEM could also lend insight into the dynamics of U60 cluster assembly and answer questions about the reversibility of assembly, changes in blackberry size with time, and the possibility of tertiary structure formation from blackberries versus direct assembly of monomers into fractal-like structures.

Supplemental Information

Table 5.S1: Solution compositions for SAXS measurements

Sample	Nitrate	$[Nitrate]_{final}$ (mM) for SAXS	$[Nitrate]_{final}$ (mM) for cryo-TEM	Cation:U
U60+Li	$LiNO_3$	100	---	1177
U60+Na	$NaNO_3$	23	1.55×10^{-4}	275
U60+K	KNO_3	20	1.32×10^{-4}	235
U60+Rb	$RbNO_3$	17	---	196
U60+Cs	$CsNO_3$	23	---	275
U60+Mg	$Mg(NO_3)_2$	8.7	5.73×10^{-5}	102
U60+Ca	$Ca(NO_3)_2$	10	6.60×10^{-5}	118
U60+Sr	$Sr(NO_3)_2$	6.7	---	78.4
U60+Ba	$Ba(NO_3)_2$	4.0	---	47.1

Table 5.S2: Center-to-center distance between U60 clusters in nitrate-containing solutions

Sample	Nitrate	Interaction distance (nm)
U60+Li	$LiNO_3$	2.53
U60+Na	$NaNO_3$	2.85
U60+K	KNO_3	2.86
U60+Rb	$RbNO_3$	3.15
U60+Cs	$CsNO_3$	2.94
U60+Mg	$Mg(NO_3)_2$	2.71
U60+Ca	$Ca(NO_3)_2$	3.04
U60+Sr	$Sr(NO_3)_2$	2.47
U60+Ba	$Ba(NO_3)_2$	2.56

References

1. Wilczewska, A. Z.; Niemirowicz, K.; Markiewicz, K. H.; Car, H., Nanoparticles as drug delivery systems. *Pharmacol. Rep.* **2012,** *64* (5), 1020-1037.
2. Freestone, I.; Meeks, N.; Sax, M.; Higgitt, C., The Lycurgus Cup — A Roman nanotechnology. *Gold Bull* **2007,** *40* (4), 270-277.
3. Banfield, J.; Zhang, H., Nanoparticles in the environment. *Rev. Mineral Geochem* **2001,** *44* (1), 1-58.
4. Zaera, F., New Challenges in Heterogeneous Catalysis for the 21st Century. *Catalysis Letters* **2012,** *142* (5), 501-516.
5. Roldan Cuenya, B., Metal Nanoparticle Catalysts Beginning to Shape-up. *Accounts of Chemical Research* **2012,** *46* (8), 1682-1691.
6. Petryayeva, E.; Algar, W. R., Proteolytic Assays on Quantum-Dot-Modified Paper Substrates Using Simple Optical Readout Platforms. *Anal. Chem.* **2013,** *85* (18), 8817-8825.
7. Zijlstra, P.; Orrit, M., Single metal nanoparticles: optical detection, spectroscopy and applications. *Reports on Progress in Physics* **2011,** *74* (10), 106401.
8. Mizusawa, K.; Tsukamono, A.; Itoh, A., FePt grains for magnetic storage on layer of self-assembled silica nanoparticles. *Journal of Materials Research* **2011,** *26* (02), 205-208.
9. Borchert, H., Elementary processes and limiting factors in hybrid polymer/nanoparticle solar cells. *Energy Environ. Sci.* **2010,** *3*, 1682-1694.
10. McNeil, I. J.; Ashford, D. L.; Luo, H.; Fecko, C. J., Power-Law Kinetics in the Photoluminescence of Dye-Sensitized Nanoparticle Films: Implications for Electron Injection and Charge Transport. *J. Phys. Chem. C* **2012,** *116* (30), 15888-15899.
11. Usman, A. R. A.; Kuzyakov, Y.; Lorenz, K.; Stahr, K., Remediation of a soil contaminated with heavy metals by immobilizing compounds. *J. Plant Nutr. Soil Sci.* **2006,** *169* (2), 205-212.
12. Anawar, H. M.; Akai, J.; Komaki, K.; Terao, H.; Yoshioka, T.; Ishizuka, T.; Safiullah, S.; Kato, K., Geochemical occurrence of arsenic in groundwater of Bangladesh: sources and mobilization processes. *J. Geochem. Explor.* **2003,** *77*, 109-131.
13. Stipp, S. L. S.; Hansen, M.; Kristensen, R.; Hochella Jr, M. F.; Bennedsen, L.; Dideriksen, K.; Balic-Zunic, T.; Léonard, D.; Mathieu, H. J., Behaviour of Fe-oxides relevant to contaminant uptake in the environment. *Chemical Geology* **2002,** *190* (1–4), 321-337.
14. Penn, R. L.; Banfield, J. F., Imperfect Oriented Attachment: Dislocation Generation in Defect-Free Nanocrystals. *Science* **1998,** *281* (5379), 969-971.
15. Penn, R. L.; Banfield, J. F., Oriented attachment and growth, twinning, polytypism, and formation of metastable phases: Insights from nanocrystalline TiO_2. *Am. Mineral.* **1998,** *83* (9-10), 1077-1082.
16. Penn, R. L.; Banfield, J. F., Formation of rutile nuclei at anatase {112} twin interfaces and the phase transformation mechanism in nanocrystalline titania. *Am. Mineral.* **1999,** *84*, 871-876.
17. De Yoreo, J. J.; Gilbert, P. U. P. A.; Sommerdijk, N. A. J. M.; Penn, R. L.; Whitelam, S.; Joester, D.; Zhang, H.; Rimer, J. D.; Navrotsky, A.; Banfield, J. F.; Wallace, A. F.; Michel, F. M.; Meldrum, F. C.; Cölfen, H.; Dove, P. M., Crystallization

by Particle Attachment in Synthetic, Biogenic, and Geologic Environments. *Science* **2015,** *349* (6247), aaa6760-1-8.
18. Legg, B. A.; Zhu, M.; Comolli, L. R.; Gilbert, B.; Banfield, J. F., Impacts of ionic strength on three-dimensional nanoparticle aggregate structure and consequences for environmental transport and deposition. *Environ. Sci. Technol.* **2014,** *48* (23), 13703-13710.
19. Waychunas, G. A.; Kim, C. S.; Banfield, J. F., Nanoparticulate iron oxide minerals in soils and sediments: unique properties and contaminant scavenging mechanisms. *J. Nanopart. Res.* **2005,** *7*, 409-433.
20. Gilbert, B.; Banfield, J., Molecular-Scale Processes Involving Nanoparticulate Minerals in Biogeochemical Systems. *Reviews in Mineralogy and Geochemistry* **2005,** *59* (1), 109-155.
21. Nedel, S.; Dideriksen, K.; Christiansen, B. C.; Bovet, N.; Stipp, S. L. S., Uptake and Release of Cerium During Fe-Oxide Formation and Transformation in Fe(II) Solutions. *Environ. Sci. Technol.* **2010,** *44* (12), 4493-4498.
22. Navrotsky, A.; Mazeina, L.; Majzlan, J., Size-Driven Structural and Thermodynamic Complexity in Iron Oxides. *Science* **2008,** *319* (5870), 1635-1638.
23. Cornell, R. M.; Schwertmann, U., *The Iron Oxides: Structures, Properties, Reactions, Occurrences and Uses*. 2nd ed.; Wiley-VCH: Weinheim, 2003; p 664.
24. Schwartzenbach, R. P.; Gschwend, P. M.; Imboden, D. M., *Environmental Organic Chemistry*. Second Edition ed.; Wiley-Interscience: Hoboken, New Jersey, 2003.
25. Yap, C. L.; Gan, S.; Ng, H. K., Fenton based remediation of polycyclic aromatic hydrocarbons-contaminated soils. *Chemosphere* **2011,** *83* (11), 1414-30.
26. Chun, C. L.; Penn, R. L.; Arnold, W. A., Kinetic and Microscopic Studies of Reductive Transformations of Organic Contaminants on Goethite. *Environ. Sci. Technol.* **2006,** *40* (10), 3299-3304.
27. Banwart, S.; Davies, S.; Stumm, W., The role of oxalate in accelerating the reductive dissolution of hematite (α-Fe2O3) by ascorbate. *Colloids and Surfaces* **1989,** *39* (2), 303-309.
28. Echigo, T.; Aruguete, D. M.; Murayama, M.; Hochella Jr, M. F., Influence of size, morphology, surface structure, and aggregation state on reductive dissolution of hematite nanoparticles with ascorbic acid. *Geochim. Cosmochim. Acta* **2012,** *90* (0), 149-162.
29. Erbs, J.; Gilbert, B.; Penn, R. L., Influence of size on reductive dissolution of six-line ferrihydrite. *J. Phys. Chem. C* **2008,** *112*, 12127–12133.
30. Erbs, J. J.; Berquó, T. S.; Reinsch, B. C.; Lowry, G. V.; Banerjee, S. K.; Penn, R. L., Reductive dissolution of arsenic-bearing ferrihydrite. *Geochim. Cosmochim. Acta* **2010,** *74* (12), 3382-3395.
31. Larsen, O., Postma, Dieke, Kinetics of reductive bulk dissolution of lepidocrocite, ferrihydrite, and goethite *Geochim. Cosmochim. Acta* **2001**, 1367-1379.
32. Gephart, R. E., *Hanford: A conversation about nuclear waste and cleanup*. Battelle Press: Richland, WA, 2003.
33. Rodgers, M. J., Waste Tank Summary Report for Month Ending February 28, 2015. Washington River Protection Solutions, LLC: Richland, WA, 2015; Vol. HNF-EP-0182, Rev. 326.

34. Sigmon, G. E.; Unruh, D. K.; Ling, J.; Weaver, B.; Ward, M.; Pressprich, L.; Simonetti, A.; Burns, P. C., Symmetry versus Minimal Pentagonal Adjacencies in Uranium-Based Polyoxometalate Fullerene Topologies. *Angew. Chem., Int. Ed.* **2009,** *48* (15), 2737-2740.
35. Flynn, S. L.; Szymanowski, J. E. S.; Gao, Y.; Liu, T.; Burns, P. C.; Fein, J. B., Experimental measurements of U60 nanocluster stability in aqueous solution. *Geochim. Cosmochim. Acta* **2015,** *156*, 94-105.
36. Qiu, J.; Burns, P. C., Clusters of actinides with oxide, peroxide, or hydroxide bridges. *Chem. Rev.* **2013,** *113* (2), 1097-120.
37. Sigmon, G. E.; Ling, J.; Unruh, D. K.; Moore-Shay, L.; Ward, M.; Weaver, B.; Burns, P. C., Uranyl-Peroxide Interactions Favor Nanocluster Self-Assembly. *J. Am. Chem. Soc.* **2009,** *131*, 16648-16649.
38. Kistler, M. L.; Bhatt, A.; Liu, G.; Casa, D.; Liu, T., A Complete Macroion-"Blackberry" Assembly-Macroion Transition with Continuously Adjustable Assembly Sizes in {Mo132} Water/Acetone Systems. *J. Am. Chem. Soc.* **2007,** *129*, 6453-6460.
39. Liu, G.; Liu, T.; Mal, S. S.; Kortz, U., Wheel-Shaped Polyoxotungstate $[Cu_{20}Cl(OH)_{24}(H_2O)_{12}(P_8W_{48}O_{184})]^{25-}$ Macroanions Form Supramolecular "Blackberry" Structure in Aqueous Solution. *J. Am. Chem. Soc.* **2006,** *128*, 10103-10110.
40. Gao, Y.; Haso, F.; Szymanowski, J. E. S.; Zhou, J.; Hu, L.; Burns, P. C.; Liu, T., Solution Behavior of Uranyl Peroxide U_{60} Nanoclusters with Interaction of the Hydration Layers of Their Counterions. *In prep* **2015**.
41. Schwertmann, U.; Cornell, R. M., *Iron Oxides in the Laboratory: Preparation and Characterization*. 2nd ed.; Wiley-VCH: Weinheim, 2000.
42. Ostwald, W., Studies on the formation and transformation of solid compounds: Report I. Supersaturation and practicing cooling. *Z. physik. Ch.* **1897,** *22*, 289-330.
43. Ostwald, W., *Lehrbuch der Allgemeinen Chemie*. Engelmann: Leipzig, Germany, 1896; Vol. 2, Part 1.
44. Penn, R. L.; Oskam, G.; Strathmann, T. J.; Searson, P. C.; Stone, A. T.; Veblen, D. R., Epitaxial Assembly in Aged Colloids. *J. Phys. Chem. B* **2001,** *105* (11), 2177-2182.
45. Penn, R. L.; Banfield, J. F., Morphology development and crystal growth in nanocrystalline aggregates under hydrothermal conditions: insights from titania. *Geochim. Cosmochim. Acta* **1999,** *63* (10), 1549-1557.
46. Bailey, J. K.; Brinker, C. J.; Mecartney, M. L., Growth Mechanisms of Iron Oxide Particles of Differing Morphologies from the Forced Hydrolysis of Ferric Chloride Solutions. *J. Colloid Interface Sci.* **1993,** *157* (1), 1-13.
47. Ocaña, M.; Morales, M. P.; Serna, C. J., The Growth Mechanism of α-Fe2O3 Ellipsoidal Particles in Solution. *J. Colloid Interface Sci.* **1995,** *171* (1), 85-91.
48. Penn, R. L.; Erbs, J.; Gulliver, D., Controlled growth of alpha-FeOOH nanorods by exploiting-oriented aggregation. *J. Cryst. Growth* **2006,** *293* (1), 1-4.
49. Penn, R. L.; Tanaka, K.; Erbs, J., Size dependent kinetics of oriented aggregation. *J. Cryst. Growth* **2007,** *309* (1), 97-102.
50. Song, H.; Lee, K.-H.; Jeong, H.; Um, S. H.; Han, G.-S.; Jung, H. S.; Jung, G. Y., A simple self-assembly route to single crystalline SnO_2 nanorod growth by oriented attachment for dye sensitized solar cells. *Nanoscale* **2013,** *5*, 1188-1194.

51. Lee, E. J. H.; Ribeiro, C.; Longo, E.; Leite, E. R., Oriented Attachment: An Effective Mechanism in the Formation of Anisotropic Nanocrystals. *J. Phys. Chem. B* **2005,** *109* (44), 20842-20846.
52. Chiche, D.; Digne, M.; Revel, R.; Chaneac, C.; Jolivet, J. P., Accurate determination of oxide nanoparticle size and shape based on X-ray powder pattern simulation: Application to boehmite AlOOH. *J. Phys. Chem. C* **2008,** *112* (23), 8524-8533.
53. Banfield, J. F.; Welch, S. A.; Zhang, H.; Thomsen Ebert, T.; Lee Penn, R., Aggregation-Based Crystal Growth and Microstructure Development in Natural Iron Oxyhydroxide Biomineralization Products. *Science* **2000,** *289* (5480), 751.
54. Isley, S. L.; Penn, R. L., Titanium dioxide nanoparticles: Effect of sol-gel pH on phase composition, particle size, and particle growth mechanism. *J. Phys. Chem. C* **2008,** *112* (12), 4469-4474.
55. Oskam, G.; Nellore, A.; Penn, R. L.; Searson, P., The growth kinetics of TiO_2 nanoparticles from titanium(IV) alkoxide at high water/titanium ratio. *J. Phys. Chem. B* **2003,** *107* (8), 1734-1738.
56. Li, D.; Soberanis, F.; Fu, J.; Hou, W.; Wu, J.; Kisailus, D., Growth Mechanism of Highly Branched Titanium Dioxide Nanowires via Oriented Attachment. *Cryst. Growth Des.* **2013,** *13* (2), 422-428.
57. Tsai, M. H.; Chen, S. Y.; Shen, P., Imperfect Oriented Attachment: Accretion and Defect Generation of Nanosize Rutile Condensates. *Nano Lett.* **2004,** *4* (7), 1197-1201.
58. Huang, F.; Zhang, H. Z.; Banfield, J., Two-stage crystal-growth kinetics observed during hydrothermal coarsening of nanocrystalline ZnS. *Nano Lett.* **2003,** *3* (3), 373-378.
59. Ethayaraja, M.; Bandyopadhyaya, R., Mechanism and modeling of nanorod formation from nanodots. *Langmuir* **2007,** *23* (11), 6418-6423.
60. Gong, M.; Kirkeminde, A.; Ren, S., Symmetry-defying iron pyrite (FeS_2) nanocrystals through oriented attachment. *Sci Rep* **2013,** *3*, 2092.
61. Li, D.; Nielsen, M. H.; Lee, J. R.; Frandsen, C.; Banfield, J. F.; De Yoreo, J. J., Direction-specific interactions control crystal growth by oriented attachment. *Science* **2012,** *336* (6084), 1014-1018.
62. Huang, Z.; Zhang, G., Biomimetic Synthesis of Aragonite Nanorod Aggregates with Unusual Morphologies Using a Novel Template of Natural Fibrous Proteins at Ambient Condition. *Cryst. Growth Des.* **2012,** *12* (4), 1816-1822.
63. Politi, Y.; Arad, T.; Klein, E.; Weiner, S.; Addadi, L., Sea urchin spine calcite forms via a transient amorphous calcium carbonate phase. *Science* **2004,** *306* (5699), 1161-1164.
64. Killian, C. E.; Metzler, R. A.; Gong, Y. U. T.; Olson, I. C.; Aizenberg, J.; Politi, Y.; Wilt, F. H.; Scholl, A.; Young, A.; Doran, A.; Kunz, M.; Tamura, N.; Coppersmith, S. N.; Gilbert, P. U. P. A., Mechanism of calcite co-orientation in the sea urchin tooth. *J. Am. Chem. Soc.* **2009,** *131*, 18404-18409.
65. Penn, R. L., Kinetics of Oriented Aggregation. *J. Phys. Chem. B* **2004,** *108* (34), 12707-12712.
66. Yuwono, V.; Burrows, N. D.; Soltis, J. A.; Penn, R. L., Oriented Aggregation: Formation and Transformation of Mesocrystal Intermediates Revealed. *J. Am. Chem. Soc.* **2010,** *132*, 2163–2165.

67. Song, R.-Q.; Cölfen, H., Mesocrystals-Ordered Nanoparticle Superstructures. *Adv. Mater.* **2010,** *22* (12), 1301-1330.
68. Niederberger, M.; Colfen, H., Oriented attachment and mesocrystals: Non-classical crystallization mechanisms based on nanoparticle assembly. *Phys. Chem. Chem. Phys.* **2006,** *8* (28), 3271-3287.
69. Cölfen, H.; Antonietti, M., Mesocrystals: Inorganic Superstructures Made by Highly Parallel Crystallization and Controlled Alignment. *Angew. Chem., Int. Ed.* **2005,** *44* (35), 5576-5591.
70. Cölfen, H.; Antonietti, M., *Mesocrystals and Nonclassical Crystallization*. John Wiley & Sons, Ltd: 2008; p 276.
71. Penn, R. L.; others, PMG Workshop Placeholder Ref. **2015**.
72. Ghose, S. K.; Waychunas, G. A.; Trainor, T. P.; Eng, P. J., Hydrated goethite (α-FeOOH) (1 0 0) interface structure: Ordered water and surface functional groups. *Geochim. Cosmochim. Acta* **2010,** *74* (7), 1943-1953.
73. Zheng, H.; Smith, R. K.; Jun, Y. W.; Kisielowski, C.; Dahmen, U.; Alivisatos, A. P., Observation of single colloidal platinum nanocrystal growth trajectories. *Science* **2009,** *324* (5932), 1309-1312.
74. Penn, R. L.; Soltis, J. A., Characterizing crystal growth by oriented aggregation. *CrystEngComm* **2014,** *16* (8), 1409-1418.
75. Sabyrov, K.; Penn, R. L., A kinetic model for two-step phase transformation of hydrothermally treated nanocrystalline anatase. *In prep* **2015**.
76. Wang, L.; Gao, L., Morphology Transformation of Hematite Nanoparticles Through Oriented Aggregation. *J. Am. Ceram. Soc.* **2008,** *91* (10), 3391-3395.
77. An, Z.; Zhang, J.; Pan, S.; Song, G., Novel peanut-like α-Fe2O3 superstructures: Oriented aggregation and Ostwald ripening in a one-pot solvothermal process. *Powder Technol.* **2012,** *217*, 274-280.
78. Jia, B.; Gao, L., Growth of well-defined cubic hematite single crystals: oriented aggregation and Ostwald ripening. *Cryst. Growth Des.* **2008,** *8*, 1372-1376.
79. Frandsen, C.; Legg, B. A.; Comolli, L. R.; Zhang, H.; Gilbert, B.; Johnson, E.; Banfield, J. F., Aggregation-induced growth and transformation of β-FeOOH nanorods to micron-sized α-Fe2O3 spindles. *CrystEngComm* **2014,** *16*, 1451–1458.
80. Fang, J.; Ding, B.; Gleiter, H., Mesocrystals: Syntheses in metals and applications. *Chem. Soc. Rev.* **2011,** *40* (11), 5347-5360.
81. Zhang, Q.; Liu, S.; Yu, S., Recent advances in oriented attachment growth and synthesis of functional materials: concept, evidence, mechanism, and future. *J. Mater. Chem.* **2009,** *19* (2), 191-207.
82. Zhang, J.; Huang, F.; Lin, Z., Progress of nanocrystalline growth kinetics based on oriented attachment. *Nanoscale* **2010,** *2* (1), 18-34.
83. Lu, Z.; Yin, Y., Colloidal nanoparticle clusters: functional materials by design. *Chem. Soc. Rev.* **2012,** *41* (21), 6874-6887.
84. Fischer, W. R.; Schwertmann, U., The Formation of Hematite from Amorphous Iron(III) Hydroxide. *Clays Clay Miner.* **1975,** *23*, 33-37.
85. Burleson, D. J.; Penn, R. L., Two-Step Growth of Goethite from Ferrihydrite. *Langmuir* **2006,** *22* (1), 402-409.
86. Burrows, N. D.; Hale, C. R. H.; Penn, R. L., Effect of pH on the Kinetics of Crystal Growth by Oriented Aggregation. *Cryst. Growth Des.* **2013,** *13* (8), 3396-3403.

87. Burrows, N. D.; Hale, C. R. H.; Penn, R. L., Effect of Ionic Strength on the Kinetics of Crystal Growth by Oriented Aggregation. *Cryst. Growth Des.* **2012,** *12* (10), 4787-4797.
88. Schwertmann, U.; Murad, E., Effect of pH on the formation of goethite and hematite from ferrihydrite. *Clays Clay Miner.* **1983,** *31* (4), 277-284.
89. Shaw, S.; Pepper, S. E.; Bryan, N. D.; Livens, F. R., The kinetics and mechanisms of goethite and hematite crystallization under alkaline conditions, and in the presence of phosphate. *Am. Mineral.* **2005,** *90*, 1852-1860.
90. Cornell, R. M.; Schneider, W.; Giovanoli, R., Phase transformations in the ferrihydrite/cysteine system. *Polyhedron* **1989,** *8* (23), 2829-2836.
91. Chen, J. S.; Zhu, T.; Li, C. M.; Lou, X. W., Building hematite nanostructures by oriented attachment. *Angew Chem Int Ed Engl* **2011,** *50* (3), 650-653.
92. Feitknecht, W.; Michaelis, W., Hydrolysis of iron(III) perchlorate solutions. *Helvetica Chimica Acta* **1962,** *45*, 212-24.
93. Kozin, P. A.; Salazar-Alvarez, G.; Boily, J.-F., Oriented Aggregation of Lepidocrocite and Impact on Surface Charge Development. *Langmuir* **2014,** *30*, 9017-9021.
94. Hockridge, J. G.; Jones, F.; Loan, M.; Richmond, W. R., An electron microscopy study of the crystal growth of schwertmannite needles through oriented aggregation of goethite nanocrystals. *J. Cryst. Growth* **2009,** *311* (15), 3876-3882.
95. Zhang, H.; Banfield, J. F., New kinetic model for the nanocrystalline anatase-to-rutile transformation revealing rate dependence on number of particles. *Am. Mineral.* **1999,** *84*, 528-535.
96. Zhang, H.; Penn, R. L.; Hamers, R. J.; Banfield, J. F., Enhanced Adsorption of Molecules on Surfaces of Nanocrystalline Particles. *J. Phys. Chem. B* **1999,** *103*, 4656-4662.
97. Zhang, H.; Banfield, J. F., Kinetics of Crystallization and Crystal Growth of Nanocrystalline Anatase in Nanometer-Sized Amorphous Titania. *Chemistry of Materials* **2002,** *14* (10), 4145-4154.
98. Zhang, H.; Banfield, J. F., Phase transformation of nanocrystalline anatase-to-rutile via combined interface and surface nucleation. *Journal of Materials Research* **2000,** *15* (02), 437-448.
99. Sabyrov, K.; Lee Penn, R., Interface-mediated phase transformation in nanocrystalline particles: the case of the TiO2 allotropes. *CrystEngComm* **2015,** *17* (10), 2062-2069.
100. Sabyrov, K.; Adamson, V.; Penn, R. L., Two-step phase transformation of anatase to rutile in aqueous suspension. *CrystEngComm* **2014,** *16* (8), 1488.
101. Sabyrov, K.; Burrows, N. D.; Penn, R. L., Size-Dependent Anatase to Rutile Phase Transformation and Particle Growth. *Chemistry of Materials* **2013,** *25* (8), 1408-1415.
102. Kumar, S.; Wang, Z.; Penn, R. L.; Tsapatsis, M., A Structural Resolution Cryo-TEM Study of the Early Stages of MFI Growth. *J. Am. Chem. Soc.* **2008,** *130* (51), 17284-17286.
103. Grogan, J. M.; Schneider, N. M.; Ross, F. M.; Bau, H. H., The nanoaquarium: a new paradigm in electron microscopy. *Journal of the Indian Institute of Science* **2012,** *92*, 295-308.

104. Yuk, J. M.; Park, J.; Ercius, P.; Kim, K.; Hellebusch, D. J.; Crommie, M. F.; Lee, J. Y.; Zettl, A.; Alivisatos, A. P., High-resolution EM of colloidal nanocrystal growth using graphene liquid cells. *Science* **2012,** *336* (6077), 61-64.
105. Cao, G., *Nanostructures and Nanomaterials: Synthesis, Properties and Applications*. Imperial College Press: London, 2004.
106. Woehl, T. J.; Browning, N. D.; Evans, J. E.; Arslan, I.; Ristenpart, W. D.; Park, C., Direct observation of aggregative nanoparticle growth: Kinetic modeling of the size distribution and growth rate. *Nano Lett.* **2013,** *14* (1), 373-378.
107. Zhan, H.; Yang, X.; Wang, C.; Liang, C.; Wu, M., Multiple Growth Stages and Their Kinetic Models of Anatase Nanoparticles under Hydrothermal Conditions. *J. Phys. Chem. C* **2010,** *114* (34), 14461-14466.
108. Lupulescu, A. I.; Rimer, J. D., In Situ Imaging of Silicalite-1 Surface Growth Reveals the Mechanism of Crystallization. *Science* **2014,** *344* (6185), 729-732.
109. Burrows, N. D.; Penn, R. L., Cryogenic Transmission Electron Microscopy: Aqueous Suspensions of Nanoscale Objects. *Microscopy and Microanalysis* **2013,** *19* (6), 1542-1553.
110. Jungjohann, K. L.; Evans, J. E.; Aguiar, J. A.; Arslan, I.; Browning, N. D., Atomic-scale imaging and spectroscopy for in situ liquid scanning transmission electron microscopy. *Microscopy and Microanalysis* **2012,** *18* (3), 621-627.
111. Liu, Y.; Lin, X. M.; Sun, Y.; Rajh, T., In situ visualization of self-assembly of charged gold nanoparticles. *J. Am. Chem. Soc.* **2013,** *135* (10), 3764-3767.
112. Pan, Y.; Brown, A.; Brydson, R.; Warley, A.; Li, A.; Powell, J., Electron beam damage studies of synthetic 6-line ferrihydrite and ferritin molecule cores within a human liver biopsy. *Micron* **2006,** *37* (5), 403-11.
113. Hapiuk, D.; Masenelli, B.; Masenelli-Varlot, K.; Tainoff, D.; Boisron, O.; Albin, C.; Mélinon, P., Oriented Attachment of ZnO Nanocrystals. *J. Phys. Chem. C* **2013,** *117* (19), 10220-10227.
114. Davis, T. M.; Drews, T. O.; Ramanan, H.; He, C.; Dong, J. S.; Schnablegger, H.; Katsoulakis, M.; Kokkoli, E.; McCormick, A.; Penn, R. L.; Tsapatsis, M., Mechanistic principles of nanoparticle evolution to zeolite crystals. *Nat. Mater.* **2006,** *5* (5), 400-408.
115. Drews, T. O.; Tsapatsis, M., Model of the evolution of nanoparticles to crystals via an aggregative growth mechanism. *Micropor. Mesopor. Mat.* **2007,** *101* (1-2), 97-107.
116. Schwahn, D.; Ma, Y.; Cölfen, H., Mesocrystal to Single Crystal Transformation of d,l-Alanine Evidenced by Small Angle Neutron Scattering. *J. Phys. Chem. C* **2007,** *111* (8), 3224-3227.
117. Mintova, S.; Olson, N. H.; Senker, J.; Bein, T., Mechanism of the transformation of silica precursor solutions into Si-MFI zeolite. *Angew. Chem., Int. Ed.* **2002,** *41* (14), 2558-2561.
118. Schliehe, C.; Juarez, B. H.; Pelletier, M.; Jander, S.; Greshnykh, D.; Nagel, M.; Meyer, A.; Foerster, S.; Kornowski, A.; Klinke, C.; Weller, H., Ultrathin PbS sheets by two-dimensional oriented attachment. *Science* **2010,** *329*, 550-3.
119. Burrows, N. D.; Yuwono, V. M.; Penn, R. L., Quantifying the kinetics of crystal growth by oriented aggregation. *MRS Bull.* **2010,** *35*, 133-137.

120. Ribeiro, C.; Lee, E.; Longo, E.; Leite, E. R., Oriented attachment mechanism in anisotropic nanocrystals: A "polymerization" approach. *ChemPhysChem* **2006,** *7* (3), 664-670.
121. Kallay, N.; Žalac, S., Stability of Nanodispersions: A Model for Kinetics of Aggregation of Nanoparticles. *J. Colloid Interface Sci.* **2002,** *253* (1), 70-76.
122. Dalmaschio, C. J.; Ribeiro, C.; Leite, E. R., Impact of the colloidal state on the oriented attachment growth mechanism. *Nanoscale* **2010,** *2* (11), 2336-2345.
123. Qin, Y.; Fichthorn, K. A., Solvation forces between colloidal nanoparticles: Directed alignment. *Physical Review E* **2006,** *73* (2), 020401.
124. Zhang, W.; Crittenden, J.; Li, K.; Chen, Y., Attachment Efficiency of Nanoparticle Aggregation in Aqueous Dispersions: Modeling and Experimental Validation. *Environ. Sci. Technol.* **2012,** *46* (13), 7054-7062.
125. von Smoluchowski, M., Mathematical theory of the kinetics of the coagulation of colloidal solutions. *Z. physik. Chem.* **1917,** *92*, 129-68.
126. Spagnoli, D.; Banfield, J. F.; Parker, S. C., Free Energy Change of Aggregation of Nanoparticles. *J. Phys. Chem. C* **2008,** *112* (38), 14731-14736.
127. Ribeiro, C.; Lee, E.; Longo, E.; Leite, E. R., A kinetic model to describe nanocrystal growth by the oriented attachment mechanism. *ChemPhysChem* **2005,** *6* (4), 690-696.
128. Peng, X.; Wickham, J.; Alivisatos, A. P., Kinetics of II-VI and III-V Colloidal Semiconductor Nanocrystal Growth: "Focusing" of Size Distributions. *J. Am. Chem. Soc.* **1998,** *120*, 5343-5344.
129. Ratkovich, A. S.; Penn, R. L., Controlling nanosized ZnO growth kinetics using various Zn : OH concentration ratios. *J. Phys. Chem. C* **2007,** *111* (38), 14098-14104.
130. Drews, T. O.; Katsoulakis, M. A.; Tsapatsis, M., A Mathematical Model for Crystal Growth by Aggregation of Precursor Metastable Nanoparticles. *J. Phys. Chem. B* **2005,** *109*, 23879-23887.
131. Chalmers, W., *J. Am. Chem. Soc.* **1934,** *56*, 912-922.
132. Flory, P. J., *J. Am. Chem. Soc.* **1936,** *58*, 1877-1885.
133. Lee, E. J. H.; Ribeiro, C.; Longo, E.; Leite, E. R., Growth kinetics of tin oxide nanocrystals in colloidal suspensions under hydrothermal conditions. *Chem. Phys.* **2006,** *328* (1-3), 229-235.
134. Jun, Y. W.; Casula, M. F.; Sim, J. H.; Kim, S. Y.; Cheon, J.; Alivisatos, A. P., *J. Am. Chem. Soc.* **2003,** *125*, 15981-15986.
135. Soltis, J. A.; Harapan, J.; Penn, R. L., Heterogeneous phase transformation in iron oxides. *In prep* **2015**.
136. Zhang, H.; Banfield, J. F., Energy Calculations Predict Nanoparticle Attachment Orientations and Asymmetric Crystal Formation. *Journal of Physical Chemistry Letters* **2012,** *3* (19), 2882-2886.
137. Meldrum, F. C.; Cölfen, H., Controlling mineral morphologies and structures in biological and synthetic systems. *Chem. Rev.* **2008,** *108*, 4332–4432.
138. Wulff, G., *Z. Kristallogr. Mineral.* **1901,** *34*, 449-530.
139. Alimohammadi, M.; Fichthorn, K. A., Molecular Dynamics Simulation of the Aggregation of Titanium Dioxide Nanocrystals: Preferential Alignment. *Nano Lett.* **2009,** *9* (12), 4198-4203.

140. Xia, Y.; Xiong, Y.; Lim, B.; Skrabalak, S. E., Shape-controlled synthesis of metal nanocrystals: simple chemistry meets complex physics? *Angew Chem Int Ed Engl* **2009,** *48* (1), 60-103.
141. Navrotsky, A., Nanoscale effects on thermodynamics and phase equilibria in oxide systems. *ChemPhysChem* **2011,** *12* (12), 2207-15.
142. Raju, M.; van Duin, A. C.; Fichthorn, K. A., Mechanisms of oriented attachment of TiO_2 nanocrystals in vacuum and humid environments: reactive molecular dynamics. *Nano Lett.* **2014,** *14* (4), 1836-42.
143. Maram, P. S.; Costa, G. C. C.; Navrotsky, A., Experimental Confirmation of Low Surface Energy in $LiCoO_2$ and Implications for Lithium Battery Electrodes. *Angew. Chem., Int. Ed.* **2013,** *52* (46), 12139-12142.
144. Cölfen, H.; Mann, S., Higher-Order Organization by Mesoscale Self-Assembly and Transformation of Hybrid Nanostructures. *Angew. Chem., Int. Ed.* **2003,** *42* (21), 2350-2365.
145. Burrows, N. D.; Kesselman, E.; Sabyrov, K.; Stemig, A.; Talmon, Y.; Penn, R. L., Crystalline nanoparticle aggregation in non-aqueous solvents. *CrystEngComm* **2014,** *16*, 1472-1481.
146. Chen, C.; Hu, R.; Mai, K.; Ren, Z.; Wang, H.; Qian, G.; Wang, Z., Shape Evolution of Highly Crystalline Anatase TiO2 Nanobipyramids. *Cryst. Growth Des.* **2011,** *11* (12), 5221-5226.
147. Derjaguin, B.; Landau, L., Theory of stability of highly charged liophobic sols and adhesion of highly charged particles in solutions of electrolytes. *Zhurnal Eksperimentalnoi Teor. Fiz.* **1941,** *15*, 663-682.
148. Verwey, E. J. W.; Overbeek, J. T. G.; Nes, K. v., *Theory of the stability of lyophobic colloids: The interaction of sol particles having an electric double layer*. Elsevier Pub. Co.: New York, 1948.
149. Israelachvili, J. N., *Intermolecular and Surface Forces (Third Edition)*. Academic Press: San Diego, 2011; p 704.
150. Coulomb, C.-A. d., Second mémoire sur l'électricité et le magnétisme. In *Histoire de l'Académie Royale des Sciences*, 1785; pp 578-611.
151. Coulomb, C.-A. d., Premier mémoire sur l'électricité et le magnétisme. In *Histoire de l'Académie Royale des Sciences*, 1785; pp 569-577.
152. Snook, I.; van Megen, W., Structure of dense liquids at solid interfaces. *Journal of Chemical Physics* **1979,** *70* (6), 3099-3105.
153. Abraham, F. F., The interfacial density profile of a Lennard-Jones fluid in contact with a (100) Lennard-Jones wall and its relationship to idealized fluid/wall systems: A Monte Carlo simulation. *Journal of Chemical Physics* **1978,** *68* (8), 3713-3716.
154. Cheng, L.; Fenter, P.; Nagy, K.; Schlegel, M.; Sturchio, N., Molecular-Scale Density Oscillations in Water Adjacent to a Mica Surface. *Phys. Rev. Lett.* **2001,** *87* (15), 156103-1-156103-4.
155. Lovley, D. R., Microbial Fe(III) reduction in subsurface environments. *FEMS Microbiology Reviews* **1997,** *20* (3-4), 305-313.
156. Nealson, K. H.; Myers, C. R., Microbial reduction of manganese and iron: new approaches to carbon cycling. *Appl. Environ. Microbiol.* **1992,** *58*, 439-43.

157. DiChristina, T. J.; Fredrickson, J. K.; Zachara, J. M., Enzymology of electron transport: Energy generation with geochemical consequences. *Rev. Mineral. Geochem.* **2005,** *59*, 27-52.
158. Fortin, D.; Langley, S., Formation and occurrence of biogenic iron-rich minerals. *Earth-Science Reviews* **2005,** *72* (1–2), 1-19.
159. Ford, R. G.; Bertsch, P. M.; Farley, K. J., Changes in Transition and Heavy Metal Partitioning during Hydrous Iron Oxide Aging. *Environ. Sci. Technol.* **1997,** *31* (7), 2028-2033.
160. Cwiertny, D. M.; Handler, R. M.; Schaefer, M. V.; Grassian, V. H.; Scherer, M. M., Interpreting nanoscale size-effects in aggregated Fe-oxide suspensions: Reaction of Fe(II) with Goethite. *Geochim. Cosmochim. Acta* **2008,** *72* (5), 1365-1380.
161. Jambor, J. L.; Dutrizac, J. E., Occurrence and Constitution of Natural and Synthetic Ferrihydrite, a Widespread Iron Oxyhydroxide. *Chem. Rev.* **1998,** *98* (7), 2549-2586.
162. Vikesland, P. J.; Valentine, R. L., Iron Oxide Surface-Catalyzed Oxidation of Ferrous Iron by Monochloramine: Implications of Oxide Type and Carbonate on Reactivity. *Environ. Sci. Technol.* **2002,** *36* (3), 512-519.
163. Schwertmann, U., Solubility and dissolution of iron oxides. *Plant and Soil* **1991,** *130* (1), 1-25.
164. Towe, K. M.; Bradley, W. F., Mineralogical constitution of colloidal "hydrous ferric oxides". *J. Colloid Interface Sci.* **1967,** *24* (3), 384-392.
165. Michel, F. M.; Ehm, L.; Antao, S. M.; Lee, P. L.; Chupas, P. J.; Liu, G.; Strongin, D. R.; Schoonen, M. A. A.; Phillips, B. L.; Parise, J. B., The Structure of Ferrihydrite, a Nanocrystalline Material. *Science* **2007,** *316* (5832), 1726-1729.
166. Michel, F. M.; Barron, V.; Torrent, J.; Morales, M. P.; Serna, C. J.; Boily, J. F.; Liu, Q.; Ambrosini, A.; Cismasu, A. C.; Brown, G. E., Ordered ferrimagnetic form of ferrihydrite reveals links among structure, composition, and magnetism. *Proc. Natl. Acad. Sci.* **2010,** *107* (7), 2787-2792.
167. Manceau, A., Evaluation of the structural model for ferrihydrite derived from real-space modelling of high-energy X-ray diffraction data. *Clay Minerals* **2009,** *44*, 19-34.
168. Manceau, A., PDF analysis of ferrihydrite and the violation of Pauling's Principia. *Clay Minerals* **2010,** *45*, 225-228.
169. Rancourt, D. G.; Meunier, J. F., Constraints on structural models of ferrihydrite as a nanocrystalline material. *Am. Mineral.* **2008,** *93* (8-9), 1412-1417.
170. Janney, D. E.; Cowley, J. M.; Buseck, P. R., Transmission electron microscopy of synthetic 2- and 6-line ferrihydrite. *Clays Clay Miner.* **2000,** *48* (1), 111-119.
171. Janney, D. E.; Cowley, J. M.; Buseck, P. R., Structure of synthetic 2-line ferrihydrite by electron nanodiffraction. *Am. Mineral.* **2000,** *85* (9), 1180-1187.
172. Jansen, E.; Kyek, A.; Schäfer, W.; Schwertmann, U., The structure of six-line ferrihydrite. *Applied Physics A: Materials Science and Processing* **2002,** *74* (SUPPL.II), S1004-S1006.
173. Figueiredo, M. O.; Silva, T. P.; Veiga, J. P., Natural nanomaterials: reappraising the elusive structure of the nano-sized mineral ferrihydrite through X-ray absorption spectroscopy at the iron K-edge. *Materials Science Forum* **2013**, 931-935.

174. Soltis, J. A.; Penn, R. L., Oriented attachment and non-classical formation in iron oxides. In *Iron Oxides*, Faivre, D., Ed. Wiley VCH: 2015.
175. Nespolo, M.; Ferraris, G., The oriented attachment mechanism in the formation of twins – a survey. *Eur. J. Mineral.* **2004,** *16* (3), 401-406.
176. Zeng, H. C., Oriented attachment: a versatile approach for construction of nanomaterials. *Int. J. Nanotechnol.* **2007,** *4* (4), 329-346.
177. Zhang, H.; Penn, R. L.; Lin, Z.; Cölfen, H., Nanocrystal growth via oriented attachment. *CrystEngComm* **2014,** *16* (8), 1407.
178. Park, J.-I.; Jun, Y.-w.; Choi, J.-s.; Cheon, J., Highly crystalline anisotropic superstructures via magnetic field induced nanoparticle assembly. *Chem. Commun.* **2007,** (47), 5001-5003.
179. Baynton, A.; Radomirovic, T.; Ogden, M. I.; Raston, C. L.; Richmonda, W. R.; Jones, F., Small molecules induce mesocrystal formation: nanoparticle aggregation directed by self-assembling calixarenes. *CrystEngComm* **2011,** *13*, 10-112.
180. Liu, Z.; Wen, X. D.; Wu, X. L.; Gao, Y. J.; Chen, H. T.; Zhu, J.; Chu, P. K., Intrinsic Dipole-Field-Driven Mesoscale Crystallization of Core−Shell ZnO Mesocrystal Microspheres. *J. Am. Chem. Soc.* **2009,** *131* (26), 9405-9412.
181. Fang, X.-L.; Chen, C.; Jin, M.-S.; Kuang, Q.; Xie, Z.-X.; Xie, S.-Y.; Huang, R.-B.; Zheng, L.-S., Single-crystal-like hematite colloidal nanocrystal clusters: synthesis and applications in gas sensors, photocatalysis and water treatment. *J. Mater. Chem.* **2009,** *19* (34), 6154.
182. Sabyrov, K.; Penn, R. L., Interface-mediated phase transformation in nanocrystalline particles: the case of the TiO2 allotropes. *CrystEngComm* **2015**.
183. Das, S.; Hendry, M. J.; Essilfie-Dughan, J., Transformation of Two-Line Ferrihydrite to Goethite and Hematite as a Function of pH and Temperature. *Environ. Sci. Technol.* **2010,** *45* (1), 268-275.
184. Ray, J. R.; Wan, W.; Gilbert, B., Effects of Formation Conditions on the Physicochemical Properties, Aggregation, and Phase Transformation of Iron Oxide Nanoparticles. *Langmuir* **2013**, 1069-1076.
185. Vu, H. P.; Shaw, S.; Benning, L. G., Transformation of ferrihydrite to hematite: an in situ investigation on the kinetics and mechanisms. *Mineral. Mag.* **2008,** *72*, 217-220.
186. Cornell, R. M.; Giovanoli, R., Effect of solution conditions on the proportion and morphology of goethite formed from ferrihydrite. *Clays Clay Miner.* **1985,** *33*, 424-32.
187. Cornell, R. M., Effect of simple sugars on the alkaline transformation of ferrihydrite into goethite and hematite. *Clays Clay Miner.* **1985,** *33* (3), 219-227.
188. Cornell, R. M.; Schwertmann, U., Influence of organic anions on the crystallization of ferrihydrite. *Clays Clay Miner.* **1979,** *27* (6), 402-410.
189. Navrotsky, A., Energetics of oxide nanoparticles. *International Journal of Quantum Chemistry* **2009,** *109* (12), 2647-2657.
190. Bilardello, D.; Jackson, M., What do the Mumpsies do? *IRM Quarterly* **Fall 2013,** *23* (3).
191. Bowles, J.; Jackson, M.; Banerjee, S. K., Interpretation of Low-Temperature Data Part II: The Hematite Morin Transition. *IRM Quarterly* **Spring 2010,** *20* (1).
192. Özdemir, Ö.; Dunlop, D. J.; Berquó, T. S., Morin transition in hematite: Size dependence and thermal hysteresis. *Geochem. Geophys. Geosys.* **2008,** *9*, Q10Z01.

193. Feinberg, J. M.; Solheid, P. A.; Swanson-Hysell, N. L.; Jackson, M. J.; Bowles, J. A., Full vector low-temperature magnetic measurements of geologic materials. *Geochem. Geophys. Geosyst.* **2015,** *16*, 301-314.
194. Scherrer, P., *Nachrichten von der Gesellschaft der Wissenschaften zu Göttingen, mathematisch-physikalische Klasse* **1918,** *2*, 96.
195. Hammersley, A. P., FIT2D: An Introduction and Overview. **1997**.
196. Burt, R., *Soil Survey Laboratory Methods Manual*. 4th ed. ed.; United States Department of Agriculture Natural Resources Conservation Service: 2004; Vol. No. 42.
197. Schwertmann, U., Use of Oxalate for Fe Extraction from Soils. *Can. J. Soil Sci.* **1973,** *53* (2), 244-246.
198. Dominik, P.; Kaupenjohann, M., Simple spectrophotometric determination of Fe in oxalate and HCl soil extracts. *Talanta* **2000,** *51* (4), 701-707.
199. Rasband, W. S. *ImageJ*, U. S. National Institutes of Health: Bethesda, Maryland, USA, 1997-2015.
200. Guyodo, Y.; Banerjee, S.; Leepenn, R.; Burleson, D.; Berquo, T.; Seda, T.; Solheid, P., Magnetic properties of synthetic six-line ferrihydrite nanoparticles. *Phys. Earth Planet. Inter.* **2006,** *154* (3-4), 222-233.
201. Berquó, T. S.; Erbs, J. J.; Lindquist, A.; Penn, R. L.; Banerjee, S. K., Effects of magnetic interactions in antiferromagnetic ferrihydrite particles. *J. Phys.: Condens. Matter* **2009,** *21* (17), 176005.
202. Bhattacharjee, A.; Rooj, A.; Roy, M.; Kusz, J.; Gütlich, P., Solventless synthesis of hematite nanoparticles using ferrocene. *J Mater Sci* **2013,** *48* (7), 2961-2968.
203. Li, D.; Nielsen, M. H.; Lee, J. R.; Frandsen, C.; Banfield, J. F.; De Yoreo, J. J., Direction-specific interactions control crystal growth by oriented attachment--SI. *Science* **2012,** *336* (6084), 1014-8.
204. Raven, K. P., Jain, Amita, Arsenite and Arsenate Adsorption on Ferrihydrite: Kinetics, Equilibrium, and Adsorption Envelopes. *Environmental Science Technology* **1998**, 344-349.
205. Tabara, K.; Higuchi, T.; Yamamoto, K., Cement admixture and cement composition. *PCT Int. Appl.* **2011**.
206. Kim, K.; Yang, S., New fabrication of mixed oxygen carrier for CLC: Sludge and scale from power plant. *Fuel* **2013**, 496-504.
207. He Y, Z. L., Zhu D, Design of multifunctional magnetic iron oxide nanoparticles/mitoxantrone-loaded liposomes for both magnetic resonance imaging and targeted cancer therapy. *International Journal of Nanomedicine* **2014**, 4055-4066.
208. Mo Dan, Y. B., Thomas A. Pittman, Alternating Magnetic Field-Induced Hyperthermia Increases Iron Oxide Nanoparticle Cell Association/Uptake and Flux in Blood-Brain Barrier Models. *Pharmaceutical Research* **2014**.
209. Park, J. W., Ku, Sook Hee, Cross-linked Iron Oxide Nanoparticles for Therapeutic Engineering and in Vivo Monitoring of Mesenchymal Stem Cells in Cerebral Ischemia Model *Macromolecular Bioscience* **2013**, 380-389.
210. Blodau, C.; Gatzek, C., Chemical controls on iron reduction in schwertmannite-rich sediments. *Chemical Geology* **2006,** *235* (3-4), 366-376.
211. Mielke, R. E.; Pace, D. L.; Porter, T.; Southam, G., A critical stage in the formation of acid mine drainage: Colonization of pyrite by Acidithiobacillus ferrooxidans under pH-neutral conditions. *Geobiology* **2003,** *1* (1), 81-90.

212. Brown, G. E.; Henrich, V. E.; Casey, W. H.; Clark, D. L.; Eggleston, C.; Felmy, A.; Goodman, D. W.; Grätzel, M.; Maciel, G.; McCarthy, M. I.; Nealson, K. H.; Sverjensky, D. A.; Toney, M. F.; Zachara, J. M., Metal Oxide Surfaces and Their Interactions with Aqueous Solutions and Microbial Organisms. *Chem. Rev.* **1998,** *99* (1), 77-174.
213. Blodau, C., A review of acidity generation and consumption in acidic coal mine lakes and their watersheds. *Sci. Total Environ.* **2006,** *369* (1–3), 307-332.
214. Cornell, R. M.; Schneider, W.; Giovanoli, R., Phase transformations in the ferrihydrite/cysteine system. *Elsevier: Polyhedron* **1989**, 2829-2836.
215. Manceau, A.; Skanthakumar, S.; Soderholm, L., PDF analysis of ferrihydrite: Critical assessment of the under-constrained akdalaite model. *Am. Mineral.* **2014,** *99* (1), 102-108.
216. Gilbert, B.; Erbs, J. J.; Penn, R. L.; Petkov, V.; Spagnoli, D.; Waychunas, G. A., A disordered nanoparticle model for 6-line ferrihydrite. *Am. Mineral.* **2013,** *98* (8-9), 1465-1476.
217. Xu, W.; Hausner, D. B.; Harrington, R.; Lee, P. L.; Strongin, D. R.; Parise, J. B., Structural water in ferrihydrite and constraints this provides on possible structure models. *Am. Mineral.* **2011,** *96* (4), 513-520.
218. Manceau, A., Critical evaluation of the revised akdalaite model for ferrihydrite. *Am. Mineral.* **2011,** *96*, 521-533.
219. Harrington, R.; Hausner, D. B.; Xu, W.; Bhandari, N.; Michel, F. M.; Brown, G. E., Jr.; Strongin, D. R.; Parise, J. B., Neutron pair distribution function study of two-line ferrihydrite. *Environ. Sci. Technol.* **2011,** *45* (23), 9883-90.
220. Cismasu, A. C.; Michel, F. M.; Tcaciuc, A. P.; Tyliszczak, T.; Brown, J. G. E., Composition and structural aspects of naturally occurring ferrihydrite. *C. R. Geosci.* **2011,** *343* (2-3), 210-218.
221. Penn, R. L., CHEMISTRY: Resolving an Elusive Structure. *Science* **2007,** *316* (5832), 1704-1705.
222. Drits, V. A.; Sakharov, B. A.; Salyn, A. L.; Manceau, A., Structural model for ferrihydrite. *Clay Miner.* **1993,** *28*, 185-207.
223. Majzlan, J.; Navrotsky, A.; Schwertmann, U., Thermodynamics of iron oxides: Part III. Enthalpies of formation and stability of ferrihydrite (~Fe(OH)3), schwertmannite (~FeO(OH)3/4(SO4)1/8), and ε-Fe2O3 1. *Geochim. Cosmochim. Acta* **2004,** *68* (5), 1049-1059.
224. Cherepy, N. J.; Liston, D. B.; Lovejoy, J. A.; Deng, H.; Zhang, J. Z., Ultrafast Studies of Photoexcited Electron Dynamics in γ- and α-Fe2O3 Semiconductor Nanoparticles. *J. Phys. Chem. B* **1998,** *102* (5), 770-776.
225. Farvid, S. S.; Radovanovic, P. V., Phase Transformation of Colloidal In2O3 Nanocrystals Driven by the Interface Nucleation Mechanism: A Kinetic Study. *J. Am. Chem. Soc.* **2012,** *134* (16), 7015-7024.
226. Banfield, J.; Bischoff, B. L.; Anderson, M. A., TiO2 accessory minerals: coarsening, and transformation kinetics in pure and doped synthetic nanocrystalline materials. *Chem. Geology* **1993**, 211-231.
227. Zhang, H.; Banfield, J., Thermodynamic analysis of phase stability of nanocrystalline titania. *J. Mater. Chem* **1998**, 2073-2076.

228. Gilbert, B.; Zhang, H.; Huang, F.; Finnegan, M. P.; Waychunas, G. A.; Banfield, J. F., Special phase transformation and crystal growth pathways observed in nanoparticles. *Geochem. Trans.* **2003,** *4* (4), 20.
229. Na, B.; Guo, M.; Yang, J.; Tan, H.; Zhang, Q.; Fu, Q., Crystal morphology and transcrystallization mechanism of isotactic polypropylene induced by fibres: interface nucleation versus bulk nucleation. *Polymer International* **2006,** *55* (4), 441-448.
230. Wacaser, B. A.; Dick, K. A.; Johansson, J.; Borgström, M. T.; Deppert, K.; Samuelson, L., Preferential Interface Nucleation: An Expansion of the VLS Growth Mechanism for Nanowires. *Adv. Mater.* **2009,** *21* (2), 153-165.
231. Alvarez, M.; Sileo, E. E.; Rueda, E. H., Effect of Mn(II) incorporation on the transformation of ferrihydrite to goethite. *Chemical Geology* **2005,** *216* (1–2), 89-97.
232. Ebinger, M. H.; Schulze, D. G., The Influence of pH on the Synthesis of Mixed Fe-Mn Oxide Minerals. *Clay Minerals* **1990,** *25* (4), 507-518.
233. Mazeina, L.; Navrotsky, A., Surface Enthalpy of Goethite. *Clays Clay Miner.* **2005,** *53* (2), 113-122.
234. Heald, E. F.; Weiss, C. W., Kinetics and mechanism of the anatase/rutile transformation, as catalyzed by ferric oxide and reducing conditions. *Am. Mineral.* **1972,** *57*, 10-23.
235. Shannon, R. D.; Pask, J. A., Kinetics of the Anatase-Rutile Transformation. *J. Am. Ceram. Soc.* **1965,** *48* (8), 391-398.
236. Hochella, M. F.; Lower, S. K.; Maurice, P. A.; Penn, R. L.; Sahai, N.; Sparks, D. L.; Twining, B. S., Nanominerals, Mineral Nanoparticles, and Earth Systems. *Science* **2008,** *319* (5870), 1631-1635.
237. Stumm, W.; Sulzberger, B., *Geochim. Cosmochim. Acta* **1992,** *56*, 3233
238. Casiot, C.; Lebrun, S.; Morin, G.; Bruneel, O.; Personne, J. C.; Elbaz-Poulichet, F., *Sci. Total. Environ.* **2005,** *347*, 122.
239. Jessen, S.; Larsen, F.; Koch, C. B.; Arvin, E., *Environ Sci Technol* **2005,** *39*, 8045.
240. Shaw, J. N., *Commun. Soil Sci. Plant Anal.* **2001,** *32*, 49.
241. Rancourt, D. G.; Fortin, D.; Pichler, T.; Thibault, P.-J.; Lamarche, G.; Morris, R. V.; Mercier, P. H. J., Mineralogy of a natural As-rich hydrous ferric oxide coprecipitate formed by mixing of hydrothermal fluid and seawater: implications regarding surface complexation and color banding in ferrihydrite deposits. *Am. Mineral.* **2001,** *86*, 834-851.
242. Smedley, P. L.; Kinniburgh, D. G., A review of the source, behavior and distribution of arsenic in natural waters. *Applied Geochemistry* **2002,** *17*, 517-568.
243. Pichler, T.; Veizer, J.; Hall, G. E. M., Natural input of arsenic into a coral-reef ecosystem by hydrothermal fluids and its removal by Fe(II) oxyhydroxides. *Environ. Sci. Technol.* **1999,** *33*, 1373-1377.
244. Erbs, J. J.; Gilbert, B.; Penn, R. L., Influence of Size on Reductive Dissolution of Six-Line Ferrihydrite--Supporting Information. *J. Phys. Chem. C* **2008,** *112* (32), 12127-12133.
245. Jentzsch, T.; Penn, R. L., Influence of aluminum doping on ferrihydrite nanoparticle reactivity. *J. Phys. Chem. B* **2006,** *110*, 11746-11750.
246. Jentzsch, T. L. Reactivity of aluminum-doped iron oxide nanoparticles. Ph.D., University of Minnesota, Minneapolis, 2007.

247. Egger, M.; Rasigraf, O.; Sapart, C. J.; Jilbert, T.; Jetten, M. S. M.; Röckmann, T.; van der Veen, C.; Bândă, N.; Kartal, B.; Ettwig, K. F.; Slomp, C. P., Iron-Mediated Anaerobic Oxidation of Methane in Brackish Coastal Sediments. *Environ. Sci. Technol.* **2015,** *49* (1), 277-283.
248. Qi-an, P.; Muhammad, S.; Ronggui, H.; Yongliang, M.; Yupeng, W.; Bashir, U., Effects of soluble organic carbon addition on CH4 and CO2 emissions from paddy soils regulated by iron reduction processes. *Soil Research* **2015,** *53*, 316-324.
249. Wissing, L.; Kölbl, A.; Häusler, W.; Schad, P.; Cao, Z.-H.; Kögel-Knabner, I., Management-induced organic carbon accumulation in paddy soils: The role of organo-mineral associations. *Soil & Tillage Research* **2012,** *126*, 60-71.
250. Sulzberger, B., Light-Induced Redox Cycling of Iron: Roles for CO2 Uptake and Release by Aquatic Ecosystems. *Aquatic Geochemistry* **2015,** *21* (2-4), 65-80.
251. Masue-Slowey, Y.; Loeppert, R. H.; Fendorf, S., Alteration of ferrihydrite reductive dissolution and transformation by adsorbed As and structural Al: Implications for As retention. *Geochim. Cosmochim. Acta* **2011,** *75* (3), 870-886.
252. Paige, C. R.; Snodgrass, W. J.; Nicholson, R. V.; Scharer, J. M., An arsenate effect on ferrihydrite dissolution kinetics under acidic oxic conditions. *Water Research* **1997,** *31* (9), 2370-2382.
253. Gorski, C. A.; Handler, R. M.; Beard, B. L.; Pasakarnis, T.; Johnson, C. M.; Scherer, M. M., Fe atom exchange between aqueous Fe2+ and magnetite. *Environ. Sci. Technol.* **2012,** *46* (22), 12399-407.
254. Handler, R. M.; Beard, B. L.; Johnson, C. M.; Scherer, M. M., Atom Exchange between Aqueous Fe(II) and Goethite: An Fe Isotope Tracer Study. *Environ. Sci. Technol.* **2009,** *43* (4), 1102-1107.
255. Yanina, S. V.; Rosso, K. M., Linked Reactivity at Mineral-Water Interfaces Through Bulk Crystal Conduction. *Science* **2008,** *320* (5873), 218-222.
256. Katz, J. E.; Zhang, X.; Attenkofer, K.; Chapman, K. W.; Frandsen, C.; Zarzycki, P.; Rosso, K. M.; Falcone, R. W.; Waychunas, G. A.; Gilbert, B., Electron small polarons and their mobility in iron (oxyhydr)oxide nanoparticles. *Science* **2012,** *337* (6099), 1200-3.
257. Nelson, J., Continuous-time random-walk model of electron transport in nanocrystalline TiO2 electrodes. *Phys. Rev. B: Condens. Matter Mater. Phys.* **1999,** *59*, 15374-15380.
258. Kerisit, S.; Rosso, K. M., Kinetic Monte Carlo model of charge transport in hematite (α-Fe2O3). *J Chem Phys* **2007,** *127* (12), 124706.
259. Iordanova, N.; Dupuis, M.; Rosso, K. M., Charge transport in metal oxides: A theoretical study of hematite α-Fe2O3. *J Chem Phys* **2005,** *122* (14), 144305.
260. Yuwono, V. M.; Burrows, N. D.; Soltis, J. A.; Anh Do, T.; Lee Penn, R., Aggregation of ferrihydrite nanoparticles in aqueous systems. *Faraday Discuss.* **2012,** *159* (1), 235-245.
261. Gilbert, B.; Katz, J. E.; Huse, N.; Zhang, X.; Frandsen, C.; Falcone, R. W.; Waychunas, G. A., Ultrafast electron and energy transfer in dye-sensitized iron oxide and oxyhydroxide nanoparticles. *Phys Chem Chem Phys* **2013,** *15* (40), 17303-13.
262. Zarzycki, P.; Charmas, R.; Szabelski, P., Study of proton adsorption at heterogeneous oxide/electrolyte interface. Prediction of the surface potential using Monte

Carlo simulations and 1-pK approach. *Journal of Computational Chemistry* **2004,** *25* (5), 704-711.
263. Zarzycki, P.; Rosso, K. M., Origin of Two Time-Scale Regimes in Potentiometric Titration of Metal Oxides. A Replica Kinetic Monte Carlo Study. *Langmuir* **2009,** *25* (12), 6841-6848.
264. Mulvaney, P.; Cooper, R.; Grieser, F.; Meisel, D., Charge trapping in the reductive dissolution of colloidal suspensions of iron(III) oxides. *Langmuir* **1988,** *4* (5), 1206-1211.
265. Tiedje, T.; Rose, A., *Solid State Commun* **1980,** *37*, 49-52.
266. Seki, K.; Wojcik, M.; Tachiya, M. J., Dispersive-diffusion-controlled distance-dependent recombination in amorphous semiconductors. *Chem. Phys.* **2006,** *124*, 044702
267. Eggleton, R. A.; Fitzpatrick, R. W., New data and a revised structural model for ferrihydrite. *Clays Clay Miner.* **1988,** *36*, 111-24.
268. Abbas, Z.; Labbez, C.; Nordholm, S.; Ahlberg, E., Size-Dependent Surface Charging of Nanoparticles. *J. Phys. Chem. C* **2008,** *112*, 5715-5723.
269. Barroso, M.; Pendlebury, S. R.; Cowan, A. J.; Durrant, J. R., Charge carrier trapping, recombination and transfer in hematite (α-Fe2O3) water splitting photoanodes. *Chemical Science* **2013,** *4* (7), 2724.
270. Dimitrijevic, N. M.; Savic, D.; Micic, O. I.; Nozik, A. J., Interfacial electron-transfer equilibria and flatband potentials of .alpha.-ferric oxide and titanium dioxide colloids studied by pulse radiolysis. *The Journal of Physical Chemistry* **1984,** *88* (19), 4278-4283.
271. Burns, P. C.; Sigmon, G. E., *Uranium: Cradle to grave*. Mineralogical Association of Canada: 2013; Vol. 43, p 437.
272. Abrefah, J.; Marschmann, S.; Jenson, E. D., Examination of the surface coatings removed from K-East Basin fuel elements, PNNL-11806. Pacific Northwest National Laboratory: Richland, WA, 1998.
273. Finn, P. A.; Hoh, J. C.; Wolf, S. F.; Slater, S. A.; Bates, J. K., The release of uranium, plutonium, cesium, strontium, technetium and iodine from spent fuel under unsaturated conditions. *Radiochim. Acta* **1996,** *74*, 65.
274. Bruno, J.; Ewing, R. C., Spent nuclear fuel. *Elements* **2006,** *2*, 343.
275. Finch, R. J.; Buck, E. C.; Finn, P. A.; Bates, J. K., In *Scientific Basis for Nuclear Waste Management XXII*, Wronkiewicz, D. J.; Lee, J. H., Eds. Materials Research Society: Warrendale, PA, 1999; Vol. 556, pp 431–438.
276. Girardot, C. L.; Harlow, D. G., Hanford Single-Shell Tank Leak Causes and Locations - 241-SX Farm PNNL RPP-RPT-54910, Rev. 0. Washington River Protection Solutions: Richland, WA, 2014.
277. Finch, R. J.; Ewing, R. C., The Corrosion of Uranite Under Oxidizing Conditions. *J. Nucl. Mater.* **1992,** *190*, 133
278. Burns, P. C.; Ewing, R. C.; Navrotsky, A., Nuclear fuel in a reactor accident. *Science* **2012,** *335* (6073), 1184-8.
279. Burns, P. C., Nanoscale uranium-based cage clusters inspired by uranium mineralogy. *Mineral. Mag.* **2011,** *75* (1), 1-25.
280. Yin, P.; Li, D.; Liu, T., Counterion Interaction and Association in Metal-Oxide Cluster Macroanionic Solutions and the Consequent Self-Assembly. *Isr. J. Chem.* **2011,** *51* (2), 191-204.

281. Ammam, M., Polyoxometalates: formation, structures, principal properties, main deposition methods and application in sensing. *J. Mater. Chem. A* **2013,** *1* (21), 6291.
282. Long, D. L.; Tsunashima, R.; Cronin, L., Polyoxometalates: building blocks for functional nanoscale systems. *Angew Chem Int Ed Engl* **2010,** *49* (10), 1736-58.
283. Nyman, M.; Burns, P. C., A comprehensive comparison of transition-metal and actinyl polyoxometalates. *Chem. Soc. Rev.* **2012,** *41* (22), 7354-7367.
284. Muller, A.; Diemann, E.; Kuhlmann, C.; Eimer, W.; Serain, C.; Tak, T.; Knochel, A.; Pranzas, P. K., Hierarchic patterning: architectures beyond 'giant molecular wheels'. *Chem. Commun.* **2001,** (19), 1928-1929.
285. Liu, T., Hydrophilic Macroionic Solutions: What Happens When Soluble Ions Reach the Size of Nanometer Scale? *Langmuir* **2009,** *26* (12), 9202-9213.
286. Pigga, J. M.; Teprovich, J. A.; Flowers, R. A.; Antonio, M. R.; Liu, T., Selective Monovalent Cation Association and Exchange around Keplerate Polyoxometalate Macroanions in Dilute Aqueous Solutions. *Langmuir* **2010,** *26*, 9449-9456.
287. Liu, G.; Liu, T., Thermodynamic Properties of the Unique Self-Assembly of {Mo72Fe30} Inorganic Macro-Ions in Salt-Free and Salt-Containing Aqueous Solutions. *Langmuir* **2005,** *21*, 2713-2720.
288. Liu, G.; Cai, Y.; Liu, T., Automatic and Subsequent Dissolution and Precipitation Process in Inorganic Macroionic Solutions. *J. Am. Chem. Soc.* **2004,** *126*, 16690-16691.
289. Liu, T.; Diemann, E.; Li, H.; Dress, A. W. M.; Muller, A., Self-assembly in aqueous solution of wheel-shaped Mo154 oxide clusters into vesicles. *Nature* **2003,** *426* (6962), 59-62.
290. Chen, B.; Jiang, H.; Zhu, Y.; Cammers, A.; Selegue, J. P., Monitoring the Growth of Polyoxomolybdate Nanoparticles in Suspension by Flow Field-Flow Fractionation. *J. Am. Chem. Soc.* **2005,** *127* (12), 4166-4167.
291. Zhu, Y.; Cammers-Goodwin, A.; Zhao, B.; Dozier, A.; Dickey, E. C., Kinetic Precipitation of Solution-Phase Polyoxomolybdate Followed by Transmission Electron Microscopy: A Window to Solution-Phase Nanostructure. *Chem. - Eur. J.* **2004,** *10* (10), 2421-2427.
292. Wang, C.-Y.; Boettcher, C.; Bahnemann, D. W.; Dohrmann, J. K., In situ Electron Microscopy Investigation of Fe(III)-doped TiO2 Nanoparticles in an Aqueous Environment. *J. Nanopart. Res.* **2004,** *6*, 119-122.
293. Klokkenburg, M.; Vonk, C.; Claesson, E. M.; Meeldijk, J. D.; Erné, B. H.; Philipse, A. P., Direct Imaging of Zero-Field Dipolar Structures in Colloidal Dispersions of Synthetic Magnetite. *J. Am. Chem. Soc.* **2004,** *126* (51), 16706-16707.
294. Legg, B. A.; Zhu, M.; Comolli, L. R.; Gilbert, B.; Banfield, J. F., Determination of the Three-Dimensional Structure of Ferrihydrite Nanoparticle Aggregates. *Langmuir* **2014,** *30*, 9931-9940.
295. Berret, J.-F.; Schonbeck, N.; Gazeau, F.; El Kharrat, D.; Sandre, O.; Vacher, A.; Airiau, M., Controlled Clustering of Superparamagnetic Nanoparticles Using Block Copolymers: Design of New Contrast Agents for Magnetic Resonance Imaging. *J. Am. Chem. Soc.* **2006,** *128* (5), 1755-1761.
296. Ilavsky, J.; Jemian, P. R.; Allen, A. J.; Zhang, F.; Levine, L. E.; Long, G. G., Ultra-small-angle X-ray scattering at the Advanced Photon Source. *J. Appl. Crystallogr.* **2009,** *42*, 469-479.

297. Ilavsky, J.; Jemian, P. R., Irena: tool suite for modeling and analysis of small-angle scattering. *J. Appl. Crystallogr.* **2009,** *42* (2), 347-353.
298. Mackay, A. L.; Finney, J. L.; Gotoh, K., The closest packing of equal spheres on a spherical surface. *Acta Crystallogr., Sect. A* **1977,** *33* (1), 98-100.
299. Williams, D. B.; Carter, C. B., *Transmission Electron Microscopy: A textbook for materials science*. Plenum Press: New York, 1996.
300. Pigga, J. M.; Kistler, M. L.; Shew, C.-Y.; Antonio, M. R.; Liu, T., Counterion Distribution around Hydrophilic Molecular Macroanions: The Source of the Attractive Force in Self-Assembly. *Angew. Chem., Int. Ed.* **2009,** *48*, 6538-6542, S6538/1-S6538/11.